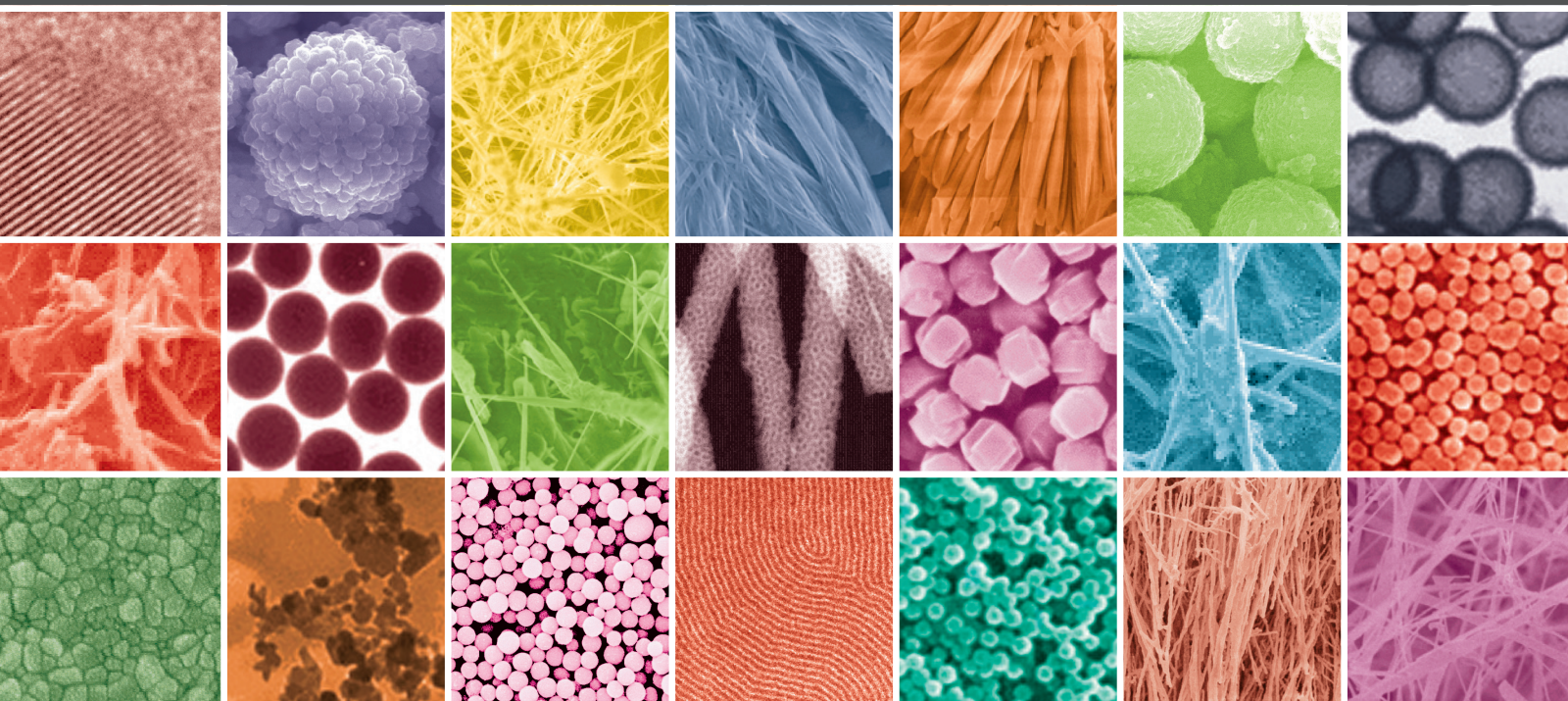


Nanomaterials for Energy-Efficient Applications

Guest Editors: Xiaohu Huang, Guozhong Xing, Yongfeng Li,
and Ekaterina Nannen





Nanomaterials for Energy-Efficient Applications

Journal of Nanomaterials

Nanomaterials for Energy-Efficient Applications

Guest Editors: Xiaohu Huang, Guozhong Xing, Yongfeng Li,
and Ekaterina Nannen



Copyright © 2015 Hindawi Publishing Corporation. All rights reserved.

This is a special issue published in “Journal of Nanomaterials.” All articles are open access articles distributed under the Creative Commons Attribution License, which permits unrestricted use, distribution, and reproduction in any medium, provided the original work is properly cited.

Editorial Board

Domenico Acierno, Italy
Katerina Aifantis, USA
Sheikh Akbar, USA
Nageh K. Allam, USA
Margarida Amaral, Portugal
Jordi Arbiol, Spain
Raul Arenal, Spain
Ilaria Armentano, Italy
Lavinia Balan, France
Thierry Baron, France
Andrew R. Barron, USA
Hongbin Bei, USA
Stefano Bellucci, Italy
Enrico Bergamaschi, Italy
D. Bhattacharyya, New Zealand
Giovanni Bongiovanni, Italy
Theodorian Borca-Tasciuc, USA
Mohamed Bououdina, Bahrain
Torsten Brezesinski, Germany
C. Jeffrey Brinker, USA
Christian Brosseau, France
Yibing Cai, China
Chuanbao Cao, China
Victor M. Castao, Mexico
Albano Cavaleiro, Portugal
Bhanu P. S. Chauhan, USA
Wei Chen, China
Tupei Chen, Singapore
Yuan Chen, Singapore
Shafiul Chowdhury, USA
Kwang-Leong Choy, UK
Jin-Ho Choy, Korea
Yu-Lun Chueh, Taiwan
Elisabetta Comini, Italy
Giuseppe Compagnini, Italy
David Cornu, France
Miguel A. Correa-Duarte, Spain
P. Davide Cozzoli, Italy
Majid Darroudi, Iran
Shadi A. Dayeh, USA
Luca Deseri, USA
Yong Ding, USA
Bin Dong, China
Zehra Durmus, Turkey
Joydeep Dutta, Oman

Ali Eftekhari, USA
Samy El-Shall, USA
Farid El-Tantawy, Egypt
Ovidiu Ersen, France
Claude Estourns, France
Andrea Falqui, Saudi Arabia
Xiaosheng Fang, China
Bo Feng, China
Matteo Ferroni, Italy
Wolfgang Fritzsche, Germany
Alan Fuchs, USA
Peng Gao, China
Miguel A. Garcia, Spain
Siddhartha Ghosh, Singapore
P. K. Giri, India
Russell E. Gorga, USA
Jihua Gou, USA
Alexander Govorov, USA
Jean M. Greneche, France
Changzhi Gu, China
Lin Guo, China
John Z. Guo, USA
Smrati Gupta, Germany
Kimberly Hamad-Schifferli, USA
Michael Harris, USA
Jr-Hau He, Taiwan
Nguyen D. Hoa, Vietnam
Michael Z. Hu, USA
Qing Huang, China
Nay Ming Huang, Malaysia
Shaoming Huang, China
David Hui, USA
Zafar Iqbal, USA
Balachandran Jeyadevan, Japan
Xin Jiang, Germany
Rakesh Joshi, Australia
Myung-Hwa Jung, Korea
Jeong-won Kang, Korea
Hassan Karimi-Maleh, Iran
Antonios Kelarakis, UK
Alireza Khataee, Iran
Ali Khorsand Zak, Iran
Dojin Kim, Korea
Wonbaek Kim, Korea
Jang-Kyo Kim, Hong Kong

Philippe Knauth, France
Ralph Krupke, Germany
Christian Kübel, Germany
Sanjeev Kumar, India
Sushil Kumar, India
Prashant Kumar, UK
Subrata Kundu, India
Michele Laus, Italy
Eric Le Bourhis, France
Burtrand Lee, USA
Jun Li, Singapore
Meiyong Liao, Japan
Silvia Licoccia, Italy
Wei Lin, USA
Jun Liu, USA
Zainovia Lockman, Malaysia
Songwei Lu, USA
Jue Lu, USA
Ed Ma, USA
Malik Maaza, South Africa
Lutz Mädler, Germany
Gaurav Mago, USA
Morteza Mahmoudi, Iran
Mohammad A. Malik, UK
Devanesan Mangalaraj, India
Sanjay R. Mathur, Germany
Paulo Cesar Morais, Brazil
Mahendra A. More, India
Paul Munroe, Australia
Jae-Min Myoung, Korea
Rajesh Naik, USA
Albert Nasibulin, Russia
Toshiaki Natsuki, Japan
Koichi Niihara, Japan
Sherine Obare, USA
Won-Chun Oh, Republic of Korea
Atsuto Okamoto, Japan
Abdelwahab Omri, Canada
Ungyu Paik, Republic of Korea
Edward A. Payzant, USA
Ton Peijs, UK
Oscar Perales-Prez, Puerto Rico
Wenxiu Que, China
Peter Reiss, France
Orlando Rojas, USA



Marco Rossi, Italy
Cengiz S. Ozkan, USA
Vladimir Šepelák, Germany
Huaiyu Shao, Japan
Prashant Sharma, USA
Donglu Shi, USA
Bhanu P. Singh, India
Surinder Singh, USA
Vladimir Sivakov, Germany
Yanlin Song, China
Ashok Sood, USA
Marinella Striccoli, Italy
Jing Sun, China
Xuping Sun, Saudi Arabia
Ashok K. Sundramoorthy, USA

Sabine Szunerits, France
Nyan-Hwa Tai, Taiwan
Bo Tan, Canada
Ion Tiginyanu, Moldova
Valeri P. Tolstoy, Russia
Muhammet S. Toprak, Sweden
Ramon Torrecillas, Spain
Takuya Tsuzuki, Australia
Tamer Uyar, Turkey
Bala Vaidhyanathan, UK
Luca Valentini, Italy
Rajender S. Varma, USA
Antonio Villaverde, Spain
Ajayan Vinu, Australia
Shiren Wang, USA

Yong Wang, USA
Ruibing Wang, Macau
Magnus Willander, Sweden
Ping Xiao, UK
Zhi Li Xiao, USA
Yangchuan Xing, USA
Doron Yadlovker, Israel
Piaoping Yang, China
Yoke K. Yap, USA
Ramin Yousefi, Iran
Kui Yu, Canada
William W. Yu, USA
Renyun Zhang, Sweden

Nanomaterials for Energy-Efficient Applications, Xiaohu Huang, Guozhong Xing, Yongfeng Li, and Ekaterina Nannen
Volume 2015, Article ID 524095, 2 pages

Effect of CdS/Mg-Doped CdSe Cosensitized Photoanode on Quantum Dot Solar Cells, Yingxiang Guan, Xiaoping Zou, and Sheng He
Volume 2015, Article ID 673135, 6 pages

Enhanced Efficiency of Dye-Sensitized Solar Cells by Trace Amount Ca-Doping in TiO₂ Photoelectrodes, Mengmei Pan, Hanjun Liu, Zhongyu Yao, and Xiaoli Zhong
Volume 2015, Article ID 974161, 5 pages

Multiwalled Carbon Nanotube-TiO₂ Nanocomposite for Visible-Light-Induced Photocatalytic Hydrogen Evolution, Ke Dai, Xiaohu Zhang, Ke Fan, Peng Zeng, and Tianyou Peng
Volume 2014, Article ID 694073, 8 pages

Functional Carbon Nanotube/Mesoporous Carbon/MnO₂ Hybrid Network for High-Performance Supercapacitors, Tao Tao, Ling Zhang, Hao Jiang, and Chunzhong Li
Volume 2014, Article ID 568561, 6 pages

Structural and Electrical Properties of the YSZ/STO/YSZ Heterostructure, Yue Fan, Wende Liu, Zhenfeng Kang, Tiezhu Ding, Qingrui Bo, Lingling Xiao, Xiaobing Bai, Pingping Zheng, and Qiang Li
Volume 2014, Article ID 783132, 5 pages

Tungsten Oxide and Polyaniline Composite Fabricated by Surfactant-Templated Electrodeposition and Its Use in Supercapacitors, Benxue Zou, Shengchen Gong, Yan Wang, and Xiaoxia Liu
Volume 2014, Article ID 813120, 9 pages

Editorial

Nanomaterials for Energy-Efficient Applications

Xiaohu Huang,¹ Guozhong Xing,² Yongfeng Li,³ and Ekaterina Nannen⁴

¹*Institute of Materials Research and Engineering, Agency for Science, Technology and Research (A*STAR), 3 Research Link, Singapore 117602*

²*School of Materials Science and Engineering, The University of New South Wales, Sydney, NSW 2052, Australia*

³*Key Laboratory of Physics and Technology for Advanced Batteries (Ministry of Education), College of Physics, Jilin University, Changchun 130012, China*

⁴*Department of Electrical Engineering and Information Technology, University of Duisburg-Essen, 47057 Duisburg, Germany*

Correspondence should be addressed to Xiaohu Huang; xhhuang.nano@gmail.com

Received 4 December 2014; Accepted 4 December 2014

Copyright © 2015 Xiaohu Huang et al. This is an open access article distributed under the Creative Commons Attribution License, which permits unrestricted use, distribution, and reproduction in any medium, provided the original work is properly cited.

The ways we used to generate and utilize energy have been threatening our living environment. For example, the crude oil spills in Gulf of Mexico in 2010 left devastating effects to the Gulf ecosystem, Fukushima nuclear plant leaks in Japan in 2012 threatened the lives of thousands of people, and the Haze in the cities of China at present affects the health of millions of people. All of them remind us of the global energy and environment crisis that we have to face in the near future. Alternative solutions in energy generation and utilization have to be explored towards a sustainable earth.

Many breakthroughs in the area of nanomaterials and nanosciences have been reported recently [1–12], which open up tremendous opportunities to tackle the challenges in energy and environment. With shrinking the size of the materials into nanoscale, fewer materials are required, which translates to higher utility efficiency of the resources. Moreover, with the dimensions of the materials decreasing to a scale comparable to the characteristic length of the physical properties, behaviors of photon emission [1], electron transport [2], surface train [3], and phonon scattering [4] change drastically compared to their bulk counterpart. The resulting properties have very important implications to their applications in high brightness light-emitting diodes [5–7], low power nanoelectronics [2], high efficiency solar cells [8], thermoelectric power generator [4], and so forth. In addition,

the large surface-to-volume ratio in nanomaterials facilitates more efficient chemical reactions, which is highly desirable in many applications such as high performance batteries and catalysts [9, 10]. Therefore, the research activities of nanomaterials on energy-related applications have surged over the past decade, which is manifested by the exponential growth of the corresponding research publications and citations as shown in Figure 1. It is very clear that the research on energy-related nanoscience and nanotechnology has been becoming extremely active since 2010.

However, the success of nanomaterials in energy-efficient applications relies on our ability to synthesize nanomaterials at will and to understand and tailor the properties of the nanomaterials [11, 12] and to integrate the nanomaterials into devices [1, 2, 7, 9]. This special issue solicits some of these topics to foster the applications of nanomaterials in the emerging energy research. Moreover, the research trend of nanomaterials towards high performance energy-efficient applications could be summarized from the articles published in this special issue, for example, chemical doping, interface engineering, and hybridizing.

We hope that the readers will find in this special issue not only the interesting results but also important questions to be resolved and finally incorporate the findings into their own research. We hope this special issue can inspire more

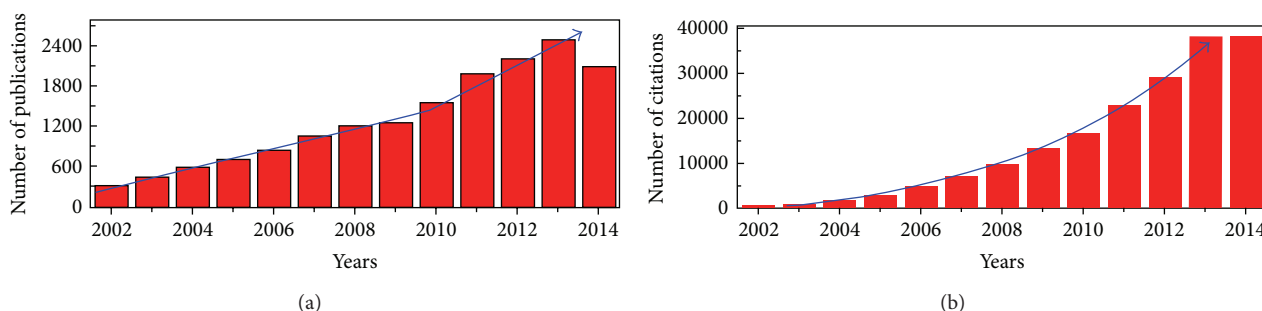


FIGURE 1: The numbers of (a) publications and (b) citations retrieved from Web of Science by listing both “nano” and “energy” as the key words in the search engine. The search was conducted on November 21, 2014; thus any update after that was not reflected in this figure.

research efforts on nanomaterials towards energy-efficient and environmentally friendly applications.

Xiaohu Huang
Guozhong Xing
Yongfeng Li
Ekaterina Nannen

References

- [1] Y. Li, W. Yin, R. Deng et al., “Realizing a SnO_2 -based ultraviolet light-emitting diode via breaking the dipole-forbidden rule,” *NPG Asia Materials*, vol. 4, no. 11, article e30, 2012.
- [2] W. Lu and C. M. Lieber, “Nanoelectronics from the bottom up,” *Nature Materials*, vol. 6, no. 11, pp. 841–850, 2007.
- [3] X. Huang, G. Li, L. B. Kong, Y. Z. Huang, and T. Wu, “Anisotropic surface strain in single crystalline cobalt nanowires and its impact on the diameter-dependent Young’s modulus,” *Nanoscale*, vol. 5, no. 23, pp. 11643–11648, 2013.
- [4] D. Li, Y. Wu, P. Kim, L. Shi, P. Yang, and A. Majumdar, “Thermal conductivity of individual silicon nanowires,” *Applied Physics Letters*, vol. 83, no. 14, pp. 2934–2936, 2003.
- [5] X. H. Huang, Z. Y. Zhan, K. P. Pramoda, C. Zhang, L. X. Zheng, and S. J. Chua, “Correlating the enhancement of UV luminescence from solution-grown ZnO nanorods with hydrogen doping,” *CrystEngComm*, vol. 14, no. 16, pp. 5163–5165, 2012.
- [6] X. H. Huang, C. Zhang, C. B. Tay, T. Venkatesan, and S. J. Chua, “Green luminescence from Cu-doped ZnO nanorods: role of Zn vacancies and negative thermal quenching,” *Applied Physics Letters*, vol. 102, no. 11, Article ID 111106, 2013.
- [7] E. Neshataeva, T. Kümmell, G. Bacher, and A. Ebbers, “All-inorganic light emitting device based on ZnO nanoparticles,” *Applied Physics Letters*, vol. 94, no. 9, Article ID 091115, 2009.
- [8] C. F. Guo, T. Y. Sun, F. Cao, Q. Liu, and Z. F. Ren, “Metallic nanostructures for light trapping in energy-harvesting devices,” *Light: Science and Applications*, vol. 3, article e161, 2014.
- [9] G. Z. Xing, Y. Wang, J. I. Wong, Y. M. Shi, S. Li, and H. Y. Yang, “Hybrid CuO/SnO_2 nanocomposites: towards cost-effective and high performance binder free lithium ion batteries anode materials,” *Applied Physics Letters*, vol. 105, Article ID 143905, 2014.
- [10] H. R. Byon, J. Suntivich, and Y. Shao-Horn, “Graphene-based non-noble-metal catalysts for oxygen reduction reaction in acid,” *Chemistry of Materials*, vol. 23, no. 15, pp. 3421–3428, 2011.
- [11] X. Huang, L. Li, X. Luo, X. Zhu, and G. Li, “Orientation-controlled synthesis and ferromagnetism of single crystalline Co nanowire arrays,” *The Journal of Physical Chemistry C*, vol. 112, no. 5, pp. 1468–1472, 2008.
- [12] G. Z. Xing, X. S. Fang, X. Huang et al., “Ultrathin single-crystal ZnO nanobelts: Ag-catalyzed growth, optical absorption and field emission properties,” *Nanotechnology*, vol. 21, Article ID 255701, 2010.

Research Article

Effect of CdS/Mg-Doped CdSe Cosensitized Photoanode on Quantum Dot Solar Cells

Yingxiang Guan, Xiaoping Zou, and Sheng He

Research Center for Sensor Technology, Beijing Key Laboratory for Sensor, Ministry of Education Key Laboratory for Modern Measurement and Control Technology, School of Applied Sciences, and School of Information & Communication Engineering, Beijing Information Science and Technology University, Jianxiangqiao Campus, Beijing 100101, China

Correspondence should be addressed to Xiaoping Zou; xpzou2005@gmail.com

Received 31 May 2014; Accepted 13 August 2014

Academic Editor: Yongfeng Li

Copyright © 2015 Yingxiang Guan et al. This is an open access article distributed under the Creative Commons Attribution License, which permits unrestricted use, distribution, and reproduction in any medium, provided the original work is properly cited.

Quantum dots have emerged as a material platform for low-cost high-performance sensitized solar cells. And doping is an effective method to improve the performance of quantum dot sensitized solar cells (QDSSCs). Since Kwak et al. from South Korea proved the incorporation of Mg in the CdSe quantum dots (QDs) in 2007, the Mg-doped CdSe QDs have been thoroughly studied. Here we report a new attempt on CdS/Mg-doped CdSe quantum dot cosensitized solar cells (QDCSSC). We analyzed the performance of CdS/Mg-doped CdSe quantum dot cosensitized solar cells via discussing the different doping concentration of Mg and the different SILAR cycles of CdS. And we studied the mechanism of CdS/Mg-doped CdSe QDs in detail for the reason why the energy conversion efficiency had been promoted. It is a significant instruction on the development of Mg-doped CdSe quantum dot sensitized solar cells (QDSSCs).

1. Introduction

Recently, doping of semiconductor quantum dot has been largely developed. It provides a broad way to achieve low-cost high-performance optoelectronic devices. Lee and his colleagues reported on a PbS:Hg QDSSC with high power conversion of 5.6% for the extremely high J_{sc} (30 mA/cm²) last year [1]. It has shown the great potential of QDSSCs. CdSe is a kind of sensitizer system and has gotten lots of research. Mg-doped CdSe is one kind of doping scheme. In 2007, Kwak et al. proved that Mg was doped into CdSe with X-ray energy dispersive spectroscopy (EDS) and inductively coupled plasma mass spectrometry (ICPMS) [2]. And they adjusted the band-gap of CdSe nanocrystalline by doping CdSe with Mg which was blue shifted and the intensity of PL spectra of doped CdSe nanocrystalline was similar with that of undoped CdSe nanocrystalline, or even higher. Then they enhanced the ripening kinetics of Mg-doped CdSe nanocrystals because of the low activation energy for the volume diffusion [3]. In 2008, Wonjoo et al. prepared CdSe/Mg-doped

CdSe QDSSCs with chemical bath deposition (CBD) method [4]. It had a more broad range of spectral response in visible region. Thus, the short-circuit current was enhanced by 47%, but the fill factor (FF) and the open circuit voltage did not change significantly compared with undoped CdSe QDSSCs. In 2010, Wang et al. from Qufu Normal University announced the first-principles on the electron structure and optical properties of Mg-doped CdSe system [5]. They calculated the electron structure and optical properties of wurtzite structure $Cd_{1-x}Mg_xSe$ ($x = 0, 0.125, 0.250, 0.375$) by using first-principles ultrasoft pseudopotential plane wave method based on the density functional theory (DFT). The result showed that Se4p electrons fundamentally determined the top of valence band which was essentially the same, while both Se4s electrons and Cd5s electrons determined the bottom of conduction band which was moved to a higher energy region with the increasing Mg concentration, and the band-gap was also broadened. As a result, the peaks in the imaginary part of the dielectric function and the peak in the real part of the refractive index were blue shifted with the

increasing Mg concentration. The CdS/CdSe system is one of the most studied systems. Lee et al. achieved an energy conversion efficiency of 4.22% by using a $\text{TiO}_2/\text{CdS}/\text{CdSe}/\text{ZnS}$ electrode structure in 2009 [6]. Because of the Fermi level alignment, a stepwise structure of band-edge levels was yielded in the cascade structure of $\text{TiO}_2/\text{CdS}/\text{CdSe}$ electrode. And it profited the electron injection and hole recovery.

As we were enlightened by the previous research on doping [7–9] of our research group and the research on Mg-doped CdSe and CdS/CdSe photoanode structure of others, we report a quantum dot cosensitized solar cell prepared by using successive ionic layer absorption and reaction (SILAR) method based on cosensitized CdS/Mg-doped CdSe QDs. (Mg-CdSe stands for Mg-doped CdSe.)

2. Methods

2.1. Device Fabrication. Firstly, with regard to TiO_2 films fabrication, TiO_2 films were printed on the cleaned FTO glass which was treated by a 0.4 M TiCl_4 solution and then annealed at 450°C for 30 min with screen printing method and then annealed at 450°C for 30 min. The thickness of TiO_2 films was about $8.5\ \mu\text{m}$ and the working area was $0.5 \times 0.5\ \text{cm}^2$. Secondly, in photoanode fabrication, the TiO_2 films were dipped into a $\text{Cd}(\text{NO}_3)_2$ ethanol solution (0.1 M) for 5 min and then rinsed with ethanol. After being dried with nitrogen they were dipped into a Na_2S methanol solution (0.1 M) for 5 min and then rinsed with methanol. The two steps were termed as one SILAR cycle. It was similar to the deposition of Mg-CdSe QDs; the cation solution was prepared by adding the $\text{MgCl}_2 \cdot 6\text{H}_2\text{O}$ into preceding Cd^{2+} solution with a settled molar concentration ratio. The anion solution (Na_2SeSO_3) was prepared by refluxing Se (0.06 M) into a Na_2SO_3 aqueous solution (0.12 M) at 70°C for 7 h. But there were longer time (ca. 30 min) and higher temperature (50°C) for dipping them into anion solution. Thirdly, in counter electrode fabrication, Pt counter electrode was prepared by thermal decomposition of chloroplatinic acid; the method is as follows: 0.053 g chloroplatinic acid was dissolved in 10 mL isopropanol to fabricate platinum paste. Then, the Pt counter electrode could be obtained by annealing the FTO glass which was coated with the platinum paste in Muffle furnace at 450°C for 30 min. Fourthly in electrolyte preparation, polysulfide electrolyte was prepared by dissolving 1 M Na_2S and 1 M S in deionized water. Finally, with regard to cells packaging, the prepared photoanode was put on laboratory bench (the coated side facing up). Next a hollow rectangle spacer with the thickness of $60\ \mu\text{m}$ was placed around the photoanode. Then the prepared Pt counter electrode (the conductive side facing down) was put on the photoanode. Then the electrolyte was injected into the cell from the gap between photoanode and counter electrode followed by gripping the cell with clips. (Finished cell should be placed under dark for 40 min before testing.)

2.2. Material Characterization. Scanning electron microscopy (SEM) was used to observe the surface of the films. SEM was performed with a S-4300 of Technical Institute of Physics

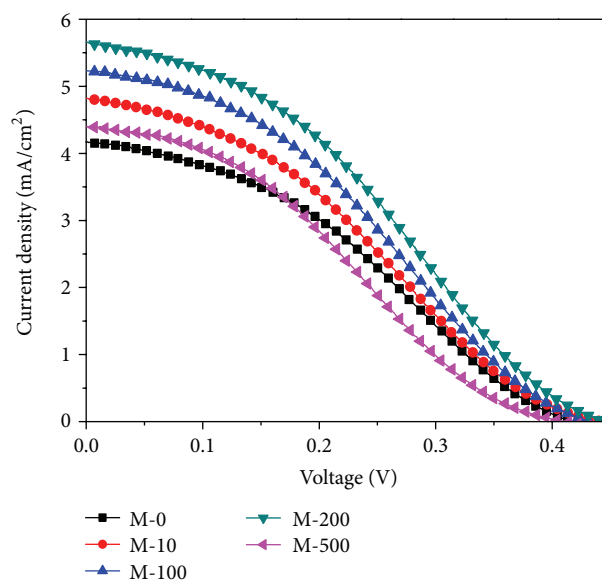


FIGURE 1: The J-V curves of the cells made by sample solution of M-0, M-10, M-100, M-200, and M-500.

and Chemistry, CAS. Energy dispersive X-ray spectroscopy (EDS) was employed with S-4300 equipped with a high-performance energy dispersive X-ray spectroscopy (EDS). Transmission electron microscopy (TEM) was measured with Tecnai G2 F20 S-TWIN at 200 KV. X-ray diffraction (XRD) was performed with Bruker D8 focus. Absorption spectra were measured with a Varian Cary 5000 UV-Vis spectrophotometer. Inductively coupled plasma optical emission spectroscopy (ICP-OES) analysis was performed with a Thermo Fisher IRIS Intrepid II XSP.

2.3. Device Characterization. J-V curves were obtained by using J-V test system which consisted of solar simulator ($100\ \text{mW}/\text{cm}^2$ AM 1.5), irradiance meter, electrochemical workstation (Linear Scan Voltammetry mode), test software, and so on (Figure 2). IPCE measurements were obtained with a IPCE measurement tool ($0.3\text{--}0.8\ \text{mW}/\text{cm}^2$, $350\text{--}800\ \text{nm}$) developed by Institute of Physics, CAS, through DC method. EIS was measured with Princeton Applied Research, V3-400 electrochemical workstation equipped with electrochemical impedance test system. The bias was $-0.5\ \text{V}$, the scanning frequency was from 0.1 Hz to 500 KHz, and the amplitude modulation was 20 mV.

3. Results and Discussions

3.1. Effect of Different Doping Concentration of Mg on the Performance of CdS/Mg-CdSe Quantum Dots Cosensitized Solar Cells. Because of the different doping concentration of Mg, some doped cells performed better than undoped cells, while some did not (Figure 1). The short-circuit current, fill factor, and efficiency of the cells increased first and then reduced (Table 1) with the decrease of doping concentration (from 1:10 to 1:500). Mg existed in CdSe QDS as dopant,

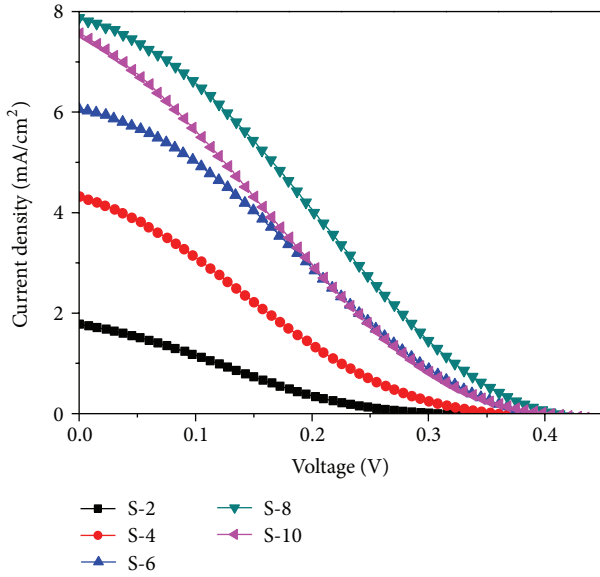


FIGURE 2: The J-V curves of samples of S-2, S-4, S-6, S-8, and S-10.

TABLE 1: The performance parameters of cells made by sample solution of M-0, M-10, M-100, M-200, and M-500.

Samples	J_{sc} (mA/cm ²)	V_{OC} (V)	FF	η (%)
M-0	4.17	0.42	0.35	0.61
M-10	4.82	0.44	0.32	0.68
M-100	5.24	0.43	0.34	0.77
M-200	5.66	0.44	0.34	0.85
M-500	4.40	0.41	0.32	0.57

M-0 stands for that the doping concentration of Mg is 0; similarly, M-10, M-100, M-200, and M-500, respectively, stand for the doping concentration of Mg (Mg: Cd) of 1:10, 1:100, 1:200, and 1:500. Each sample was deposited with 4 SILAR cycles of CdS followed by 4 SILAR cycles of Mg-CdSe.

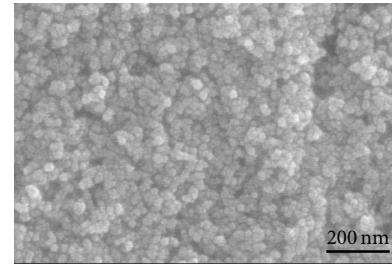
which not only enhanced the short-circuit current density, but also decreased the short-circuit current density as it became the recombination center of electrons and holes. When the concentration of Mg was 1:200, we got the optimal result between the two factors. And because of the recombination centers introduced by dopant Mg, the open-circuit voltage did not change significantly.

3.2. Effect of Different SILAR Cycles of CdS on the Performance of CdS/Mg-CdSe Quantum Dot Cosensitized Solar Cells. We studied the effect of different SILAR cycles on the performance of CdS/Mg-CdSe quantum dot cosensitized solar cells after we got the best doping ratio (Mg: Cd = 1:200). The short-circuit current and open-circuit voltage (Table 2) keep increasing until the SILAR cycles of CdS are 8 and get to the maximum value of 7.87 mA/cm² and 0.41 V, respectively. However, the maximum efficiency of 0.84% was not further improved than previous experimental data. There might have been some problems in the preparation of TiO₂ films or Pt counter electrode. But the optimization of SILAR cycles of CdS has been shown in this experiment.

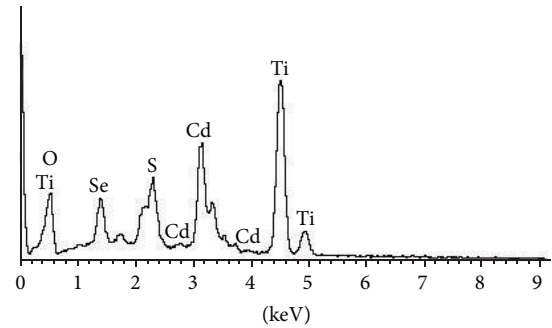
TABLE 2: The performance parameters of samples of S-2, S-4, S-6, S-8, and S-10.

Samples	J_{sc} (mA/cm ²)	V_{OC} (V)	FF	η (%)
S-2	1.79	0.31	0.22	0.12
S-4	4.31	0.36	0.22	0.34
S-6	6.06	0.39	0.26	0.61
S-8	7.87	0.41	0.26	0.84
S-10	7.55	0.40	0.22	0.65

S-2 means that the deposition cycles of CdS were 2. Similarly, S-4, S-6, S-8, and S-10 mean the deposition cycles of CdS were 4, 6, 8, and 10, respectively. All the deposition cycles of Mg-CdSe were 4.



(a)



(b)

FIGURE 3: (a) The SEM image and (b) the EDS spectra of photoanode.

3.3. Analysis of Mg-CdSe Effecting the Performance of CdS/CdSe Quantum Dot Cosensitized Solar Cells. We found that Mg-doped CdSe had a great enhancement on the performance of CdS/CdSe quantum dot cosensitized solar cells (Figure 1). Here we analyze the mechanism of Mg-CdSe effecting the performance of CdS/CdSe quantum dot cosensitized solar cells specifically.

3.3.1. The Material Characterization of CdS/Mg-CdSe Photoanode. As we can see from the scanning electron microscopy (SEM) image of photoanode (Figure 3(a)), the size of TiO₂ is about 20 nm. However, it is hard to find the quantum dots in the SEM image. So we used transmission electron microscopy (TEM) to characterize the quantum dots.

Furthermore, we could not find element Mg in the energy dispersive spectroscopy (EDS) spectra (Figure 3(b)) of photoanode because the weight of MgCl₂·6H₂O was too little for just 0.0051g to detect characteristic X-rays of

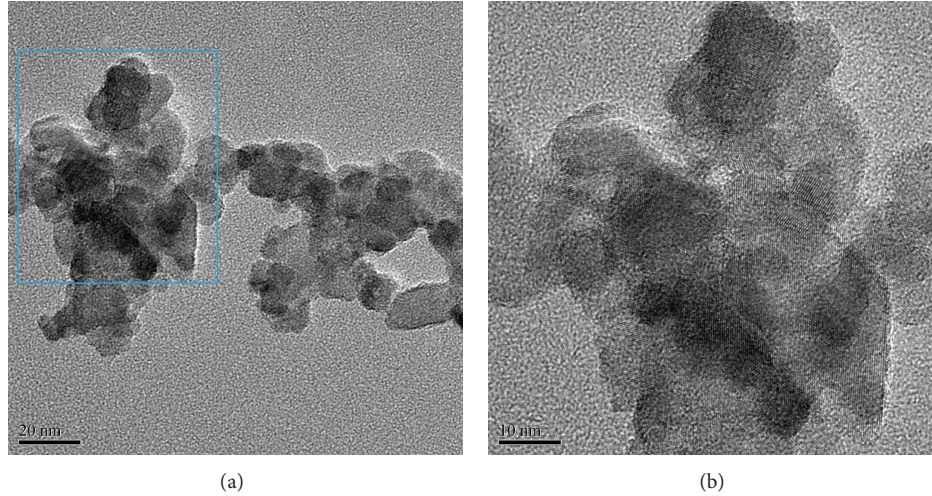


FIGURE 4: TEM images of (a) low magnification and (b) high magnification.

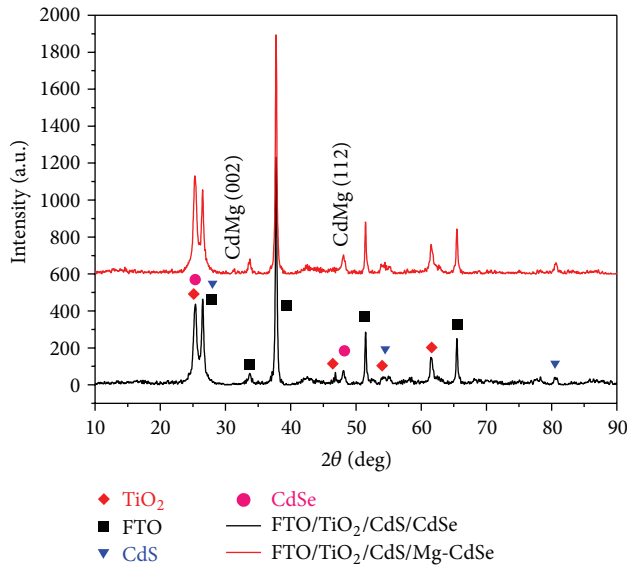


FIGURE 5: XRD pattern of CdS/Mg-doped CdSe photoanode.

element Mg. So as to analyze element Mg qualitatively and quantitatively, we used inductively coupled plasma optical emission spectroscopy.

The size of nanoparticles is about 5–20 nm (Figure 4(a)). Furthermore, the smaller particles of Mg-doped QDs that were found, which are the size of 5 nm, are on the surface of bigger particles of TiO_2 (Figure 4(b)).

XRD results (Figure 5) show that the CdS/Mg-CdSe photoanode has a diffraction peak from impurity atoms of Mg except for diffraction peaks of FTO, TiO_2 , CdS, and CdSe. Two peaks corresponding to lattice plane (002) and (112) of CdMg have been identified at 33.8° and 48.1° , respectively. Particularly, the peak of CdSe at 48.1° has been a little left shifted by 0.01° (from 48.10739° to 48.09740°) through lattice distortion caused by doping with Mg and it is very likely that the peak of TiO_2 at 46.8° has disappeared after being covered

TABLE 3: Quantitative analysis of ICP-OES.

Sample	Cd (μg)	Mg (μg)	Molar ratio (Mg: Cd)
Mg-CdSe	25.51	0.0299	0.54%

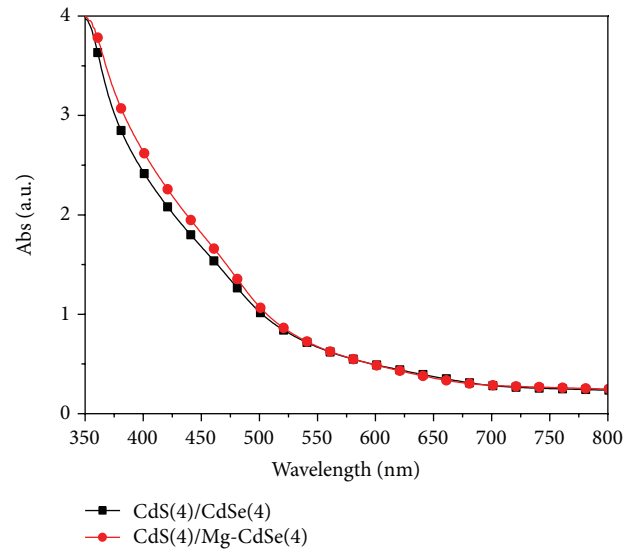


FIGURE 6: UV-Vis absorption spectroscopy of CdS(4)/Mg-CdSe(4) and CdS(4)/CdSe(4).

with quantum dots. So the element Mg dose has doped inside photoanode.

In order to further determine if the element Mg has doped into CdSe QDs, we analyzed quantitatively with ICP-OES (Table 3).

The experimental doping concentration of Mg was 0.5% (Mg: Cd = 1: 200). However, the molar ratio of Mg: Cd was 0.54% actually. That was higher than the experimental data. It might be because the Mg ions reacted with Se ions more easily.

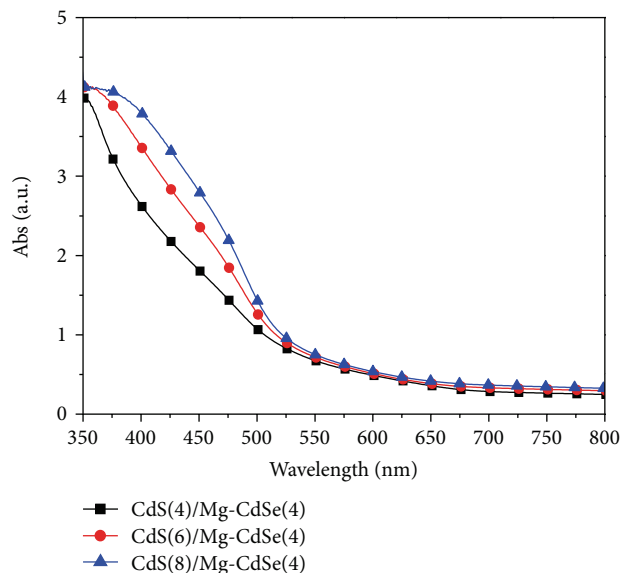


FIGURE 7: UV-Vis absorption spectroscopy of CdS/Mg-CdSe photoanode of different SILAR cycles.

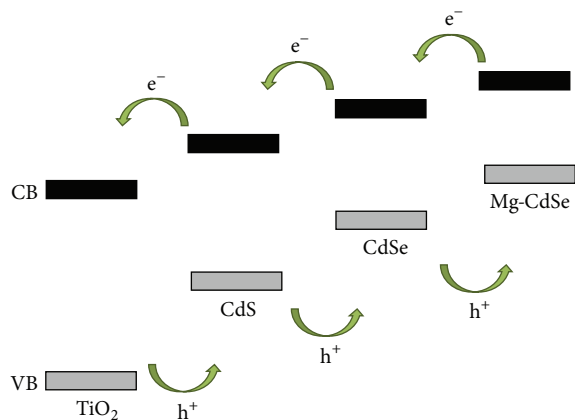


FIGURE 8: Energy level alignment by doping CdSe with Mg.

The comparison between absorption spectroscopy of CdS(4)/Mg-CdSe(4) and that of CdS(4)/CdSe(4) in UV-Vis (Figure 6) shows that the absorption of Mg-doped photoanode has performed a little better than undoped photoanode in the wavelength ranging from 350 nm to 525 nm according to the enhancement of current concentration.

As the deposition cycles of CdS were not optimal, we measured the absorption spectroscopy of CdS/Mg-CdSe photoanode with different SILAR cycles (Figure 7). The absorption of photoanode has been improved with the increasing of SILAR cycles from 4 to 8 in the same wavelength range when the deposition cycles of Mg-CdSe are 4, especially in the wavelength of 350–500 nm.

According to the UV-Vis absorption spectroscopy, the band-gap of CdSe has been narrowed by doping with Mg. Then we made a possible diagram (Figure 8) of the adjustment of Mg-CdSe energy level [6, 9]. The conduction band

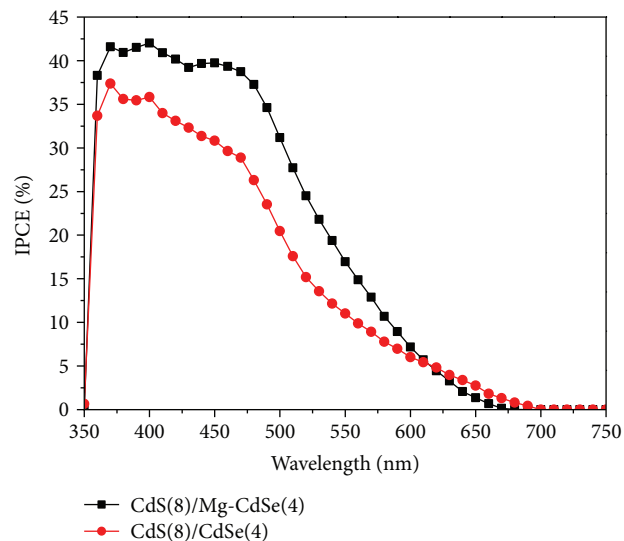


FIGURE 9: IPCE curves of cells made by the photoanode of CdS(8)/Mg-CdSe(4) and CdS(8)/CdSe(4), respectively.

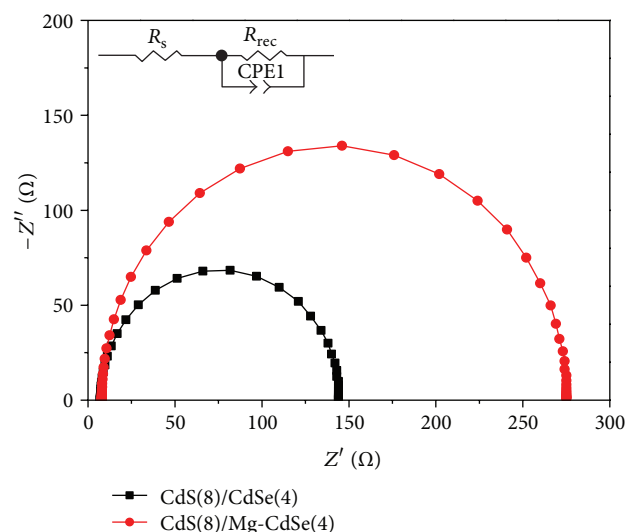


FIGURE 10: EIS of cells with the photoanode of CdS(8)/Mg-CdSe(4) and CdS(8)/CdSe(4). R_s is the series resistance of TCO electrodes, CPE1 is chemical capacitor of photoanode, and $(R_{rec} = r_{rec}L)$ is electron recombination resistance.

and the valence band of CdSe both have become higher after doping with Mg. The stepwise structure yielded by level adjustment has enhanced the electron injection and the hole-recovery and reduced the recombination between electrons and holes, that is, agreement with the improved photocurrent (Table 1). As a result, the conversion efficiency has been enhanced by doping CdSe with Mg.

3.3.2. The Performance of Cells. The maximum value of IPCE has been improved after doping CdSe with Mg (Figure 9). In particular, the max value of IPCE has been improved from 37% to 42% in the wavelength of 350–475 nm. This has been

TABLE 4: Parameters of EIS before and after doping.

Sample number	R_s (Ω)	R_{rec} (Ω)	CPEI (μF)
CdS(8)/CdSe(4)	7.17	137.2	10.65
CdS(8)/Mg-CdSe(4)	7.92	267.4	14.54

consistent with the improvement of preceding absorption spectrum and current density.

The electrochemical impedance spectroscopy (EIS) and the impedance fitting circuit diagram of photoanode and electrolyte are shown in Figure 10. The larger the R_{rec} , the smaller the electron concentration of photoanode and the recombination rate, and the greater the radius of the curves. So the recombination resistance has been increased by doping with Mg (Table 4).

Furthermore, the relationship of lifetime of electrons (τ) between chemical capacitor (CPEI) and electron recombination resistance (R_{rec}) is summarized as

$$\tau = CPEI \cdot R_{rec}. \quad (1)$$

The lifetime of electrons of CdS/Mg-CdSe system has been extended by doping CdSe with Mg compared with that of CdS/CdSe system.

As the performance of cells is decided by several kinds of factors, although this new attempt did not produce a high energy conversion efficiency (0.84%), we believe that we will get a high performance cell after overall optimization of cells.

4. Conclusions

Because of the doping with Mg, the stepwise structure which has improved the electron injection and the hole-recovery has been yielded. And the absorbance has been enhanced. The lifetime of electrons has also been extended. Thus the performance of cells has been improved by doping CdSe with Mg effectively.

Conflict of Interests

The authors declare that there is no conflict of interests regarding the publication of this paper.

Acknowledgments

This work was partially supported by Key Project of Beijing Natural Science Foundation (3131001), Key Project of Natural Science Foundation of China (91233201 and 61376057), Key Project of Beijing Education Committee Science & Technology Plan (KZ201211232040), State 863 Plan of MOST of China (2011AA050527), Beijing National Laboratory for Molecular Sciences (BNLMS2012-21), State Key Laboratory of Solid State Microstructures of Nanjing University (M27019), State Key Laboratory for New Ceramic and Fine Processing of Tsinghua University (KF1210), Key Laboratory for Renewable Energy and Gas Hydrate of Chinese Academy of Sciences (y207ka1001), Beijing Key Laboratory for Sensors of BISTU (KF20141077207 and KF20141077208), and Beijing

Key Laboratory for photoelectrical measurement of BISTU (GDKF2013005).

References

- [1] J.-W. Lee, D.-Y. Son, T. K. Ahn et al., "Quantum-dot-sensitized solar cell with unprecedentedly high photocurrent," *Scientific Reports*, vol. 3, article 1050, 2013.
- [2] W.-C. Kwak, K. T. Geun, W.-S. Chae, and Y.-M. Sung, "Tuning the energy bandgap of CdSe nanocrystals via Mg doping," *Nanotechnology*, vol. 18, no. 20, 2007.
- [3] Y.-M. Sung, W.-C. Kwak, W. Kim, and T. G. Kim, "Enhanced ripening behavior of Mg-doped CdSe quantum dots," *Journal of Materials Research*, vol. 23, no. 7, pp. 1916–1921, 2008.
- [4] L. Wonjoo, K. Woo-Chul, M. S. Ki et al., "Spectral broadening in quantum dots-sensitized photoelectrochemical solar cells based on CdSe and Mg-doped CdSe nanocrystals," *Electrochemistry Communications*, vol. 10, no. 11, pp. 1699–1702, 2008.
- [5] Y.-C. Wang, M. Wang, X.-Y. Su, Z.-Y. Li, and W. Zhao, "First-principles on the electron structure and optical properties of the Mg-doped CdSe system," *Chinese Journal of Luminescence*, vol. 31, no. 6, pp. 842–847, 2010.
- [6] Y.-L. Lee and Y.-S. Lo, "Highly efficient quantum-dot-sensitized solar cell based on co-sensitization of CdS/CdSe," *Advanced Functional Materials*, vol. 19, no. 4, pp. 604–609, 2009.
- [7] Z. Huang, X. Zou, and H. Zhou, "A strategy to achieve superior photocurrent by Cu-doped quantum dot sensitized solar cells," *Materials Letters*, vol. 95, pp. 139–141, 2013.
- [8] L. Li, X. Zou, H. Zhou, and G. Teng, "Cu-doped-CdS/In-doped-CdS cosensitized quantum dot solar cells," *Journal of Nanomaterials*, vol. 2014, Article ID 314386, 8 pages, 2014.
- [9] X. Zou, S. He, G. Teng, and C. Zhao, "Performance study of CdS/Co-doped-CdSe quantum dot sensitized solar cells," *Journal of Nanomaterials*, vol. 2014, Article ID 818160, 6 pages, 2014.

Research Article

Enhanced Efficiency of Dye-Sensitized Solar Cells by Trace Amount Ca-Doping in TiO₂ Photoelectrodes

Mengmei Pan, Hanjun Liu, Zhongyu Yao, and Xiaoli Zhong

School of Physics and Electronic Engineering, Hainan Normal University, Haikou, Hainan 571158, China

Correspondence should be addressed to Hanjun Liu; liuhanjun76@163.com

Received 9 August 2014; Accepted 8 September 2014

Academic Editor: Xiaohu Huang

Copyright © 2015 Mengmei Pan et al. This is an open access article distributed under the Creative Commons Attribution License, which permits unrestricted use, distribution, and reproduction in any medium, provided the original work is properly cited.

Trace amount Ca-doped TiO₂ films were synthesized by the hydrothermal method and applied as photoanodes of dye-sensitized solar cells (DSSCs). To prepare Ca-doped TiO₂ film electrodes, several milliliters of Ca(NO₃)₂ solution was added in TiO₂ solution during the hydrolysis process. The improvements of DSSCs were confirmed by photocurrent density-voltage (*J*-*V*) characteristics, electrochemical impedance spectroscopy (EIS) measurements. Owing to the doping effect of Ca, the Ca-doped TiO₂ thin film shows power conversion efficiency of 7.45% for 50 ppm Ca-doped TiO₂ electrode, which is higher than that of the undoped TiO₂ film (6.78%) and the short-circuit photocurrent density (*J*_{sc}) increases from 13.68 to 15.42 mA·cm⁻². The energy conversion efficiency and short-circuit current density (*J*_{sc}) of DSSCs were increased due to the faster electron transport in the Ca-doped TiO₂ film. When Ca was incorporated into TiO₂ films, the electrons transport faster and the charge collection efficiency η_{cc} is higher than that in the undoped TiO₂ films.

1. Introduction

Dye-sensitized solar cells (DSSCs) based on mesoporous nanocrystalline TiO₂ film have achieved photoelectric conversion efficiency (η) up to 13%. In order to develop high performance of DSSCs and commercialize successfully, many nanocrystalline semiconductors such as TiO₂ [1], ZnO [2], and SnO₂ [3] have been used as photoanode materials. Among them, TiO₂ has been proven to be the best semiconductor electrode material due to its high chemical stability [4], excellent charge transport capability, and ideal position of the conduction band edge. It is known to be one of the main components of DSSCs and plays a key role in determining the performance of DSSCs.

In recent years, Doping has been considered as a promising way to improve the properties of TiO₂ photoanode. TiO₂ films doped with metal and nonmetal have been extensively researched, such as Mg-doping [5], La-doping [6], Nb-doping [7], Ta-doping [8], and N-doping [9], which may increase the photoelectric conversion efficiency. In all the applications mentioned above, the TiO₂ films were doped at very high levels (from 0.1% to 10%). However, few studies have been reported about TiO₂ doped at parts per million

(ppm) level applied as photoanode of DSSCs. Xie et al. [10] have found that trace amount of Cr-doping TiO₂ films could improve the efficiency of DSSCs. The improvement was ascribed to Cr additions offers more electrons for TiO₂ and increases the property of electron transport for DSSCs. As we all know, doping semiconductors at parts per million (ppm) level is the most common approach for enhancing the Fermi energy level of semiconductors and then increasing their conductivity (for instance, Si).

In this paper, a series of Ca-doped TiO₂ films were synthesized by hydrothermal method and were successfully applied as the photoanode materials in DSSCs, and the short-circuit current densities (*J*_{sc}) and photoelectric conversion efficiencies of DSSCs were found to be increased by trace amount doping in TiO₂. The change in performance of DSSCs employing Ca-doped TiO₂ films with different concentrations was obvious. We can conclude that the intrinsic increases in the photocurrent and photoelectric conversion efficiency are primarily related to faster electron transport in the Ca-doped TiO₂ film. The effects caused by Ca doping on electron collection, transfer, and recombination of the DSSCs are discussed below.

2. Experimental Section

2.1. Preparation of Undoped TiO_2 and Ca-Doped TiO_2 Pastes. Titanium isopropoxide (TTIP) was used as Ti precursors and calcium nitrate ($\text{Ca}(\text{NO}_3)_2 \cdot 4\text{H}_2\text{O}$) was the Ca sources. Pure TiO_2 and Ca-doped TiO_2 pastes were synthesized by a hydrothermal treatment method. The hydrothermal solutions were synthesized as follows [11].

- (i) 2.1 g acetic acid was added dropwise into 10 mL of TTIP. Subsequently, the mixture was added to 50 mL of deionized water mixed with different amounts of $\text{Ca}(\text{NO}_3)_2 \cdot 4\text{H}_2\text{O}$ (Ca/ TiO_2 molar ratio: undoped, 20 ppm, 50 ppm, 70 ppm, and 100 ppm) with rapid stirring for 1 h. Then, 0.68 mL of nitric acid was added to the obtained mixture solution. After continuous stirring at 80°C for 2–3 h, a transparent mixture solution was obtained.
- (ii) The transparent mixture solution was filtered to remove insoluble impurities and transferred into an autoclave at 220°C for 12 h. After cooling to room temperature, 0.4 mL of nitric acid was added into the colloid, using ultrasonicator to disperse.
- (iii) The colloid was concentrated to 20 mL by rotary evaporator. Finally, PEG and Triton X-100 were added to form TiO_2 paste. The obtained pastes were denoted as undoped TiO_2 , Ca-1: 20 ppm Ca-doped TiO_2 , Ca-2: 50 ppm Ca-doped TiO_2 , Ca-3: 70 ppm Ca-doped TiO_2 , and Ca-4: 100 ppm Ca-doped TiO_2 .

Following the procedure described, a total of five pastes with different concentrations of Ca were prepared.

2.2. Fabrication of Photoelectrodes and DSSCs. The FTO glass was used as substrate after careful cleaning. The pure TiO_2 and Ca-doped TiO_2 pastes were coated onto FTO substrates using a doctor-blade method, respectively. Next, the photoelectrodes were sintered at 500°C for 30 min to obtain the mesoporous TiO_2 film photoelectrodes. The thicknesses of these films were around $8\ \mu\text{m}$ measured with a TalyForm S4C-3D profilometer. They were dipped into a 0.5 mM N719 dye solution for 24 h at room temperature, and the excessive dye was washed away by using ethanol, followed by drying at 60°C . The platinum-coated FTO was used as the counter. A drop of electrolyte solution was injected into the photoelectrode and then the counter was clamped onto the photoelectrode; the electrolyte solution consisted of 0.05 mM LiI, 0.03 M I_2 , 0.1 M PMII (1-methyl-3-propyl imidazolium iodide), 0.1 M GNCS, and 0.5 M TBP in mixed solvent of acetonitrile and PC (volume ratio: 1/1). A sandwich-type DSSC configuration was fabricated.

2.3. Measurements. Photovoltaic measurements were performed by a CHI660C electrochemical workstation (CH Instruments, Shanghai, China) at room temperature. The irradiated area of each cell was kept at $0.25\ \text{cm}^2$ by using a light-tight metal mask. Electrochemical impedance spectroscopy (EIS) technique [12] was employed to investigate the electron transport in DSSCs.

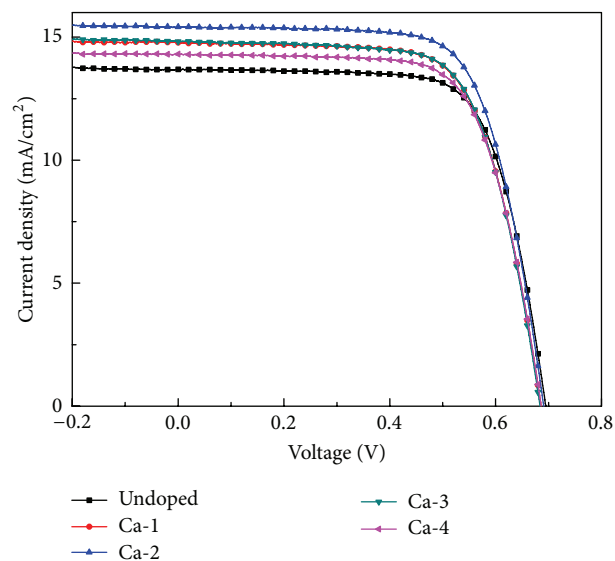


FIGURE 1: J - V characteristics of DSSCs based on the undoped and Ca-doped TiO_2 photoanodes.

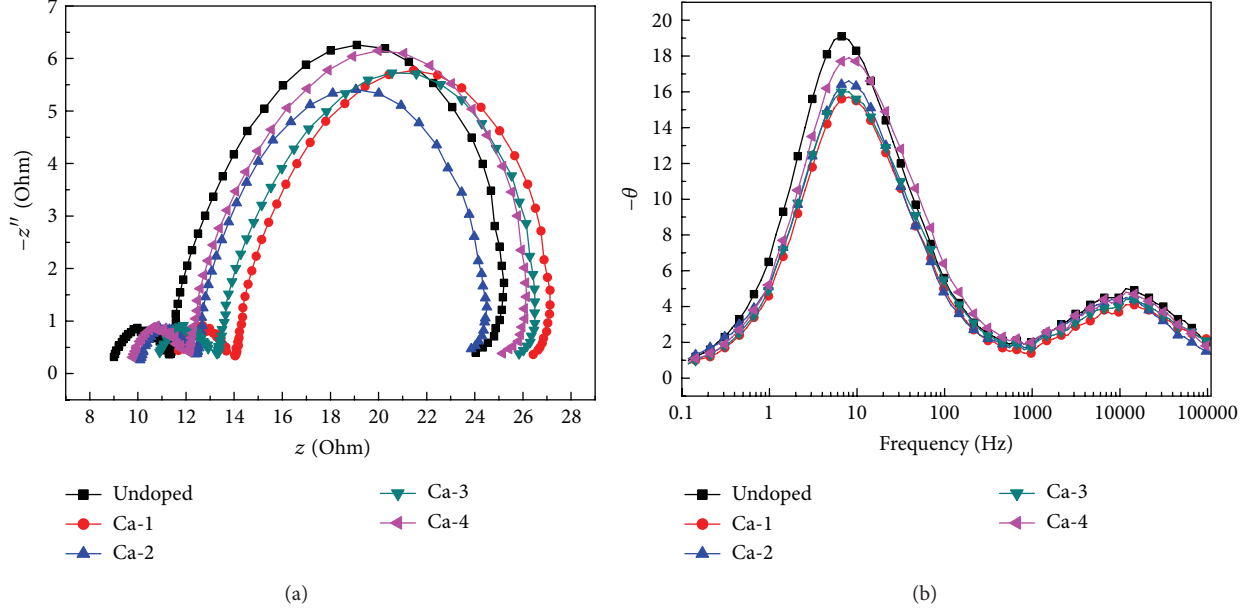
3. Results and Discussion

3.1. J - V Characteristics. The photocurrent density-voltage (J - V) characteristics of the DSSCs based on the pure TiO_2 film photoelectrodes and Ca-doped TiO_2 film photoelectrodes are shown in Figure 1. The average performance characteristics obtained from multiple cells with the same Ca content were summarized in Table 1, which shows the correlation between the photovoltaic performance parameters and the Ca content in the TiO_2 . The best photovoltaic performance was obtained from 50 ppm Ca-doped TiO_2 . Obviously, as can be seen from the graph, the energy conversion efficiency (η) went up with the increase of Ca content, which was attributed to the enhancement of the short-circuit current density (J_{sc}). The J_{sc} of DSSCs based on 50 ppm Ca-doped TiO_2 was $15.42\ \text{mA}\cdot\text{cm}^{-2}$, which was 12.7% higher than that of undoped cells. The energy conversion efficiency of 7.58% was achieved for cells based on 50 ppm Ca-doped TiO_2 electrode, which accounts for 9.88% higher than that of undoped cells. The effect on open-circuit voltage (V_{oc}) and fill factor as a result of such a little amount of Ca-doping was negligible. The energy conversion efficiency (η) increases gradually with the increase of Ca content and reaches an optimum value coinciding with Ca quantity of 50 ppm. However, the higher Ca amounts (>50 ppm) cause electron scattering and trap electrons which increase dark current. As a result, the energy conversion efficiency of DSSCs begin to fall.

3.2. Electrochemical Impedance Spectroscopy Analysis of DSSCs. To investigate the difference of the charge transport properties between pure DSSCs and Ca-doped DSSCs, we performed electrochemical impedance spectroscopy (EIS) analysis. EIS has been widely employed to investigate the electron transport in DSSCs, for example, measuring the respective time constants for charge combination and for the

TABLE 1: Performance of DSSCs based on undoped and Ca-doped TiO₂ photoanodes.

DSSCs	Doping/ppm	V_{oc}/mV	$J_{sc}/mAcm^2$	FF	$\eta/\%$	R_{ct}/Ω	η_{cc}
Undoped	0	695	13.68	0.71	6.78	7.34	0.75
Ca-1	20	686	14.78	0.69	7.00	7.32	0.73
Ca-2	50	691	15.42	0.70	7.45	5.24	0.80
Ca-3	70	684	14.82	0.70	7.00	8.09	0.72
Ca-4	100	686	14.32	0.69	6.84	7.30	0.73

FIGURE 2: EIS of DSSCs based on the undoped and Ca-doped TiO₂ photoanodes measured in the illumination at the applied bias of V_{oc} (a) Nyquist plots and (b) Bode phase plots.

combined processes of charge collection. From the measured spectra of EIS, we can get reliable value of the parameter. Figure 2 shows the EIS spectra of pure DSSCs and Ca-doped DSSCs, the impedance spectra of DSSCs based on the pure TiO₂ and Ca-doped TiO₂ were measured from 0.1 to 10⁵ Hz in the illumination at the applied bias of V_{oc} . The spectra are composed of two semicircles: the small semicircle in the high frequency range of 10³ to 10⁵ Hz fitted to a charge transfer resistance (R_{ct}) at the interfaces of the redox electrolyte/Pt counter electrode and FTO/TiO₂ and the large semicircle in the frequency range of 1 to 10³ Hz fitted to a transport resistance (R_w), which is related to the charge transport resistance of the accumulation/transport [13] of the injected electrons within TiO₂ film and the charge transport resistance at the TiO₂/redox electrolyte interfaces. This large semicircle is the major concern here. As shown in Figure 2, the large semicircle got smaller with the increase of Ca in TiO₂ films. This change reflected the acceleration of electron transport process in TiO₂ photoanode. The modeled internal resistances of the DSSCs based on five different electrodes are exhibited in Table 2, in which t_r is the electron transport time, t_c is the electron lifetime, R_w is charge transport resistance, and η_{cc} is the charge collection efficiency of DSSCs.

The apparent value of η_{cc} can be estimated on the basis of the t_r and t_c data from the following [14]:

$$\eta_{cc} = 1 - \frac{t_r}{t_c}. \quad (1)$$

The electron transport time constants for Ca-doped TiO₂ films decrease, which indicates the electrons transport faster in the Ca-doped TiO₂ films than the undoped TiO₂ films. This enhanced the charge collection efficiency η_{cc} and led to higher current density (J_{sc}) of DSSCs. The electron life time constants for the Ca-doped TiO₂ films also slightly decrease. The electron lifetime in DSSCs is determined by the characteristic frequency peak in the low frequency (f_{max}) according to the following equation [15]:

$$\tau_e = \frac{1}{2\pi f_{max}}. \quad (2)$$

The shorter electron life time indicates the faster recombination rate in the Ca-doped TiO₂ films, and that could be attributed to impurities of Ca-doping, which acts as a charge trapping site for the electron-hole recombination. The electron lifetime decreases slightly, so we concluded

TABLE 2: The mean electron life time (t_r), the mean electron transit time (t_c), and the charge collection efficiency (η_{cc}) of DSSCs based on undoped and Ca-doped TiO₂ photoanodes.

DSSCs	Doping/ppm	R_w/Ω	t_r/ms	t_c/ms	η_{cc}
Undoped	0	7.36	0.0350	0.0088	0.75
Ca-1	20	7.32	0.0290	0.0077	0.73
Ca-2	50	5.24	0.0294	0.0059	0.80
Ca-3	70	7.27	0.0290	0.0076	0.72
Ca-4	100	8.09	0.0290	0.0080	0.73

that less photogenerated electrons are captured by empty trap states in the Ca-doped TiO₂ films [16], and this result favors the electron transport. The improvement of electron transport ability was helpful to increase the short-circuit current density (J_{sc}), resulting in higher conversion efficiency.

4. Conclusion

In summary, the Ca-doping TiO₂ nanoparticles were successfully applied as the photoanode material in DSSCs. By comparing the Ca-doping TiO₂ with undoping TiO₂, a faster electron transport and shorter lifetime existed for the Ca-doping DSSCs. Moreover, the higher electron transport rates of Ca-doped TiO₂ photoanode can improve the charge collection efficiency and thus lead to higher short-circuit photocurrent density of DSSCs. The best photovoltaic performance was obtained from 50 ppm Ca-doping with the conversion efficiency of 7.45%. This value was 9.88% higher than that of the undoped device. The short-circuit current density (J_{sc}) was increased due to the faster electron transport in the Ca-doped TiO₂ film. We can conclude that Ca-doped TiO₂ is a better photoanode material and a more promising alternative for high efficient DSSCs than pure TiO₂.

Conflict of Interests

The authors do not have any conflict of interests in their submitted paper.

Acknowledgments

We acknowledge the supported of the National Natural Science Foundation of China (Grant no. 11364014), the National Science Foundation of Hainan Province, China (Grant no. 113005), and Physics Graduate Project of Hainan Normal University (20140092102).

References

- [1] H. Yu, S. Q. Zhang, H. J. Zhao, B. Xue, P. Liu, and G. Will, "High-performance TiO₂ photoanode with an efficient electron transport network for dye-sensitized solar cells," *The Journal of Physical Chemistry C*, vol. 113, no. 36, pp. 16277–16282, 2009.
- [2] F. R. Li, G. C. Wang, and Y. Jiao, "Efficiency enhancement of ZnO-based dye-sensitized solar cell by hollow TiO₂ nanofibers," *Journal of Alloys and Compounds*, vol. 611, no. 5, pp. 19–23, 2014.
- [3] H. K. Wang and A. L. Rogach, "Hierarchical SnO₂ nanostructures: recent advances in design, synthesis, and applications," *Chemistry of Materials*, vol. 26, no. 1, pp. 123–133, 2014.
- [4] M. Quintana, T. Edvinsson, A. Hagfeldt, and G. Boschloo, "Comparison of dye-sensitized ZnO and TiO₂ solar cells: studies of charge transport and carrier lifetime," *The Journal of Physical Chemistry C*, vol. 111, no. 2, pp. 1035–1041, 2007.
- [5] C. N. Zhang, S. H. Chen, L.-E. Mo et al., "Charge recombination and band-edge shift in the dye-sensitized Mg²⁺-doped TiO₂ solar cells," *The Journal of Physical Chemistry C*, vol. 115, no. 33, pp. 16418–16424, 2011.
- [6] J. Y. Zhang, Z. Y. Zhao, X. Y. Wang et al., "Increasing the oxygen vacancy density on the TiO₂ surface by La-doping for dye-sensitized solar cells," *The Journal of Physical Chemistry C*, vol. 114, no. 43, pp. 18396–18400, 2010.
- [7] Q. H. Yao, J. F. Liu, Q. Peng, X. Wang, and Y. Li, "Nd-doped TiO₂ nanorods: preparation and application in dye-sensitized solar cells," *Chemistry*, vol. 1, no. 5, pp. 737–741, 2006.
- [8] J. Liu, H. T. Yang, W. W. Tan, X. Zhou, and Y. Lin, "Photovoltaic performance improvement of dye-sensitized solar cells based on tantalum-doped TiO₂ thin films," *Electrochimica Acta*, vol. 56, no. 1, pp. 396–400, 2010.
- [9] W. Guo, L. Q. Wu, Z. Chen, G. Boschloo, A. Hagfeldt, and T. Ma, "Highly efficient dye-sensitized solar cells based on nitrogen-doped titania with excellent stability," *Journal of Photochemistry and Photobiology A: Chemistry*, vol. 219, no. 2-3, pp. 180–187, 2011.
- [10] Y. N. Xie, N. Huang, S. J. You et al., "Improved performance of dye-sensitized solar cells by trace amount Cr-doped TiO₂ photoelectrodes," *Journal of Power Sources*, vol. 224, no. 10, pp. 168–173, 2013.
- [11] Z. F. Tong, T. Peng, W. W. Sun et al., "Introducing an intermediate band into dye-sensitized solar cells by W⁶⁺ doping into TiO₂ nanocrystalline photoanodes," *Journal of Physical Chemistry C*, vol. 24, no. 5, 2014.
- [12] M. Adachi, M. Sakamoto, J. Jiu, Y. Ogata, and S. Isoda, "Determination of parameters of electron transport in dye-sensitized solar cells using electrochemical impedance spectroscopy," *The Journal of Physical Chemistry B*, vol. 110, no. 28, pp. 13872–13880, 2006.
- [13] Q. Wang, J.-E. Moser, and M. Grätzel, "Electrochemical impedance spectroscopic analysis of dye-sensitized solar cells," *The Journal of Physical Chemistry B*, vol. 109, no. 31, pp. 14945–14953, 2005.
- [14] K.-P. Wang and H. Teng, "Zinc-doping in TiO₂ films to enhance electron transport in dye-sensitized solar cells under low-intensity illumination," *Physical Chemistry Chemical Physics*, vol. 11, no. 41, pp. 9489–9496, 2009.

- [15] N.-G. Park, J. van de Lagemaat, and A. J. Frank, "Comparison of dye-sensitized rutile- and anatase-based TiO_2 solar cells," *The Journal of Physical Chemistry B*, vol. 104, no. 38, pp. 8989–8994, 2000.
- [16] Y. D. Duan, N. Q. Fu, Q. P. Liu et al., "Sn-doped TiO_2 photoanode for dye-sensitized solar cells," *The Journal of Physical Chemistry C*, vol. 116, no. 16, pp. 8888–8893, 2012.

Research Article

Multiwalled Carbon Nanotube-TiO₂ Nanocomposite for Visible-Light-Induced Photocatalytic Hydrogen Evolution

Ke Dai,¹ Xiaohu Zhang,² Ke Fan,² Peng Zeng,² and Tianyou Peng²

¹ College of Resources and Environment, Huazhong Agricultural University, Wuhan 430070, China

² College of Chemistry and Molecular Science, Wuhan University, Wuhan 430072, China

Correspondence should be addressed to Ke Dai; dk@mail.hzau.edu.cn and Tianyou Peng; typeng@whu.edu.cn

Received 15 May 2014; Revised 5 July 2014; Accepted 17 July 2014; Published 10 August 2014

Academic Editor: Xiaohu Huang

Copyright © 2014 Ke Dai et al. This is an open access article distributed under the Creative Commons Attribution License, which permits unrestricted use, distribution, and reproduction in any medium, provided the original work is properly cited.

Multiwalled carbon nanotube- (MWCNT-) TiO₂ nanocomposite was synthesized via hydrothermal process and characterized by X-ray diffraction, UV-vis diffuse reflectance spectroscopy, field emission scanning electron microscope, thermogravimetry analysis, and N₂ adsorption-desorption isotherms. Appropriate pretreatment on MWCNTs could generate oxygen-containing groups, which is beneficial for forming intimate contact between MWCNTs and TiO₂ and leads to a higher thermal stability of MWCNT-TiO₂ nanocomposite. Modification with MWCNTs can extend the visible-light absorption of TiO₂. 5 wt% MWCNT-TiO₂ derived from hydrothermal treatment at 140°C exhibiting the highest hydrogen generation rate of 15.1 μmol·h⁻¹ under visible-light irradiation and a wide photoresponse range from 350 to 475 nm with moderate quantum efficiency (4.4% at 420 nm and 3.7% at 475 nm). The above experimental results indicate that the MWCNT-TiO₂ nanocomposite is a promising photocatalyst with good stability and visible-light-induced photoactivity.

1. Introduction

Hydrogen resource obtained directly from water splitting using photocatalyst and solar light is under scrutiny as a clean energy resource; however it has been facing technical challenge to find a stable and efficient photocatalyst that can maximally utilize solar light [1]. In addition to oxide semiconductors, a great variety of novel photoactive semiconductors have been developed in the last few years. Among these, mixed oxides of transition metal like Nb, V, or Ta or with main group elements such as Ga, In, Sb, or Bi have been extensively investigated as attractive candidates for visible-light-induced photocatalysis [2]. Also, sulfides and nitrides of different metals have been frequently selected to obtain materials with visible-light-driven photoactivity [3]. Titania (TiO₂) is a widely used photocatalyst due to its high chemical stability, low cost, and nontoxic nature [4], but it can only absorb UV light with low quantum efficiency due to its wide bandgap (*ca.* 3.2 eV), which limits its application in visible-light-driven photocatalysis. The above problems have been partly resolved by many methods, such as surface modification via organic materials [5], semiconductor coupling [6],

bandgap modification by nonmetals [7, 8], and plasmonic metal (Ag and Au) doping [9–14], creating oxygen vacancies and disorder or dye sensitization [15–17].

Due to the special structures and extraordinary mechanical and unique electronic properties, carbon nanotubes (CNTs) have the potential to extend the photoresponse range of TiO₂ to visible-light region by modification of bandgap and/or sensitization and increase the photoactivity of TiO₂ by contribution to high surface area and inhibition of electron-hole recombination [18]. Single-walled carbon nanotubes (SWCNTs) have shown a synergy effect on enhancing photoactivity for H₂ evolution over a mixture of SWCNTs and TiO₂ [19]. Ou et al. [20] have also demonstrated that multiwalled carbon nanotubes (MWCNTs) could enhance the visible-light-driven photoactivity of TiO₂ by acting as a photosensitizer in the MWCNT-TiO₂:Ni composite. MWCNT-TiO₂ nanocomposite with visible-light-driven photoactivity was successfully synthesized via direct growth of TiO₂ nanoparticles on the surface of the functionalized MWCNTs by the hydrothermal treatment in our group [21]. However, the effects of MWCNT pretreatment, MWCNT content, and

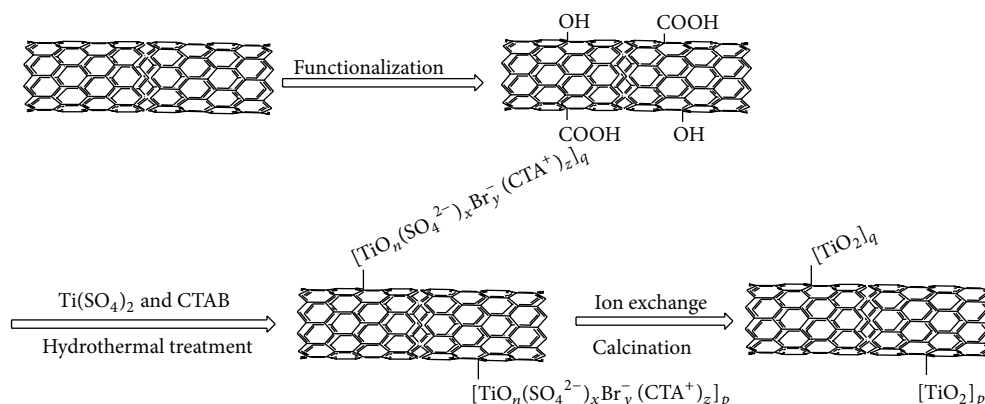


FIGURE 1: Schematic formation model for MWCNT-TiO₂ nanocomposite.

synthetic conditions of MWCNT-TiO₂ nanocomposite on its photocatalytic hydrogen evolution efficiency and quantum efficiency under monochromatic light irradiation are still beyond our knowledge.

Herein, MWCNT-TiO₂ nanocomposite was synthesized, characterized, and employed for photocatalytic H₂ production from triethanolamine (TEOA) solution. The effects of pretreatment methods, content of MWCNTs, and hydrothermal temperature on the photocatalytic H₂ evolution efficiency over the Pt-loaded photocatalysts were studied. Moreover, the apparent quantum efficiency (AQE) of 5 wt% MWCNT-TiO₂ upon incident monochromatic light is also investigated.

2. Experiment

2.1. Pretreatment Methods for MWCNTs. MWCNTs (diameter < 8 nm; length 10–30 μm; purity > 95 wt%) were purchased from Chengdu Organic Chemicals (Chinese Academy Science, China), and were functionalized by different methods: the as-received MWCNTs were chemically oxidized in a mixture of sulfuric acid and nitric acid (3/1, v/v) while being ultrasonicated for 2 h (Method A [22]); the as-received MWCNTs were treated in boiled nitrate solution (20 wt%) for 1 h for surface functionalization (Method B [21]); the as-received MWCNTs were dispersed in 5.0 M HNO₃ solution and refluxed for 48 h at 140°C (Method C). These functionalized MWCNTs were washed with water to neutral, dried under vacuum, and denoted as MWCNT (A), MWCNT (B), and MWCNT (C), respectively.

2.2. Preparation and Characterization of MWCNT-TiO₂ Nanocomposites. All other chemical reagents used in the study were of analytical grade and used without further purification, unless stated otherwise. The preparation procedure for MWCNT-TiO₂ nanocomposites is demonstrated in Figure 1. In a typical experiment, pretreated MWCNTs were ultrasonically dispersed in deionized water, and then titanium sulfate ($\text{Ti}(\text{SO}_4)_2$) was added into the dispersion under stirring. The obtained mixture was added into cetyltrimethylammonium bromide (CTAB) solution under the molar ratio

of $\text{Ti}(\text{SO}_4)_2$: CTAB : H₂O is 1 : 0.12 : 100. After stirring, the resulting mixture (pH 0.2) was aged at room temperature for 12 h and then transferred into an autoclave for 72 h hydrothermal treatment at 100°C. The resulting materials were collected using the centrifugation technique and mixed with a water and ethanol (molar ratio 1 : 1) solution of sodium chloride under stirring at 40°C for 5 h. Resultant sample was washed with water and ethanol, dried at 80°C overnight, and calcined at 400°C for 5 h.

X-ray diffraction (XRD) patterns were obtained on a XRD-6000 diffractometer using Cu Kα as radiation ($\lambda = 0.15418$ nm). Scanning electron microscope (SEM) observation was conducted on a JEOL-6700F electron microscope. Diffuse reflectance spectra (DRS) were recorded on a Cary 5000 UV-Vis-NIR spectrophotometer equipped with an integrating sphere (Varian, USA). Thermogravimetry (TG) curves were recorded on a STA 449C thermal analyzer (Netzsch, Germany). The Brunauer-Emmett-Teller (BET) surface areas were analyzed by nitrogen adsorption-desorption measurement using a Micromeritics ASAP 2020 apparatus after the samples were degassed at 180°C.

2.3. Photocatalytic Activity Measurement. The obtained MWCNT-TiO₂ nanocomposite was loaded with Pt and tested for its photocatalytic activity through a photocatalytic hydrogen evolution system as described in our previous publication [21, 23]. A 300 W Xe-lamp (PLS-SXE300C, Beijing Trusttech Co., Ltd., China) was applied as the light source, which was collimated and focalized into 5 cm² parallel faculae. A cut-off filter (Kenko, L-42; $\lambda > 420$ nm) was employed to obtain the visible-light irradiation ($\lambda > 420$ nm). The reaction was performed in a water suspension which contains 85 mL water, 15 mL triethanolamine (TEOA), and 40 mg photocatalyst. The suspension was irradiated from top of the system after thoroughly removing air. H₂ production rate was analyzed with a gas chromatograph (GC, SP-6800A, TCD detector, 5 Å molecular sieve columns, and Ar carrier).

The apparent quantum efficiency (AQE) was measured under the same photocatalytic reaction condition except for

TABLE 1: Summary of the physicochemical properties of MWNT and MWNT-TiO₂ nanocomposite.

Sample	Crystal size ^a (nm)	C _{TG} ^b (wt%)	S _{BET} (m ² /g)	Mean pore size ^c (nm)	Total volume ^d (cm ³ /g)
1.25 wt% MWNT-TiO ₂	12.8	1.5	110.8	10.9	0.35
2.5 wt% MWNT-TiO ₂	12.1	3.2	97.5	12.4	0.36
5 wt% MWNT-TiO ₂	12.9	5.7	79.8	12.1	0.28
10 wt% MWNT-TiO ₂	12.6	9.9	110.1	11.8	0.37
20 wt% MWNT-TiO ₂	11.8	18.5	166.7	9.1	0.42
MWNT	—	—	392.5	7.6	0.74

^aCalculated by the Scherrer equation.

^bCarbon content determined by TGA-DSC analyses.

^cAverage pore diameter calculated from BJH desorption average pore width (4 V/A).

^dSingle point total pore volume at the relative pressure of *ca.* 0.995.

the incident monochromatic light wavelength. The hydrogen yields of 1 h photocatalytic reaction under visible-light with different wavelengths of 350, 365, 380, 420, 435, 450, 475, 500, 520, and 550 nm were measured. Each run was carried out three times and the average value was taken (the relative errors are under 10%). The band-pass and cut-off filters and a calibrated Si photodiode (SRC-1000-TC-QZ-N, Oriel, USA) were used in measurement. Apparent quantum efficiencies at different wavelengths were calculated by the following equation:

$$\begin{aligned}
 \text{AQE (\%)} &= \frac{\text{The number of reacted electrons}}{\text{The number of incident photons}} \times 100 \\
 &= \frac{2 \times \text{The number of evolved H}_2 \text{ molecules}}{\text{The number of incident photons}} \times 100.
 \end{aligned} \quad (1)$$

3. Results and Discussion

Figure 2 shows the XRD patterns of MWCNT, TiO₂, and various MWCNT-TiO₂ nanocomposites. As can be seen from Figure 2(a), the main diffraction peaks of various products can be ascribed to anatase TiO₂, whereas a decrease in the crystallinity of anatase can be found after the introduction of MWCNTs, indicating the decrease in the grain size of TiO₂. The characteristic peaks for CNTs at $2\theta = 26.0^\circ$ and 43.4° were not observed for 1.25–10 wt% MWCNT-TiO₂, which is different from the previous observation [24]. This phenomenon could be attributed to the good dispersion of MWCNTs in the nanocomposite after surface functionalization in nitrate solution [21]. Average crystal sizes calculated using Scherrer equation [25] from the broadening of the (101) peaks of the anatase are 18.1, 12.8, 12.1, 12.9, 12.6, and 11.8 nm for TiO₂ and 1.25–20 wt% MWCNT-TiO₂, respectively (see Table 1). The small grain of TiO₂ nanoparticles in MWCNT-TiO₂ may be attributed to restricted direct contact of grains due to the presence of MWCNTs.

As can be observed from Figure 2(b), even for MWCNT-TiO₂ calcined at 800°C for 5 h, the XRD pattern shows that all of the crystal phases are still anatase; no peak of rutile appears. Average crystal sizes calculated from the broadening of the (101) peaks of the anatase are 11.6, 12.9, 13.6, 17.8, and 32.9 nm for the 5 wt% MWCNT-TiO₂ as-synthesized and calcined at

400, 500, 600, and 800°C, respectively. These results suggest that MWCNTs in the nanocomposite probably inhibit the phase transformation of TiO₂ from amorphous phase to anatase phase and lead to a higher thermal stability.

To estimate the real content of MWCNTs in composites, 1.25–10 wt% MWCNT-TiO₂ were analyzed by TGA technique. The results shown in Table 1 suggest that the MWCNT/TiO₂ ratios estimated before the synthesis of the MWCNT-TiO₂ were consistent with the results obtained from TGA analysis. Therefore, negligible losses of MWCNTs occurred during the nanocomposite preparation procedure, which is in accordance with the results of Raman analysis on 5 wt% MWCNT-TiO₂ [21]. The BET specific surface areas and pore volumes of the samples are summarized in Table 1. Compared with mesoporous TiO₂ nanoparticles prepared via hydrothermal processes [26], there is a rapid decrease in both BET surface area (from 318 to 111 m²/g) and total volume (from 0.61 to 0.35 cm³/g) of TiO₂ nanoparticles after modification with 1.25 wt% MWCNT, which could be due to the close-packed structure between TiO₂ nanoparticles and MWCNTs. With increasing MWCNT content, the BET surface area of MWCNT-TiO₂ decreased firstly and then increased, which can be attributed to the destruction of close-packing due to the self-agglomeration of MWCNTs or TiO₂ nanoparticles at high content.

The UV-vis spectra of MWCNT-TiO₂ display a similar absorption edge to TiO₂ (Figure 3), but an apparent enhancement of absorption throughout the visible-light region can be observed even for the nanocomposite containing 1.25 wt% MWCNTs. A correlation between the MWCNTs amount and absorption changes in the UV-vis spectra obviously features the enhancement of visible-light absorption upon increasing the MWCNT content; that is, the adsorption intensity of the present MWCNT-TiO₂ continuously increased with enhancing MWCNT content owing to its good dispersion.

Control experiments showed no appreciable H₂ evolution in the absence of either photocatalyst or irradiation under visible-light or full spectra irradiation. H₂ generation rates over 5 wt% MWCNT + TiO₂ (a simple mixture of MWCNTs and TiO₂ nanoparticles), 5 wt% MWCNT-TiO₂, TiO₂, and MWCNTs under the visible-light and full spectra irradiation are shown in Figure 4. The pristine TiO₂ and MWCNTs as well as the MWCNT + TiO₂ demonstrate no appreciable H₂ evolution under the visible-light irradiation, whereas

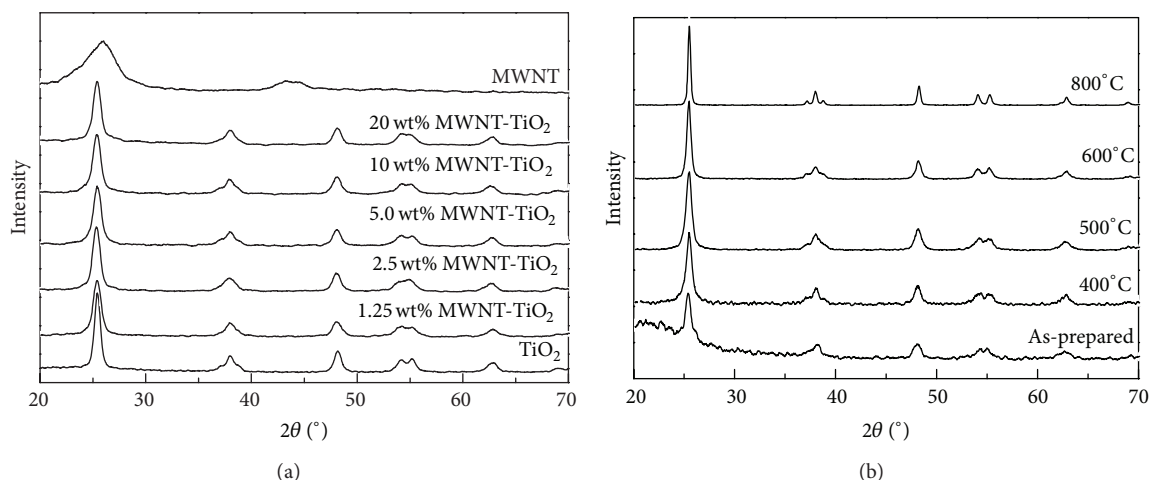


FIGURE 2: XRD patterns of MWCNT, TiO_2 , and MWCNT- TiO_2 with (a) different MWCNT content; (b) 5 wt% MWCNT and calcination at different temperatures.

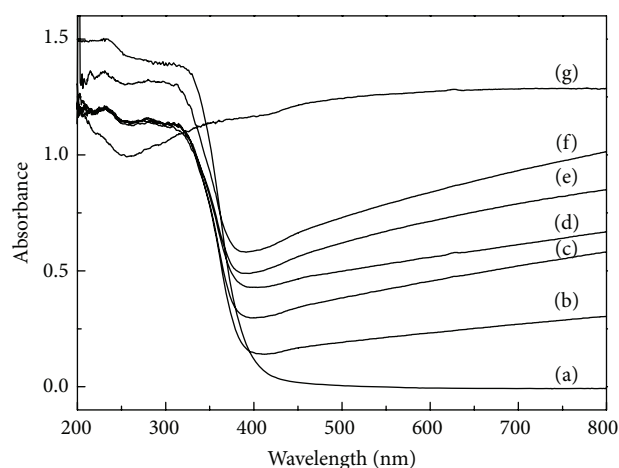


FIGURE 3: DRS patterns of MWCNT, TiO_2 , and MWCNT- TiO_2 with different MWCNT content. (a) TiO_2 ; (b) 1.25 wt%; (c) 2.5 wt%; (d) 5 wt%; (e) 10 wt%; (f) 20 wt%; (g) MWCNT.

MWCNT- TiO_2 (A, B, and C) exhibits various H_2 generation rates, suggesting the importance of chemical linking between MWCNTs and TiO_2 for their visible-light-driven photoactivity [27]. The pretreatment of MWCNTs has a strong effect on the photocatalytic H_2 evolution efficiency over MWCNT- TiO_2 . MWCNT- TiO_2 (B) demonstrates the highest H_2 evolution rate under both visible-light and full spectra irradiation.

Different oxidizing reagents possess different degrees of oxidation power, which would purify and decorate MWCNTs with oxygen-containing groups or even destroy their nanotube structure [28]. It is reported that MWCNT bundles appear exfoliated and curled after treatment with strong oxidative environment such as refluxing in nitric acid or stirring in piranha (mixture of sulphuric acid 96 wt% and hydrogen peroxide 30 wt% in ratio 70:30) [29]. Comparing

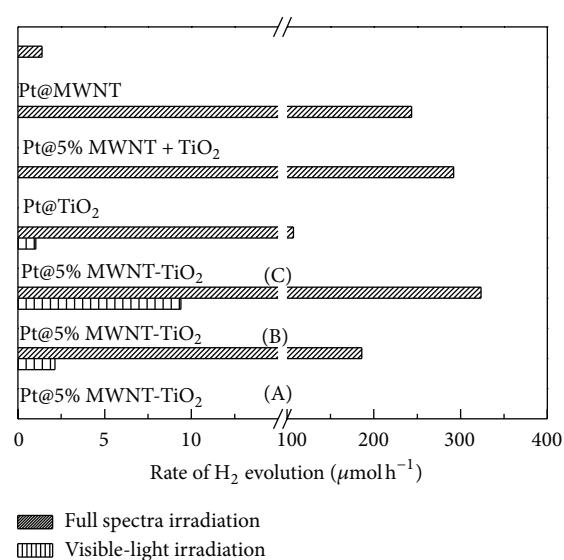


FIGURE 4: H_2 evolution efficiency over MWCNT, TiO_2 , and various photocatalysts containing MWCNT and TiO_2 under visible-light ($\lambda > 420 \text{ nm}$) and full spectra irradiation. Conditions: 1 wt% Pt-loading; 15 vol % TEOA solution (100 mL); light source, 300 W Xe-lamp. MWCNTs + TiO_2 : MWCNTs and TiO_2 nanoparticles were simply mixed together.

the method of refluxing in nitric acid with that of sonicating in a mixture of sulfuric acid and nitric acid, the method of refluxing in nitrate solution provides a moderate oxidation that would generate oxygen-containing groups but would not destroy the MWCNTs structure. Therefore, MWCNT- TiO_2 (B) exhibited the highest photoactivity.

As demonstrated in Figure 5, MWCNT- TiO_2 exhibits no photocatalytic activity until the MWCNT content enhanced to 3.5 wt% under visible-light irradiation. After that, its photocatalytic H_2 evolution efficiency increases firstly

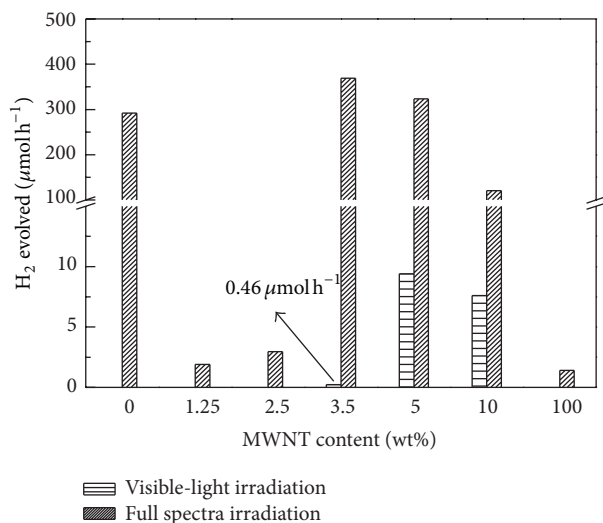


FIGURE 5: The rate of H_2 evolution on MWCNT-TiO₂ nanocomposites with different MWCNT content under visible-light ($\lambda > 420$ nm) and full spectra irradiation. Conditions: 1 wt% Pt-loading; 15 vol % TEOA solution (100 mL); light source, 300 W Xe-lamp.

and then decreases slightly with further enhancement of the MWCNT content. The maximum efficiency is achieved at 5 wt% MWCNT-TiO₂ under visible-light irradiation.

It is believed that TiO₂ nanoparticles could directly grow on the surface of the functionalized MWCNTs through the hydrothermal treatment [21]. As shown in Figure 6, no MWCNTs were found in the SEM micrograph of 2.5 wt% MWCNT-TiO₂, which can be attributed to the fact that MWCNTs are embedded inside the nanocomposite by TiO₂ nanoparticles, resulting from the direct growth of TiO₂ on the surface of MWCNTs. For 5 wt% MWCNT-TiO₂, MWCNTs can be observed on the surface of nanocomposite owing to the increase of MWCNT content. These observations can fairly explain the effect of MWCNT content on the visible-light-induced photoactivity. For the MWCNT-TiO₂ with MWCNT content less than 3.5 wt%, MWCNTs embedded inside the nanocomposite cannot be irradiated and excited by visible-light, and thus no visible-light-induced photoactivity was observed [30]. As the visible-light absorbent and sensitizer, higher MWCNT content means more efficient visible-light absorption, and more photogenerated electrons can be transferred to TiO₂; TiO₂ also plays an important role in the separation of photogenerated carriers: the electrons can be transferred from TiO₂ to the loaded Pt. It is reported [31] that the electrical conductivity in the interfacial contact between graphene and photocatalyst components is vital to the overall photocatalytic H_2 production. In addition, unintentional doping of TiO₂ may happen under annealing at 400°C [32, 33], which can increase the visible-light absorbance of TiO₂ and MWCNT-TiO₂. Therefore, there exists an optimal ratio of MWCNT to TiO₂ for achieving excellent electrical conductivity in the nanocomposites and significant photoactivity for H_2 evolution [30].

Under full spectra irradiation, MWCNT-TiO₂ with small MWCNT contents (1.25 wt% and 2.5 wt%) exhibits lower

photoactivity than the pure titania, whereas 5 wt% and 3.5 wt% MWCNT-TiO₂ demonstrate the better and the best photoactivity, respectively. Carbon materials such as graphene, C₆₀, and CNT can act as electron traps due to their high electron affinities [31, 34, 35], which would be functionalized as charge separators and enhance the photoactivity [30, 36]. However, as discussed above, for the MWCNT-TiO₂ with MWCNT content less than 3.5 wt%, MWCNTs embedded inside the nanocomposite could act as recombination center of electron and holes, resulting in a reduced photoactivity under full spectra irradiation.

It is well understood that the hydrothermal temperature plays an important role in the morphology, crystallinity, and particle size of TiO₂ [37], which are related to the photoactivity. The effect of hydrothermal temperature on the H_2 generation rate was evaluated under visible-light irradiation. As demonstrated in Figure 7, the H_2 generation rate over 5 wt% MWCNT-TiO₂ increases with the enhanced hydrothermal temperature before 140°C and decreases afterwards under both visible-light and full spectra irradiation. The highest H_2 generation rate of 15.1 $\mu\text{mol}\cdot\text{h}^{-1}$ under visible-light irradiation was obtained with 140°C hydrothermal treatment, whereas that of 323.7 $\mu\text{mol}\cdot\text{h}^{-1}$ under full spectra irradiation was obtained with 100°C hydrothermal treatment.

The above experimental results could be rationalized by the following discussions. As can be seen from Figure 8, the XRD patterns of 5 wt% MWCNT-TiO₂ derived from different hydrothermal temperatures confirm the fact that the crystallinity of MWCNT-TiO₂ increases with enhancing hydrothermal temperature. It can be calculated using Scherrer equation [25] that average crystal sizes of the anatase are 8.3, 12.9, 15.7, and 26.7 nm for the 5 wt% MWCNT-TiO₂ with hydrothermal temperature of 80, 100, 140, and 180°C, respectively [38]. Under visible-light irradiation, MWCNTs, as a photosensitizer, can absorb visible-light and the photo-generated electrons (e^-) can be excited from the VB to CB of the MWCNT [39]. TiO₂, as the “bridge” between MWCNTs and loaded Pt, would transfer the photogenerated electrons from MWCNT to Pt nanoparticles to generate H_2 from water reduction [40]. As the electron acceptor and transfer station, TiO₂ with high crystallinity and tight combination with MWCNTs could benefit the electron injections and suppress the electron-hole recombination. On the other hand, high crystallinity of TiO₂ would inevitably lead to a large crystal size and particle size, which would lead to a high electron-hole recombination rate owing to the long distance for electron transfer. As a result, 5 wt% MWCNT-TiO₂ derived from hydrothermal treatment at 140°C has the highest photoactivity under visible-light irradiation.

Under full spectra irradiation, photocatalytic H_2 generation over TiO₂ irradiated by UV light would make the best part comparing to that over MWCNT-TiO₂ irradiated by visible-light. 5 wt% MWCNT-TiO₂ derived from hydrothermal treatment at 100°C possesses moderate crystal size of anatase, resulting in the highest photoactivity due to the large surface area of MWCNT-TiO₂ and low electron-hole recombination rate.

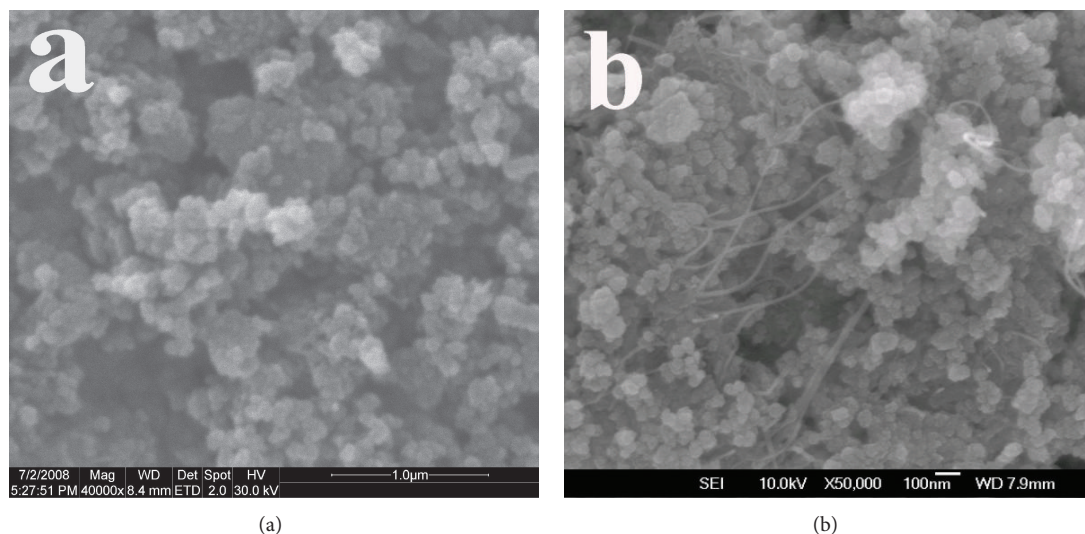


FIGURE 6: SEM micrographs of 2.5 wt% (a) and 5 wt% (b) MWCNT-TiO₂ nanocomposite.

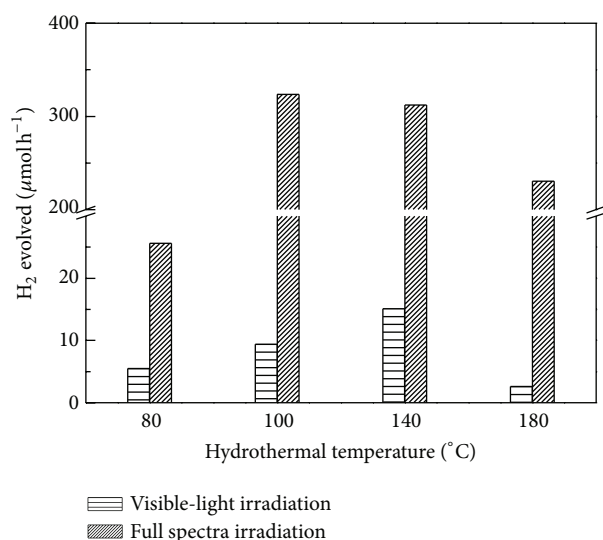


FIGURE 7: Effect of hydrothermal temperature on photocatalytic H₂ production over 5 wt% MWCNT-TiO₂.

The photocatalytic activities for H₂ production over 5 wt% MWCNT-TiO₂ upon incident light with different wavelength were investigated. MWCNT-TiO₂ shows a relatively wide photoresponse under monochromatic light of wavelength ranging from 350 to 475 nm (Figure 9), which is consistent with the experimental results obtained with visible-light irradiation (see Figure 4). The apparent quantum efficiency (AQE) of MWCNT-TiO₂ as a function of the wavelength of the incident light was calculated according to the data in Figure 9. MWCNT-TiO₂ demonstrates high quantum efficiency upon irradiation with wavelengths of 420 and 475 nm (4.4% and 3.7%, resp.). With respect to the wide adsorption band in the entire visible-light region (Figure 3), a panchromatic photocatalytic activity could be

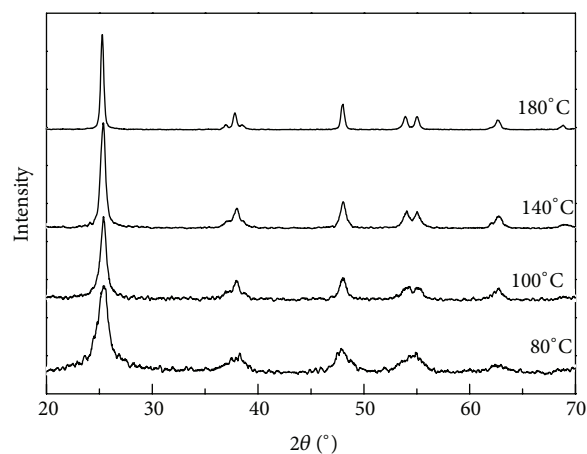


FIGURE 8: XRD patterns of 5 wt% MWCNT-TiO₂ derived from different hydrothermal temperatures for 72 h.

expected for 5 wt% MWCNT-TiO₂. However, no appreciable H₂ evolution is showed upon irradiation with wavelength longer than 500 nm. As demonstrated in our earlier study, not all MWCNTs in the nanocomposite are bound with TiO₂ nanoparticles, owing to the limited hydroxyl and carboxyl groups generated on the MWCNTs after the functionalization [21]. Therefore, the absorption band between 400 and 800 nm of MWCNT-TiO₂ nanocomposite probably is a combination of the absorption spectrum of both MWCNT-TiO₂ and uncoupled MWCNT, which would absorb light with wavelength longer than 500 nm but cannot be excited to generate electron-hole pairs. On the other hand, the energy of the incident light at longer wavelength dramatically decreased, which would inevitably depress the photoactivity over MWCNT-TiO₂. Furthermore, the photoactivity of TiO₂ under UV light irradiation is enhanced after coupling with MWCNT. The quantum efficiencies for H₂ production over

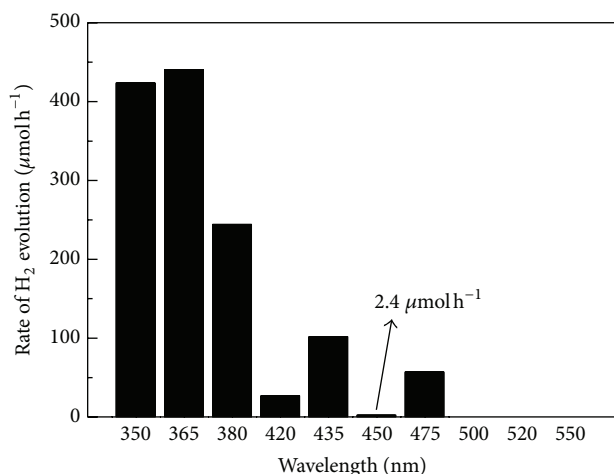


FIGURE 9: The dependence of photocatalytic activities for H₂ production over 5 wt% MWCNT-TiO₂ nanocomposite upon wavelength (controlled via cut-off filters).

P25 TiO₂, mesoporous TiO₂, and MWCNT-TiO₂ at 350 nm were measured to be 1.9, 2.5, and 3.8%, respectively. These phenomena were consistent with the previous discussion that MWCNTs could increase the carrier separation efficiency during photocatalytic process under full spectra irradiation.

4. Conclusions

A series of MWCNT-TiO₂ nanocomposites with different types of functionalized MWCNTs were synthesized through hydrothermal process and characterized by XRD, DRS, SEM, TGA, and BET techniques. The effects of pretreatment methods on MWCNT, MWCNT content, and hydrothermal temperature on the photocatalytic hydrogen evolution efficiency over MWCNT-TiO₂ nanocomposite were investigated. MWCNTs have a good dispersion in the nanocomposite, which inhibit grain growth of TiO₂ and improve its thermal stability. Appropriate pretreatment on MWCNTs could generate oxygen-containing groups, which would become the anchoring sites with TiO₂ nanoparticles in the nanocomposite. However, chemical pretreatment with strong oxidative agents would destroy the intrinsic structure of MWCNTs, which is not beneficial for a high photocatalytic activity. The best photocatalytic activity was observed for the MWCNT-TiO₂ nanocomposite with a 5% weight ratio under visible-light irradiation. The photocatalytic activity of MWCNT-TiO₂ is related to the crystallinity of TiO₂, link type between MWCNT and TiO₂, and MWCNT content. A wide range of photoresponse from 350 to 475 nm is observed with high quantum efficiency. Upon irradiation with wavelengths of 420 and 475 nm, the quantum efficiency is 4.4% and 3.7%, respectively. The above experimental results indicate that the present MWCNT-TiO₂ nanocomposite is a promising photocatalyst with good thermal stability, chemical stability under UV light irradiation, and visible-light-induced photoactivity.

Conflict of Interests

The authors declare that there is no conflict of interests regarding the publication of this paper.

Acknowledgments

The research was financially supported by the Natural Science Foundation of China (20973128, 21271146, and 21307035), Natural Science Foundation of Hubei Province (2011CDB139), and Fundamental Research Funds for Central Universities of China (2013PY112).

References

- [1] A. Kudo, "Development of photocatalyst materials for water splitting," *International Journal of Hydrogen Energy*, vol. 31, no. 2, pp. 197–202, 2006.
- [2] X. B. Chen, S. H. Shen, L. J. Guo, and S. S. Mao, "Semiconductor-based photocatalytic hydrogen generation," *Chemical Reviews*, vol. 110, no. 11, pp. 6503–6570, 2010.
- [3] M. Kitano and M. Hara, "Heterogeneous photocatalytic cleavage of water," *Journal of Materials Chemistry*, vol. 20, no. 4, pp. 627–641, 2010.
- [4] X. Liu, Z. Q. Liu, J. Zheng et al., "Characteristics of N-doped TiO₂ nanotube arrays by N₂-plasma for visible light-driven photocatalysis," *Journal of Alloys and Compounds*, vol. 509, no. 41, pp. 9970–9976, 2011.
- [5] D. Jiang, Y. Xu, B. Hou, D. Wu, and Y. Sun, "Synthesis of visible light-activated TiO₂ photocatalyst via surface organic modification," *Journal of Solid State Chemistry*, vol. 180, no. 5, pp. 1787–1791, 2007.
- [6] H. Park, Y. K. Kirn, and W. Choi, "Reversing CdS preparation order and its effects on photocatalytic hydrogen production of CdS/Pt-TiO₂ hybrids under visible light," *The Journal of Physical Chemistry C*, vol. 115, pp. 6141–6148, 2011.
- [7] S. In, A. Orlov, R. Berg et al., "Effective visible light-activated B-doped and B,N-codoped TiO₂ photocatalysts," *Journal of the American Chemical Society*, vol. 129, no. 45, pp. 13790–13791, 2007.
- [8] S. Bingham and W. A. Daoud, "Recent advances in making nano-sized TiO₂ visible-light active through rare-earth metal doping," *Journal of Materials Chemistry*, vol. 21, no. 7, pp. 2041–2050, 2011.
- [9] H. Gao, C. Liu, H. E. Jeong, and P. Yang, "Plasmon-enhanced photocatalytic activity of iron oxide on gold nanopillars," *ACS Nano*, vol. 6, no. 1, pp. 234–240, 2012.
- [10] Z. Liu, W. Hou, P. Pavaskar, M. Aykol, and S. B. Cronin, "Plasmon resonant enhancement of photocatalytic water splitting under visible illumination," *Nano Letters*, vol. 11, no. 3, pp. 1111–1116, 2011.
- [11] Z. Zhan, J. An, H. Zhang, R. V. Hansen, and L. Zheng, "Three-dimensional plasmonic photoanodes based on Au-embedded TiO₂ structures for enhanced visible-light water splitting," *ACS Applied Materials & Interfaces*, vol. 6, no. 2, pp. 1139–1144, 2014.
- [12] A. Primo, A. Corma, and H. Garcia, "Titania supported gold nanoparticles as photocatalyst," *Physical Chemistry Chemical Physics*, vol. 13, pp. 886–910, 2011.
- [13] K. Awazu, M. Fujimaki, C. Rockstuhl et al., "A plasmonic photocatalyst consisting of silver nanoparticles embedded in

- titanium dioxide," *Journal of the American Chemical Society*, vol. 130, no. 5, pp. 1676–1680, 2008.
- [14] D. B. Ingram and S. Linic, "Water splitting on composite plasmonic-metal/semiconductor photoelectrodes: evidence for selective plasmon-induced formation of charge carriers near the semiconductor surface," *Journal of the American Chemical Society*, vol. 133, no. 14, pp. 5202–5205, 2011.
 - [15] T. Ihara, M. Miyoshi, Y. Iriyama, O. Matsumoto, and S. Sugihara, "Visible-light-active titanium oxide photocatalyst realized by an oxygen-deficient structure and by nitrogen doping," *Applied Catalysis B: Environmental*, vol. 42, no. 4, pp. 403–409, 2003.
 - [16] X. B. Chen, L. Liu, P. Y. Yu, and S. S. Mao, "Increasing solar absorption for photocatalysis with black hydrogenated titanium dioxide nanocrystals," *Science*, vol. 331, no. 6018, pp. 746–750, 2011.
 - [17] H. Y. Chang, W. J. Tzeng, C. H. Lin, and S. Y. Cheng, "Ionic compounds lamination reaction and characteristics of photo-sensitive copper indium sulfide on titania nanotube arrays," *Journal of Alloys and Compounds*, vol. 509, no. 35, pp. 8700–8706, 2011.
 - [18] R. Leary and A. Westwood, "Carbonaceous nanomaterials for the enhancement of TiO_2 photocatalysis," *Carbon*, vol. 49, no. 3, pp. 741–772, 2011.
 - [19] B. Ahmmad, Y. Kusumoto, S. Somekawa, and M. Ikeda, "Carbon nanotubes synergistically enhance photocatalytic activity of TiO_2 ," *Catalysis Communications*, vol. 9, no. 6, pp. 1410–1413, 2008.
 - [20] Y. Ou, J. D. Lin, S. M. Fang, and D. W. Liao, "MWNT- TiO_2 :Ni composite catalyst: a new class of catalyst for photocatalytic H_2 evolution from water under visible light illumination," *Chemical Physics Letters*, vol. 429, pp. 199–203, 2006.
 - [21] K. Dai, T. Y. Peng, D. N. Ke, and B. Q. Wei, "Photocatalytic hydrogen generation using a nanocomposite of multi-walled carbon nanotubes and TiO_2 nanoparticles under visible light irradiation," *Nanotechnology*, vol. 20, no. 12, Article ID 125603, 2009.
 - [22] B. Kim and W. M. Sigmund, "Functionalized multiwall carbon nanotube/gold nanoparticle composites," *Langmuir*, vol. 20, no. 19, pp. 8239–8242, 2004.
 - [23] P. Zeng, Q. G. Zhang, X. Zhang, and T. Y. Peng, "Graphite oxide- TiO_2 nanocomposite and its efficient visible-light-driven photocatalytic hydrogen production," *Journal of Alloys and Compounds*, vol. 516, pp. 85–90, 2012.
 - [24] W. D. Wang, P. Serp, P. Kalck, and J. L. Faria, "Visible light photodegradation of phenol on MWNT- TiO_2 composite catalysts prepared by a modified sol-gel method," *Journal of Molecular Catalysis A: Chemical*, vol. 235, no. 1-2, pp. 194–199, 2005.
 - [25] X. H. Huang, Z. Y. Zhan, X. Wang et al., "Rayleigh-instability-driven simultaneous morphological and compositional transformation from Co nanowires to CoO octahedra," *Applied Physics Letters*, vol. 97, Article ID 203112, 2010.
 - [26] T. Peng, D. Zhao, K. Dai, W. Shi, and K. Hirao, "Synthesis of titanium dioxide nanoparticles with mesoporous anatase wall and high photocatalytic activity," *The Journal of Physical Chemistry B*, vol. 109, no. 11, pp. 4947–4952, 2005.
 - [27] G. M. An, W. H. Ma, Z. M. Sun et al., "Preparation of titania/carbon nanotube composites using supercritical ethanol and their photocatalytic activity for phenol degradation under visible light irradiation," *Carbon*, vol. 45, no. 9, pp. 1795–1801, 2007.
 - [28] W. H. Lee, S. J. Kim, W. J. Lee, J. G. Lee, R. C. Haddon, and P. J. Reucroft, "X-ray photoelectron spectroscopic studies of surface modified single-walled carbon nanotube material," *Applied Surface Science*, vol. 181, no. 1-2, pp. 121–127, 2001.
 - [29] V. Datsyuk, M. Kalyva, K. Papagelis et al., "Chemical oxidation of multiwalled carbon nanotubes," *Carbon*, vol. 46, no. 6, pp. 833–840, 2008.
 - [30] J. G. Yu, T. T. Ma, and S. W. Liu, "Enhanced photocatalytic activity of mesoporous TiO_2 aggregates by embedding carbon nanotubes as electron-transfer channel," *Physical Chemistry Chemical Physics*, vol. 13, pp. 3491–3501, 2011.
 - [31] Q. J. Xiang and J. G. Yu, "Graphene-based photocatalysts for hydrogen generation," *The Journal of Physical Chemistry Letters*, vol. 4, pp. 753–759, 2013.
 - [32] X. H. Huang, C. B. Tay, Z. Y. Zhan et al., "Universal photoluminescence evolution of solution-grown ZnO nanorods with annealing: important role of hydrogen donor," *CrystEngComm*, vol. 13, no. 23, pp. 7032–7036, 2011.
 - [33] X. H. Huang, Z. Y. Zhan, K. P. Pramoda, C. Zhang, L. X. Zheng, and S. J. Chua, "Correlating the enhancement of UV luminescence from solution-grown ZnO nanorods with hydrogen doping," *CrystEngComm*, vol. 14, no. 16, pp. 5163–5165, 2012.
 - [34] K. Dai, Y. Yao, H. Liu, I. Mohamed, H. Chen, and Q. Y. Huang, "Enhancing the photocatalytic activity of lead molybdate by modifying with fullerene," *Journal of Molecular Catalysis A: Chemical*, vol. 374, pp. 111–117, 2013.
 - [35] C. Liu, H. Chen, K. Dai, A. Xue, and Q. Huang, "Synthesis, characterization, and its photocatalytic activity of double-walled carbon nanotubes- TiO_2 hybrid," *Materials Research Bulletin*, vol. 48, no. 4, pp. 1499–1505, 2013.
 - [36] K. Dai, X. H. Zhang, K. Fan, T. Y. Peng, and B. Q. Wei, "Hydrothermal synthesis of single-walled carbon nanotube- TiO_2 hybrid and its photocatalytic activity," *Applied Surface Science*, vol. 270, pp. 238–244, 2013.
 - [37] D. S. Kim and S. Y. Kwak, "The hydrothermal synthesis of mesoporous TiO_2 with high crystallinity, thermal stability, large surface area, and enhanced photocatalytic activity," *Applied Catalysis A: General*, vol. 323, pp. 110–118, 2007.
 - [38] S. Bangkedphol, H. E. Keenan, C. M. Davidson, A. Sakultantimetha, W. Sirisaksoontorn, and A. Songsasen, "Enhancement of tributyltin degradation under natural light by N-doped TiO_2 photocatalyst," *Journal of Hazardous Materials*, vol. 184, no. 1-3, pp. 533–537, 2010.
 - [39] O. Akhavan, M. Abdollahad, Y. Abdi, and S. Mohajerzadeh, "Synthesis of titania/carbon nanotube heterojunction arrays for photoinactivation of *E. coli* in visible light irradiation," *Carbon*, vol. 47, no. 14, pp. 3280–3287, 2009.
 - [40] T. Puangpetch, T. Sreethawong, and S. Chavadej, "Hydrogen production over metal-loaded mesoporous-assembled SrTiO_3 nanocrystal photocatalysts: effects of metal type and loading," *International Journal of Hydrogen Energy*, vol. 35, no. 13, pp. 6531–6540, 2010.

Research Article

Functional Carbon Nanotube/Mesoporous Carbon/MnO₂ Hybrid Network for High-Performance Supercapacitors

Tao Tao, Ling Zhang, Hao Jiang, and Chunzhong Li

Key Laboratory for Ultrafine Materials of Ministry of Education, School of Materials Science and Engineering,
East China University of Science and Technology, Shanghai 200237, China

Correspondence should be addressed to Ling Zhang; zlingzi@ecust.edu.cn and Chunzhong Li; czli@ecust.edu.cn

Received 23 May 2014; Accepted 16 June 2014; Published 21 July 2014

Academic Editor: Xiaohu Huang

Copyright © 2014 Tao Tao et al. This is an open access article distributed under the Creative Commons Attribution License, which permits unrestricted use, distribution, and reproduction in any medium, provided the original work is properly cited.

A functional carbon nanotube/mesoporous carbon/MnO₂ hybrid network has been developed successfully through a facile route. The resulting composites exhibited a high specific capacitance of 351 F/g at 1 A g⁻¹, with intriguing charge/discharge rate performance and cycling stability due to a synergistic combination of large surface area and excellent electron-transport capabilities of MnO₂ with the good conductivity of the carbon nanotube/mesoporous carbon networks. Such composite shows great potential to be used as electrodes for supercapacitors.

1. Introduction

Supercapacitors have attracted significant attention over the past decades due to their great advantages such as high power supply, long cycle life, and low cost and, therefore, offer a promising approach to meet the increasing power demands for portable devices and automotive applications [1–3]. It is noteworthy that performances of supercapacitors depend strongly on the properties of the electrode materials they employ. As a type of good candidate, carbonaceous materials, transition metal oxides, and conducting polymers have always attracted great interest [4–6]. Among them, manganese dioxide (MnO₂) has been intensively studied as electrode material due to its outstanding capacitive properties and environmental benignity, in addition to being cheap and largely available [7–9]. However, the poor electronic conductivity of MnO₂ has limited its application in high-performance supercapacitors. To enhance the desired properties, the combination of MnO₂ and other conductive electrode materials is reckoned to tackle this limitation.

On other hand, carbon materials, especially carbon nanotubes (CNTs), are promising materials as electrodes for supercapacitors because of their high conductivity and short diffusion path to ions and excitons. The supercapacitors based on CNTs exhibit excellent power density as testified in recent years. However, the specific capacitance and energy density

of CNTs are always lower than other carbon materials such as activated carbon (typical in the range of 15–200 F g⁻¹ for CNTs) due to the limited surface area (typically less than 200 m² g⁻¹), which restricts the usage of CNTs as electrodes for supercapacitors [10–12]. In comparison with CNTs, mesoporous carbon (MC) usually exhibits a better specific capacitance up to 200 F g⁻¹, because of their large surface area and suitable pore size distribution [13–15]. And, in our previously work [16], we reported the fabrication of uniform CNT/MC networks via a facile organic sol-gel chemical route, which exhibited greatly increased specific capacitance due to the favorable balance between specific surface area and pore size distribution, and a 3D, well-connected through-pore structure. However, the specific capacitance of CNT/MC networks is still poor relative to transition metal oxides such as MnO₂. Therefore, it has inspired attempts to develop novel electrode materials via the coupling of CNT/MC networks and MnO₂ as electrode for supercapacitor, which may exhibit huge potentials to combine the advantages of both of them.

Herein, we report a convenient preparation of well-designed uniform CNT/MC/MnO₂ hybrid networks by growing MnO₂ along the backbone of the CNT/MC networks. The resulting CNT/MC/MnO₂ hybrid network electrode, under preferred conditions, exhibits an outstanding specific capacitance of 351 F g⁻¹ at a scan rate of 10 mV s⁻¹

and retains the high values of 195 F g^{-1} even at a high scan rate of 500 mV s^{-1} . All the evidence indicates that the rational combination of CNT/MC networks and MnO_2 will greatly improve the electrochemical performance, where MnO_2 on the surface of CNT/MC networks is essential for high energy storage and interconnected porous channels and high electrical conductivity of networks can accelerate the kinetic process of ion diffusion.

2. Experimental Section

2.1. Synthesis of CNT/MC/ MnO_2 Hybrid Network. All the reagents used in the experiments were of analytical grade and used without further purification. Prior to use, purified MWCNTs (Alpha Nano Technology Co., Ltd., China) were treated with concentrated acids ($\text{H}_2\text{SO}_4/\text{HNO}_3 = 1/1$ (v/v)) for 3 hours under 60°C , washed with copious of water, and dried at 60°C . In a typical synthesis, the acid-treated CNTs (0.05 g) were suspended in deionized water and thoroughly dispersed using ultrasound (sonic power $\sim 100 \text{ W}$) for 2 hours. Once the CNTs were dispersed, P123 ((PEO-PPO-PEO), 0.248 g, 22.4 mmol), resorcinol (0.124 g, 11.2 mmol), formaldehyde (0.176 g, 22.1 mmol), and sodium carbonate catalyst (0.6 mg, 0.056 mmol) were added to the reaction solution. The P123 was chosen as the generation of mesoporous structures. After stirring for half an hour, carbon fiber papers (CFP) were put into the solution, and the sol-gel mixture was cured at 85°C for 72 hours. The CFP act as an electron collector, and CNT/MC networks directly grow on the CFP substrate to improve the contact between them. The resulting gels were washed with *tert*-butanol for 72 h to remove water from the pores of the gel network. The gels were subsequently dried with lyophilization (freeze-drying) and pyrolyzed at 950°C under N_2 atmosphere for 3 hours, and CNT/MC networks were obtained. Then, the obtained CNT/MC network was again dispersed in deionized water, and followed by adding KMnO_4 (CNT/MC and KMnO_4 mass ratio of 1:1) the suspension was stirred at room temperature for different times (10/20/30 min, resp.), filtrated and washed using deionized water, and dried in air at room temperature. CNT/MC/ MnO_2 hybrid network was finally obtained and named as CNT/MC/ MnO_2 -10, CNT/MC/ MnO_2 -20, and CNT/MC/ MnO_2 -30, respectively.

2.2. Characterization. The morphology of samples was characterized with scanning electron microscopy (FESEM; Hitachi S-4800) operated at 5 kV. The samples were also analyzed by a powder X-ray diffraction system (XRD, D/MAX 2550 VB/PC) equipped with CuK α radiation. N_2 adsorption/desorption was determined by Brunauer-Emmett-Teller (BET) measurements using a Micromeritics ASAP 2100 surface area analyzer.

2.3. Electrochemical Measurements. All electrochemical measurements were done on an Ametek PARSTAT 2273 potentiostat in a three-electrode setup: the as-prepared products as the working electrode, a platinum foil as the counter electrode, and a saturated calomel electrode (SCE) as the reference

electrode. The electrochemical measurements included cyclic voltammograms (CVs) and galvanostatic charge/discharge (CD). All electrochemical measurements were carried out at room temperature in 1 M NaSO_4 aqueous electrolyte, under the potential range from -0.2 to 0.8 V .

3. Results and Discussion

Figure 1(a) shows the low magnification SEM image of the obtained CNT/MC networks. It can be seen that the CFP collector is covered with a layer of foam-like CNT/MC networks. We have reported that the network is comprised of random CNTs or CNTs bundles which interconnected by thin carbon sheets [5]. Figures 1(b) to 1(d) show the SEM image of the as-synthesized CNT/MC/ MnO_2 hybrid networks with different reaction time. It can be obviously seen that the MnO_2 nanoparticles assembled on the surface of the CNT/MC networks, owing to the reaction of MnO_4^- with less active carbons. And most of the nanosheets of MC in the CNT/MC networks disappeared, due to the reaction. The XRD patterns of CNT/MC networks, MnO_2 , and CNT/MC/ MnO_2 -10 sample are shown in Figure 2. It is clear that most MnO_2 is in amorphous nature, since the weak and broad peaks of MnO_2 in XRD analysis and the peaks at 2θ around 12° (0 0 1), 37° (1 1 1) and 66° (3 1 2) are indexed to poor crystallized birnessite-type MnO_2 . It has been reported that the amorphous parts are beneficial to increase the specific capacitance for the supercapacitors because the highly amorphous structure should favor the electrolyte to insert into or to expel out from the oxide matrix, which can enhance contact between the electrolyte and the electrode material and then improve the utilization ratio of the material. Comparing the samples with different reaction times, it is clear that the uniform MnO_2 coating has grown thicker with the increasing of reaction time. And for CNT/MC/ MnO_2 -30, there are too many MnO_2 nanoparticles on the CNT/MC network so that parts of the channel in the hybrid networks are blocked, which have influence on the electrochemical performance of the sample.

To examine the electrochemical performance of our present CNT/MC/ MnO_2 hybrid network materials, the samples were fabricated into the supercapacitor electrode, and cyclic voltammogram (CV) and galvanostatic charge-discharge (CD) measurements were carried out in 1 M NaSO_4 aqueous electrolyte, under the potential range from -0.2 to 0.8 V to avoid the electrolysis of water. Figure 3 shows the CV curves of CNT/MC/ MnO_2 hybrid networks at different scan rates (20, 50, 100, 200, and 1000 mV/s , resp.). CV curves of all CNT/MC/ MnO_2 hybrid networks are relatively rectangular in shape, proving the ideal pseudocapacitive nature at small scan rate. And under large scan rate (1000 mV/s), CV curves of CNT/MC/ MnO_2 -10 and sample CNT/MC/ MnO_2 -20 are still symmetrical, indicating excellent power capacitor behaviours; however, with MnO_2 loading increasing, the CV curves change into asymmetrical sharp. The low rate capability of CNT/MC/ MnO_2 -30 is caused by the poor conductivity of MnO_2 nanoparticles.

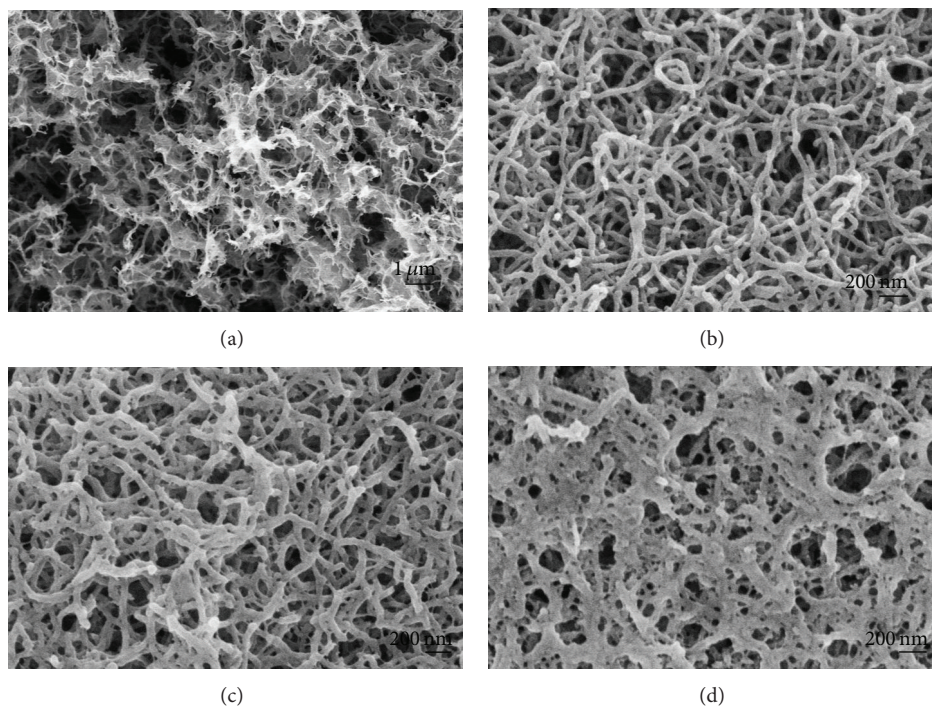


FIGURE 1: SEM images of (a) CNT/MC networks; (b) CNT/MC/MnO₂-10; (c) CNT/MC/MnO₂-20; (d) CNT/MC/MnO₂-30.

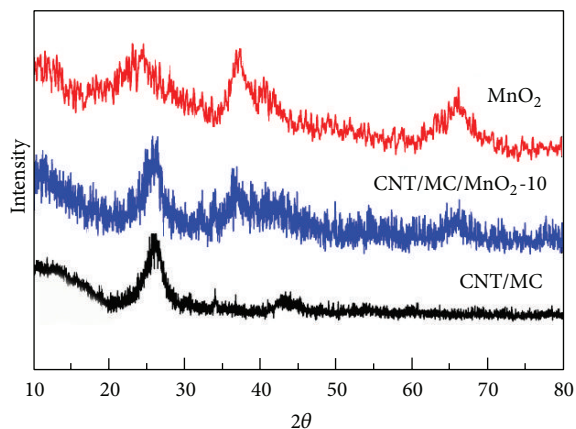


FIGURE 2: XRD patterns of CNT/MC networks, MnO₂, and CNT/MC/MnO₂-10.

Figure 4(a) shows the charge-discharge curves of all CNT/MC/MnO₂ hybrid networks and CNT/MC network at a current density of 1 A g⁻¹. The linear voltage-time profile and the highly symmetric charge-discharge characteristics also show good capacitive behavior of all samples. The discharge time for CNT/MC/MnO₂ hybrid networks is about two times larger than that of CNT/MC network, exhibiting an enhanced capacitance performance with the addition of MnO₂. The galvanostatic charge-discharge measurement is assumed to be the most accurate technique to estimate the supercapacitive performance. The specific capacitances C in this paper are calculated from galvanostatic charge-discharge curves according to $I t / m \Delta E$, where I is the

charge-discharge current, t is the discharge time, and ΔE is the voltage difference. The specific capacitance of CNT/MC network is only 159 F g⁻¹ at a current density of 1 A g⁻¹, while, for CNT/MC/MnO₂-10, its specific capacitance is 316 F g⁻¹. And CNT/MC/MnO₂-20 exhibits larger specific capacitance (351 F g⁻¹) compared to CNT/MC/MnO₂-10, due to the increasing loading of MnO₂. However, it is interesting to note that the specific capacitance of CNT/MC/MnO₂-30 is 339 F g⁻¹, which is smaller than CNT/MC/MnO₂-20. The enhanced specific capacitance of the CNT/MC/MnO₂-20 networks is mainly attributed to the effective utilization of active materials. CNT/MC/MnO₂-20 exhibits favorable balance between MnO₂ loading amount and unique interconnected network structures. The interconnected networks create hierarchical porous channels, which enable effective electrolyte transport and active site accessibility. And the poor conductivity of MnO₂ in the CNT/MC/MnO₂-30 sample decreased its electrochemical performance, due to the overloading of MnO₂ nanoparticles.

Figure 4(b) shows the relationships between specific capacitance and charge/discharge current density. CNT/MC/MnO₂-10 shows the best rate performance and the specific capacitance is still 183 F g⁻¹ (about 58% retention) at a current density of 20 A g⁻¹; as compared, CNT/MC/MnO₂-30 retained about 50% (171 F g⁻¹), while the specific capacitance of CNT/MC/MnO₂-20 is still 195 F g⁻¹ (about 55.6% retention). The superior power capability performance of CNT/MC/MnO₂ hybrid networks indicated that the high conductivity of CNTs skeleton provides quick electron transport channel, and, more importantly, the unique 3D-network configuration with short transportation pathway

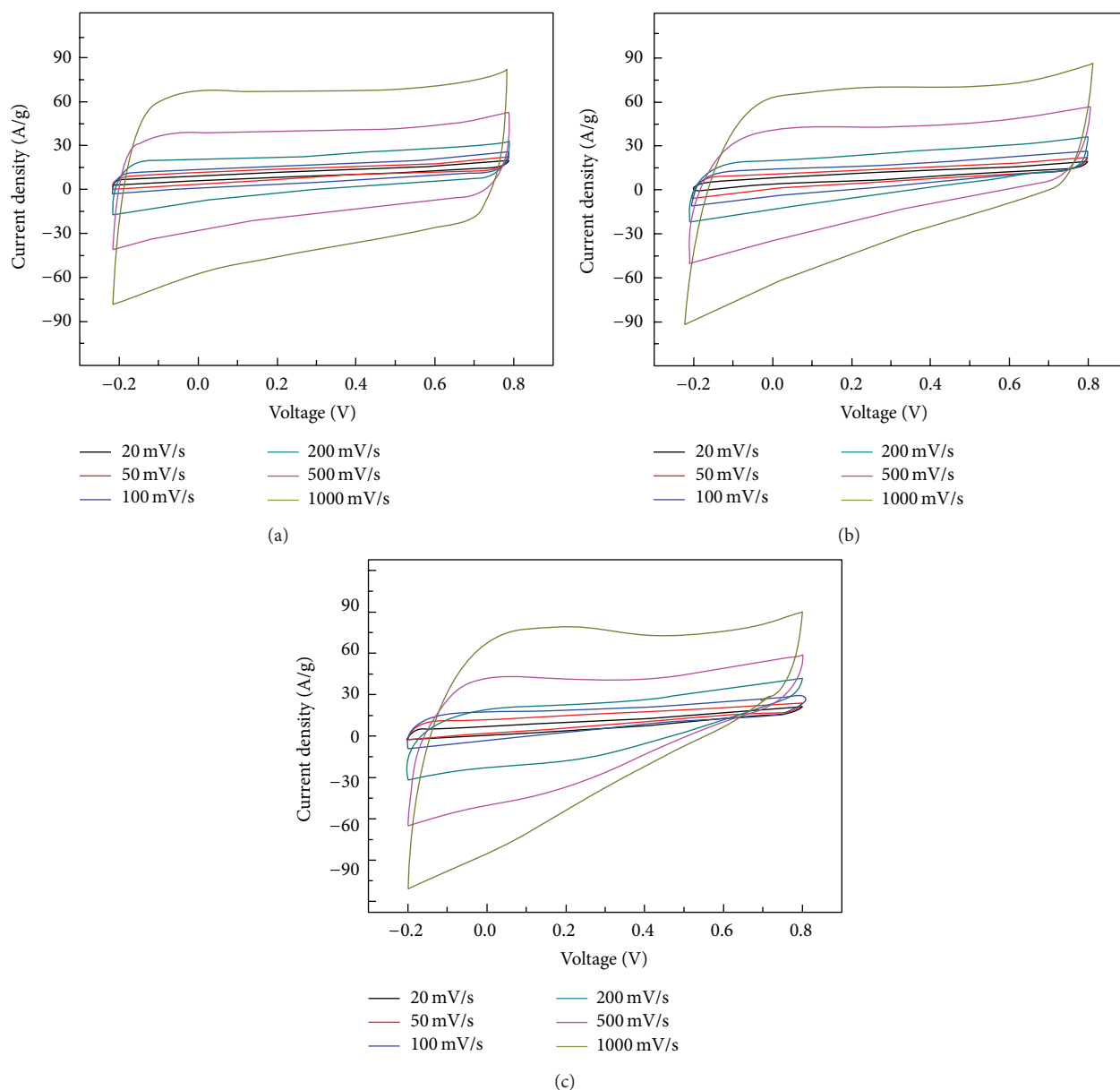


FIGURE 3: CV curves of CNT/MC/MnO₂ hybrid networks at different scan rates: (a) CNT/MC/MnO₂-10; (b) CNT/MC/MnO₂-20; (c) CNT/MC/MnO₂-30.

allows for easy accessibility of ions to the electrode/electrolyte interface and charging the capacitors. The energy density of CNT/MC/MnO₂-20 can be estimated to be 25.5 Wh kg^{-1} at a power density of 1.1 kW kg^{-1} (Figure 4(c)) which is much higher than not only the CNT/MC electrode (15.6 Wh kg^{-1}) [6], but also most of carbonaceous and MnO₂-based electrodes, such as CNTs ($<10 \text{ Wh kg}^{-1}$), graphene (3.15 Wh kg^{-1}), and MnO₂ nanoparticles ($<20 \text{ Wh kg}^{-1}$) [17–19]. More significantly, the energy density is still as high as 16.3 Wh kg^{-1} for CNT/MC/MnO₂-20 even at a high power density of 17 kW kg^{-1} . The long-term cycle stability of the CNT/MC/MnO₂-20 was also investigated. Figure 4(d) demonstrates the specific capacitance as a function of cycle number at a current density of 5 A g^{-1} , in galvanostatic charge-discharge measurements for up to 1000 cycles.

After the cycling test, there are about 86% of its initial capacities that are maintained, due to the loss of adhesion of MnO₂ with the current collector or the dissolution of MnO₂ nanoparticles into the solution [20]. This cycling performance is also superior to most of other MnO₂ nanoparticles based supercapacitors. The present results have shown that the as-designed CNT/MC/MnO₂ hybrid network exhibits an excellent electrochemical performance, even for high-rate charge/discharge operations.

Based on the above discussions, the specific capacitance of CNT/MC/MnO₂ hybrid network is not only better than the reported carbonaceous electrodes, such as CNTs (180 F g^{-1}), graphene nanosheets (175 F g^{-1}) [21, 22], and CNT/MC networks (210 F g^{-1}), but also superior to most of other carbon/MnO₂ composites, such as MnO₂/carbon aerogel

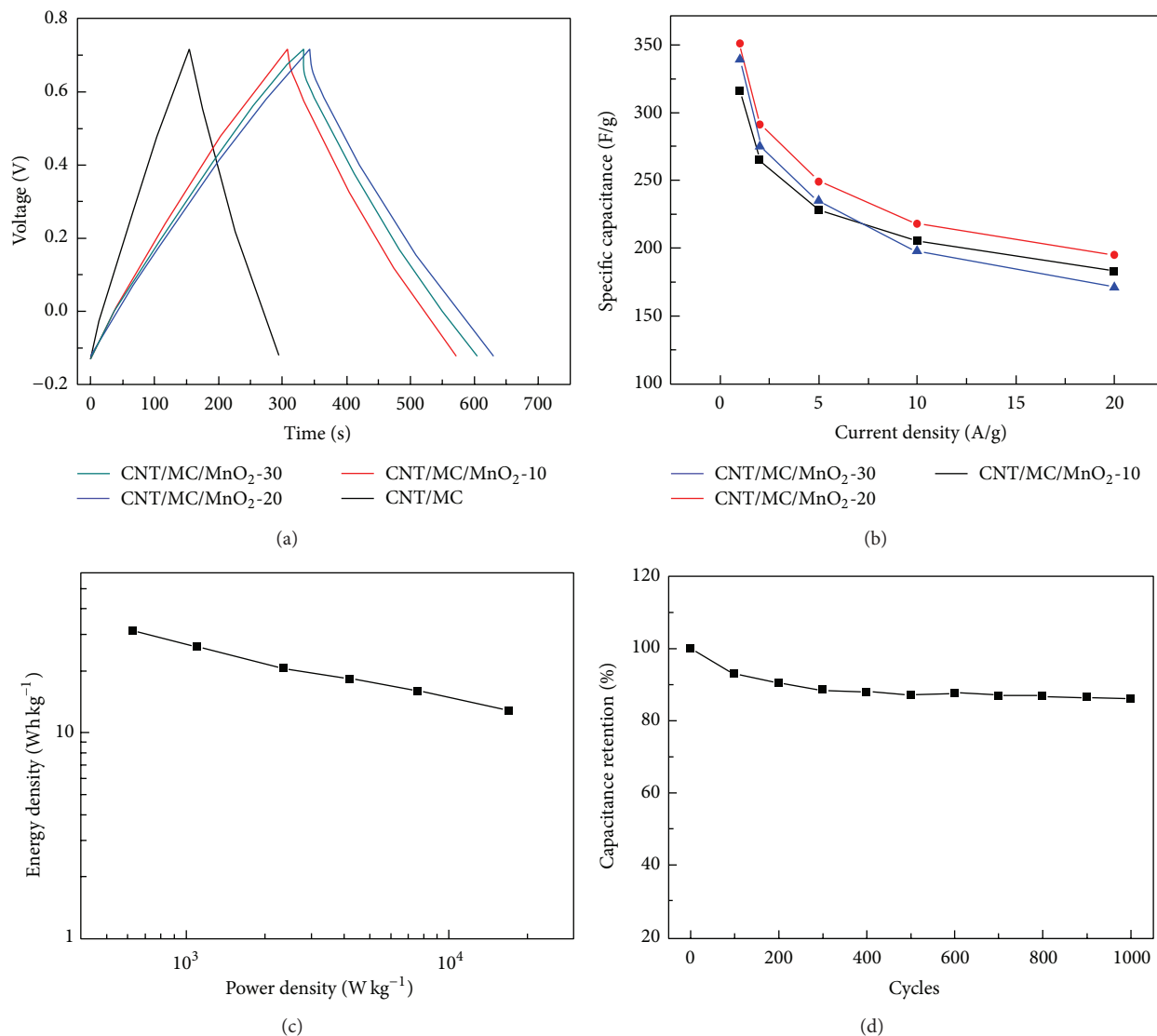


FIGURE 4: (a) charge-discharge curves of CNT/MC and CNT/MC/MnO₂ hybrid networks at 1 A g⁻¹; (b) relationship of the specific capacitance with charge/discharge current density of CNT/MC/MnO₂ hybrid networks; (c) Ragone plots of CNT/MC/MnO₂-20; (d) variation of specific capacitance with cycle number at a current density of 1 A g⁻¹ of CNT/MC/MnO₂-20.

(219 F g⁻¹) and graphene/MnO₂ (310 F g⁻¹) [23, 24]. Pure MnO₂ always exhibits high specific capacitance; however, the poor conductivity of MnO₂ results in low rate capability for high power performance. Xu et al. reported the synthesis of mesoporous MnO₂ nanowire array, which exhibited a specific capacitance as high as 493 F g⁻¹ [25]. However, at a high current density of 12 A g⁻¹, only 84 F g⁻¹ was observed. The sustainable specific capacitance of our materials is mainly due to its ability to have short paths ion diffusion with the CNT/MC networks and effective utilization of active material due to its uniform structures.

4. Conclusions

In summary, functional carbon nanotube/mesoporous carbon/manganese dioxide (CNT/MC/MnO₂) hybrid networks have been designed and fabricated via a facile route for

electrochemical energy storage. The obtained structures combined the advantages of large surface area and excellent electron-transport capabilities of MnO₂ with the good conductivity of carbon nanotube/mesoporous carbon networks and short transportation pathway of unique 3D-network configuration. The CNT/MC/MnO₂ hybrid networks exhibit greatly increased specific capacitance (351 F g⁻¹ at 1 A g⁻¹) compared with CNT/MC networks as supercapacitor electrode in 1 M NaSO₄ aqueous electrolyte. The energy density of CNT/MC/MnO₂-20 can be estimated to be 25.5 Wh kg⁻¹ at a power density of 1.1 kW kg⁻¹, and the energy density is still as high as 16.3 Wh kg⁻¹ even at a high power density of 17 kW kg⁻¹, indicating excellent electrochemical performance. It is reckoned that the present work also sheds light on the design of carbon and transition metal oxides 3D-networks for other applications.

Conflict of Interests

The authors declare that there is no conflict of interests regarding the publication of this paper.

Acknowledgments

This work was supported by the National Natural Science Foundation of China (51173043, 21136006, 21236003, and 21322607), the Special Projects for Nanotechnology of Shanghai (12nm0502700), the Basic Research Program of Shanghai (13JC1408100, 13NM1400801), the Program for New Century Excellent Talents in University (NCET-11-0641), and the Fundamental Research Funds for the Central Universities.

References

- [1] M. Winter and R. J. Brodd, "What are batteries, fuel cells, and supercapacitors?" *Chemical Reviews*, vol. 104, no. 10, pp. 4245–4270, 2004.
- [2] J. R. Miller and P. Simon, "Materials science: electrochemical capacitors for energy management," *Science*, vol. 321, no. 5889, pp. 651–652, 2008.
- [3] S. J. Guo and S. J. Dong, "Graphene nanosheet: synthesis, molecular engineering, thin film, hybrids, and energy and analytical applications," *Chemical Society Reviews*, vol. 40, p. 2644, 2011.
- [4] L. Dai, D. W. Chang, J. Baek, and W. Lu, "Carbon nanomaterials for advanced energy conversion and storage," *Small*, vol. 8, no. 8, pp. 1130–1166, 2012.
- [5] A. S. Aricò, P. Bruce, B. Scrosati, J.-M. Tarascon, and W. van Schalkwijk, "Nanostructured materials for advanced energy conversion and storage devices," *Nature Materials*, vol. 4, pp. 366–377, 2005.
- [6] D. R. Rolison, J. W. Long, J. C. Lytle et al., "Multifunctional 3D nanoarchitectures for energy storage and conversion," *Chemical Society Reviews*, vol. 38, no. 1, pp. 226–252, 2009.
- [7] D. Wang, F. Li, and H. Cheng, "Hierarchical porous nickel oxide and carbon as electrode materials for asymmetric supercapacitor," *Journal of Power Sources*, vol. 185, no. 2, pp. 1563–1568, 2008.
- [8] H. Jiang, T. Zhao, C. Yan, J. Ma, and C. Li, "Hydrothermal synthesis of novel Mn_3O_4 nano-octahedrons with enhanced supercapacitors performances," *Nanoscale*, vol. 2, no. 10, pp. 2195–2198, 2010.
- [9] R. Liu and S. B. Lee, " MnO_2 /poly(3,4-ethylenedioxythiophene) coaxial nanowires by one-step coelectrodeposition for electrochemical energy storage," *Journal of the American Chemical Society*, vol. 130, no. 10, pp. 2942–2943, 2008.
- [10] R. H. Baughman, A. A. Zakhidov, and W. A. de Heer, "Carbon nanotubes: the route toward applications," *Science*, vol. 297, no. 5582, pp. 787–792, 2002.
- [11] W. Lu, L. Qu, K. Henry, and L. Dai, "High performance electrochemical capacitors from aligned carbon nanotube electrodes and ionic liquid electrolytes," *Journal of Power Sources*, vol. 189, no. 2, pp. 1270–1277, 2009.
- [12] E. Frackowiak, K. Metenier, V. Bertagna, and F. Beguin, "Supercapacitor electrodes from multiwalled carbon nanotubes," *Applied Physics Letters*, vol. 77, no. 15, pp. 2421–2423, 2000.
- [13] L. L. Zhang and X. S. Zhao, "Carbon-based materials as supercapacitor electrodes," *Chemical Society Reviews*, vol. 38, pp. 2520–2531, 2009.
- [14] W. R. Li, D. H. Chen, Z. Li et al., "Nitrogen enriched mesoporous carbon spheres obtained by a facile method and its application for electrochemical capacitor," *Electrochemistry Communications*, vol. 9, no. 4, pp. 569–573, 2007.
- [15] Y. Zhai, Y. Dou, D. Zhao, P. F. Fulvio, R. T. Mayes, and S. Dai, "Carbon materials for chemical capacitive energy storage," *Advanced Materials*, vol. 23, no. 42, pp. 4828–4850, 2011.
- [16] T. Tao, L. Zhang, H. Jiang, and C. Li, "Functional mesoporous carbon-coated CNT network for high-performance supercapacitors," *New Journal of Chemistry*, vol. 37, no. 5, pp. 1294–1297, 2013.
- [17] L. Deng, G. Zhu, J. Wang et al., "Graphene- MnO_2 and graphene asymmetrical electrochemical capacitor with a high energy density in aqueous electrolyte," *Journal of Power Sources*, vol. 196, no. 24, pp. 10782–10787, 2011.
- [18] M. Kaempgen, C. K. Chan, J. Ma, Y. Cui, and G. Gruner, "Printable thin film supercapacitors using single-walled carbon nanotubes," *Nano Letters*, vol. 9, no. 5, pp. 1872–1876, 2009.
- [19] X. Du, C. Wang, M. Chen, Y. Jiao, and J. Wang, "Electrochemical performances of nanoparticle Fe_3O_4 /activated carbon supercapacitor using KOH electrolyte solution," *The Journal of Physical Chemistry C*, vol. 113, no. 6, pp. 2643–2646, 2009.
- [20] L. Deng, Z. Hao, J. Wang et al., "Preparation and capacitance of graphene/multiwall carbon nanotubes/ MnO_2 hybrid material for high-performance asymmetrical electrochemical capacitor," *Electrochimica Acta*, vol. 89, pp. 191–198, 2013.
- [21] D. N. Futaba, K. Hata, T. Yamada et al., "Shape-engineerable and highly densely packed single-walled carbon nanotubes and their application as super-capacitor electrodes," *Nature Materials*, vol. 5, no. 12, pp. 987–994, 2006.
- [22] J. Yan, T. Wei, B. Shao et al., "Electrochemical properties of graphene nanosheet/carbon black composites as electrodes for supercapacitors," *Carbon*, vol. 48, no. 6, pp. 1731–1737, 2010.
- [23] G. Lv, D. Wu, and R. Fu, "Preparation and electrochemical characterizations of MnO_2 -dispersed carbon aerogel as supercapacitor electrode material," *Journal of Non-Crystalline Solids*, vol. 355, pp. 2461–2465, 2009.
- [24] L. Deng, Z. Hao, J. Wang et al., "Preparation and capacitance of graphene/multiwall carbon nanotubes/ MnO_2 hybrid material for high-performance asymmetrical electrochemical capacitor," *Electrochimica Acta*, vol. 89, pp. 191–198, 2013.
- [25] C. L. Xu, Y. Q. Zhao, G. W. Yang, F. S. Li, and H. L. Li, "Mesoporous nanowire array architecture of manganese dioxide for electrochemical capacitor applications," *Chemical Communications*, no. 48, pp. 7575–7577, 2009.

Research Article

Structural and Electrical Properties of the YSZ/STO/YSZ Heterostructure

Yue Fan, Wende Liu, Zhenfeng Kang, Tiezhu Ding, Qingrui Bo, Lingling Xiao, Xiaobing Bai, Pingping Zheng, and Qiang Li

Inner Mongolia Key Laboratory of Semiconductor Photovoltaic Technology, Inner Mongolia University, Hohhot 010021, China

Correspondence should be addressed to Tiezhu Ding; pytzding@imu.edu.cn

Received 22 April 2014; Revised 8 June 2014; Accepted 9 June 2014; Published 23 June 2014

Academic Editor: Xiaohu Huang

Copyright © 2014 Yue Fan et al. This is an open access article distributed under the Creative Commons Attribution License, which permits unrestricted use, distribution, and reproduction in any medium, provided the original work is properly cited.

The heterostructure thin films of yttria-stabilized zirconia (YSZ)/strontium titanate (STO)/YSZ with various thicknesses were deposited on MgO single crystal substrate by pulsed laser deposition (PLD) method. The structural and electrical properties of the YSZ/STO/YSZ heterostructure were studied through X-ray diffraction (XRD) and electrical conductivity measurements. The in-plane conductivities of the thin films were measured and compared with that of the bulk sample. The highest conductivities were reported for those samples with the thinnest YSZ (220) layers. The observed enhancement in the lateral ionic conductivity was probably caused by the combination of the misfit dislocation density and elastic strain in the interfaces. The enhanced ionic mobility was discussed in terms of the disorder introduced in the oxygen sublattice through the epitaxial strain at the interfaces.

1. Introduction

The search for new strategies to enhance the oxide ionic conductivity of oxide materials is very active field of research. The portable application of microsolid state fuel cells (m-SOFCs) requires a reduction in the operation temperatures, where the ionic conductivity of the electrolytes, as crucial parts of the solid oxide fuel cells (SOFCs), should be improved at lower temperatures [1]. Yttria-stabilized zirconia (YSZ) is a well-known oxygen ion conductor, where oxygen vacancies are introduced through the aliovalent substitution of zirconium (Zr) by yttrium (Y). The substitution of Zr by Y^{3+} in a 4^+ oxidation state produces an oxygen vacancy for every two Y atoms. The Y substitution stabilizes a cubic fluorite structure, where oxygen occupies the tetrahedral sites of the cubic unit cell. Technologically, YSZ is a very relevant material as an electrolyte in SOFCs. However, it is limited to high temperature applications ($>800^{\circ}\text{C}$), where an acceptable performance can be realized. Much interest has been given in acquiring this material as dense thin films to reduce the ohmic resistance of devices and consequently allow lower operating temperatures. The coherent growth of strained

interfaces in heterostructures, combined with materials with different degrees of lattice mismatch, has been proposed to possibly promote ion diffusivity [2]. Thus, these heterostructures may have an important role in the optimization of materials for energy generation and storage. This coherent growth of strained heterostructure interfaces is a characteristic of YSZ/strontium titanate (STO) heterostructure, where different structures (fluorite versus perovskite) are combined with a large lattice mismatch of 7% [3]. The interface between the highly dissimilar structures stabilizes a disordered oxygen sublattice with an increased number of oxygen vacancies, which promotes oxygen diffusion. Decreasing the size of the system to the nanometer length scale leads to a dominant influence of the interfaces on the overall ionic conductivity of the system. Novel phases can be stabilized with enhanced carrier densities and, eventually, mobility. The nanosize effects in conventional ionic conductors are widely accepted in providing novel routes for achieving higher ionic conductivities [4, 5]. These nanosize effects will be the main focus of this paper, where the ionic conductivity of the YSZ/STO/YSZ electrolyte film enhancement will be described.

2. Experimental Procedures

The pulsed laser deposition (PLD) method has become an increasingly important technique for depositing thin films of various materials. The main advantage of PLD method is its ability to deposit almost any material, while preserving the stoichiometry of multicomponent materials [6]. Furthermore, the PLD technique can operate at a low processing temperature (below 800°C) without high postannealing temperature. This experiment utilized PLD fabricated epitaxial heterostructure films, with blocks made of alternate layers of 8YSZ (8 mol%) and SrTiO₃ (99.999% purity). The laser beam was focused on a high vacuum chamber onto a computer controlled multitarget rotating system. Among the different film deposition techniques, the PLD method is particularly promising because of the ability of this method to reproduce specific target compositions of the film. The films were deposited on MgO substrates through PLD using a KrF excimer laser ($\lambda = 248$ nm) at a frequency of 5 Hz and an energy density of 5 J/cm². During the deposition, each target rotated around the perpendicular axis to the surface. The laser beam was focused on the target rotated at 10 rpm and on the dense targets in a 5 Pa atmosphere of pure O₂. The substrates were positioned parallel to and 5 cm away from the target. This distance allows sufficient interaction between the plasma plume and the background oxygen gas. The substrate temperature was maintained at 700°C during the deposition. To enhance the sticking coefficient and improve the density and crystalline degree of the film, the samples were annealed in oxygen gas at 800°C for 1 h after deposition. By controlling the sputtering time, the YSZ/STO/YSZ trilayers, with different nominal thicknesses of the YSZ interlayer, were deposited through the PLD method on the MgO single crystal substrates.

The YSZ/STO/YSZ trilayers were obtained with various thicknesses of the individual YSZ layers ranging from 62 nm to 203 nm, whereas the thicknesses of the STO were kept at 62 nm. The physical thicknesses were evaluated using a growth rate of 1 Å/s.

The microstructures, crystallinity, and growth orientation of the YSZ/STO/YSZ thin films were investigated by X-ray diffraction (XRD) using Cu-K α radiation. To analyze the conductance of the films, the in-plane AC impedance was measured between two Ag parallel contacts deposited on the film surface [7]; the measurement was performed at temperatures ranging from 350°C to 600°C in air with a frequency range from 40 Hz to 10 MHz.

3. Results and Discussion

3.1. Microstructure of YSZ/STO/YSZ Epitaxial Heterostructure Films. Figure 1 illustrates the XRD features of the films with various YSZ thicknesses, along with the strong MgO (110) peaks of the substrate. The XRD analyses clearly indicated that these films are composed of individual layers of STO and YSZ.

The XRD pattern exhibited a well-cubic fluorite structure, and the sharp lines of the XRD peaks can be observed, indicating that the heterostructure thin films were formed

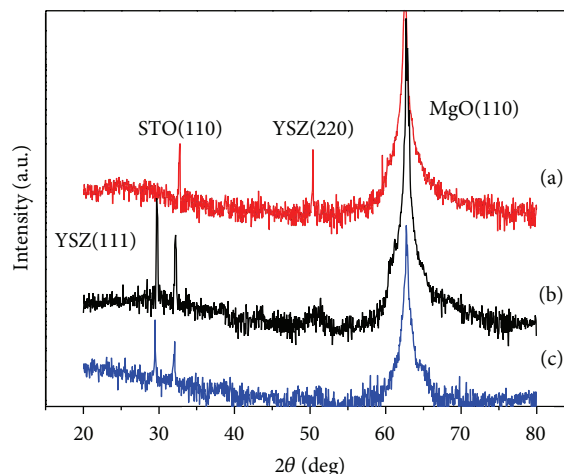


FIGURE 1: XRD patterns of YSZ/STO/YSZ heterostructure electrolyte thin films with different thicknesses, where the thickness of the STO remains at 62 nm, whereas those of the thickness of YSZ are (a) 62 nm, (b) 117 nm, and (c) 203 nm.

after sintering at 800°C for 1 h. Figure 1 shows that the (110) diffraction peaks from the MgO substrate and STO buffer layer were aligned with the reference data, and the intensities of the YSZ/STO/YSZ films also increased when the film thickness ranged from 62 nm to 203 nm. The preferred orientation of the YSZ film changed from (111) to (220) when the thickness of the YSZ decreased from 203 nm to 62 nm (for the constant STO thickness). This change in orientation indicated that the YSZ layers experienced larger lattice strain across the layer to adapt an in-plane orientation with the STO layers and the YSZ was fully strained to the lattice parameters of the STO [4]. This growth mode results in comparatively low interfacial and surface energies of (220) oriented grains and expanded lattice spacing of the layers.

From the surface view, the YSZ/STO/YSZ film appeared to be quite dense and homogeneous without any delamination at the interfaces, and the film adhered well to the MgO substrate. No cracks or pores are present on the layer after the annealing, which is probably a result of the residual stresses in the annealed thin film. Based on the cross-sectional SEM images, the thickness of each of the STO layers was about 62 nm.

3.2. Electrical Characterization. Electrochemical impedance spectroscopy (EIS) analysis allows separation of the impedance contribution of the electrolyte (at high frequencies) from that of the electrode (at low frequencies). EIS measurements can be performed using a two-electrode configuration that does not require a reference electrode, which would be difficult to place in a thin-film sample [8]. Electrical conductivity measurements for the YSZ/STO/YSZ samples were performed between 350°C and 600°C at 50°C steps. High-resistance substrates need to be used for the electrical measurements of the in-plane conductivity of the thin film. The measured conductance of the MgO substrate was about three orders lower than that of the YSZ/STO/YSZ film. Hence,

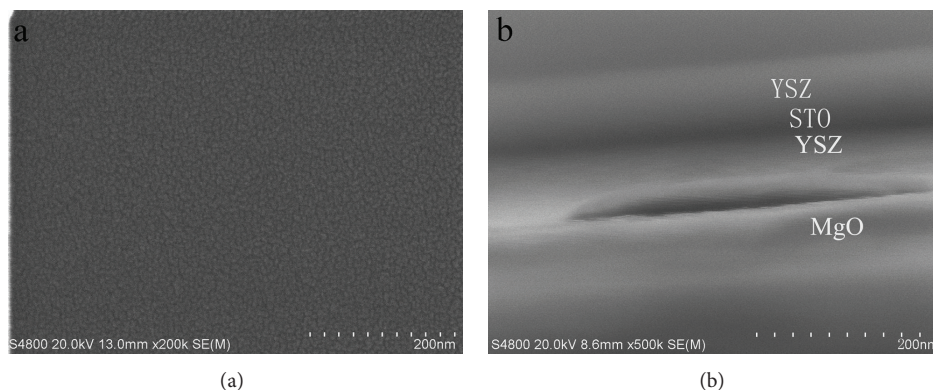


FIGURE 2: (a) Surface SEM images of the YSZ/STO/YSZ (YSZ = 62 nm) film on MgO (110) substrate after sintering at 800°C for 1 h. (b) Cross-sectional SEM images of the YSZ/STO/YSZ film.

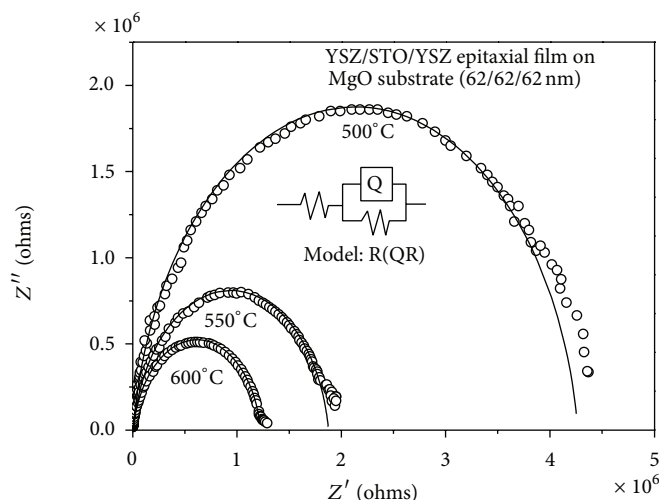


FIGURE 3: Impedance spectra (open symbols) and corresponding fit curves (lines) measured at 500°C, 550°C, and 600°C for the YSZ/STO/YSZ epitaxial films on MgO substrates in dry air; the inset shows an equivalent circuit.

the substrate resistance was negligible compared with that of the YSZ/STO/YSZ film because of the small geometrical factor.

Figure 3 displays the typical Nyquist plots for the annealed YSZ/STO/YSZ samples at various temperatures under open air and with the corresponding temperature dependent on the total ohmic resistance. Together with the fit curves of the presented equivalent circuit, the patterns consist of only one semicircle attributed to the response of the samples, which are slightly asymmetric in the low frequency range. An equivalent (RQ) R circuit (inset) was used in the fitting procedure to obtain the resistances R, with Q representing the constant phase element.

The ionic conductivities of the films were analyzed by AC impedance method. Figure 4 illustrates the Arrhenius plots of the electrical conductivities measured in dry air, with a temperature range from 350°C to 600°C, for the YSZ/STO/YSZ heterostructures with different thicknesses. The electrical conduction of the bulk YSZ is also shown in Figure 4

for comparison. The bulk YSZ sample shows the well-known Arrhenius behavior with activation energy of 1.24 eV. All YSZ/STO/YSZ heterostructures exhibited higher conductivities and smaller activation energies than the bulk YSZ sample. Figure 4 reveals that the reduction in layer thickness causes a decreased active energy; this figure also shows an enhancement in the exhibited ionic conductivity by roughly 3.3 orders of magnitude for the YSZ/STO/YSZ (YSZ = 62 nm) trilayer films deposited on the MgO compared with the conductivity values of the bulk YSZ. The ionic conductivity of the YSZ/STO/YSZ (YSZ = 62 nm) film was 0.5 S/cm at 600°C, with a conduction activation energy of 0.95 eV. The biggest relative conductivity enhancement was found in the lower temperature region. The fact that our structures showed different relative orientations (Figure 2) indicates that the conductivity enhancement may be associated with a particular crystallographic arrangement at the interface.

Two regimes of the conductivity curves were identified with a transition occurring at a temperature of 500°C. These

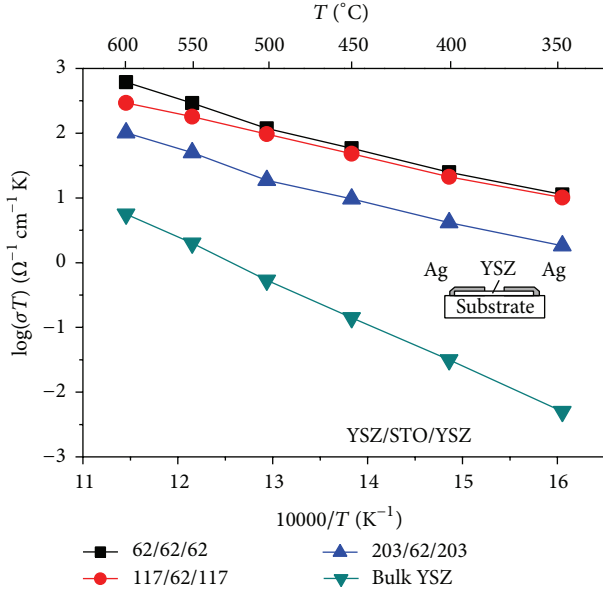


FIGURE 4: Arrhenius plots of the electrical conductivities for the epitaxial YSZ/STO/YSZ thin films with different thicknesses in the temperature range from 350°C to 600°C. The inset shows the electrode configuration for the lateral conductivity measurements.

TABLE 1: Activation energy for the ionic transport measured on different YSZ/STO/YSZ multilayer systems, as shown in Figure 4.

d/nm Thickness of the YSZ layer	d/nm Thickness of the STO layer	E_a/eV ($<500^\circ\text{C}$)	E_a/eV ($>500^\circ\text{C}$)
62	62	0.64	0.95
117	62	0.71	0.98
203	62	0.76	1.12

regimes have very distinct activation energies for oxygen ion migration, which have been found by fitting the linear segments to an Arrhenius expression. These activation energies are shown in Table 1. These observations indicate a superposition of two parallel contributions: one is caused by the bulk lattice, and the other one is attributed to the tensile strain effects [2, 9]. At lower measuring temperatures ($<500^\circ\text{C}$), the tensile strain contribution dominates the ionic conductivity. Moreover, this tensile strain contribution increases as the individual layer thickness decreases (as seen in Figure 2), which explains the increase in lateral ionic conductivity as the YSZ layer thickness decreased [10]. At higher temperatures, O^{2-} ions gain enough thermal energy to overcome the energy barrier (1.24 eV) for ionic conduction through the vacancies in the lattice; hence, a more “bulk-like” conductivity is obtained. Although the conductivity is dominated by bulk lattice diffusion at higher measuring temperatures, a tensile strain contribution is still present [9].

There is much debate surrounding the emergence of colossal ionic conductivity in highly strained films of YSZ/STO heterostructures. Guo, in a comment [11] on the original report [5], concluded that the measured conductivity of

the $\text{ZrO}_2\text{:Y}_2\text{O}_3/\text{SrTiO}_3$ heterostructure is due to electron holes in SrTiO_3 and not oxygen vacancies in YSZ. Cavallaro et al. [12] grew STO/YSZ/STO heterostructures themselves and attributed the enhanced conductivity to an interfacial alloyed oxide resulting from zirconium/strontium intermixing. From the considerations above, we also believe that strain and interfacial effects related to the density of misfit dislocations are at the origin of the enhanced conductivities reported in the present paper.

As discussed earlier, the coherent interfaces formed between the alternating STO and YSZ layers, creating a few dislocations comparable with “single crystals.” The contribution of the grain boundary conduction can be disregarded in agreement with the semicircle in Figure 3. By tailoring the thickness of the alternating layers and the lattice mismatch, the interface structure can be manipulated to have very few dislocations; the strain component is confined to the YSZ layers, which significantly improves the ionic conductivity. The strained multilayer film (YSZ = 62 nm) displays a greatly enhanced ionic conductivity, with 3.3 orders of magnitude increase, compared with the bulk YSZ at 600°C

4. Summary

This study investigated the structural and electrical properties of the YSZ/STO/YSZ heterostructure and found that preferential growth changes occur from the YSZ (111) to the YSZ (220) when the thickness of the individual layers is further decreased. These changes force YSZ into the lattice parameters of the STO. The strain that is highly confined in the YSZ layers greatly increased the ionic conductivity of the multilayered heterostructure. Atomic reconstruction at the interface was proposed among highly dissimilar structures (such as fluorite and perovskite) to provide both large numbers of carriers and high-mobility plane, yielding to immense values of the ionic conductivity. Thus, the enhanced ion conductance more likely results from the extended defects and lattice strain near the layer interfaces, which may increase the density of the O vacancies. Defects and strain relaxation may also increase the mobility of the vacancies.

Either new materials with optimized conductivity values have to be sought or new device concepts have to be developed. The interface effects in the epitaxial ionic conducting heterostructures are definitely promising pathways toward novel artificial electrolytes for cooler fuel cells or other electrochemical devices [2, 9]. However, combined experimental and theoretical efforts will be necessary to understand the ultimate origin of the enhanced conditions of the conductivity interface.

Conflict of Interests

The authors declare that there is no conflict of interests regarding the publication of this paper.

Acknowledgment

This work was supported by Natural Science Foundation of China (Approval no. 11264025).

References

- [1] E. D. Wachsman and K. T. Lee, “Lowering the temperature of solid oxide fuel cells,” *Science*, vol. 334, no. 6058, pp. 935–939, 2011.
- [2] A. Rivera-Calzada, M. R. Diaz-Guillen, O. J. Dura et al., “Tailoring interface structure in highly strained YSZ/STO heterostructures,” *Advanced Materials*, vol. 23, no. 44, pp. 5268–5274, 2011.
- [3] R. A. de Souza and A. H. H. Ramadan, “Ionic conduction in the SrTiO_3 —YSZ— SrTiO_3 heterostructure,” *Physical Chemistry Chemical Physics*, vol. 15, no. 13, pp. 4505–4509, 2013.
- [4] J. Garcia-Barriocanal, A. Rivera-Calzada, M. Varela et al., “Tailoring disorder and dimensionality: strategies for improved solid oxide fuel cell electrolytes,” *ChemPhysChem*, vol. 10, no. 7, pp. 1003–1011, 2009.
- [5] J. Garcia-Barriocanal, A. Rivera-Calzada, M. Varela et al., “Colossal ionic conductivity at interfaces of epitaxial ZrO_2 : Y_2O_3 / SrTiO_3 heterostructures,” *Science*, vol. 321, no. 5889, pp. 676–680, 2008.
- [6] A. Tebano, G. Balestrino, N. G. Boggio, C. Aruta, B. Davidson, and P. G. Medaglia, “High-quality in situ manganite thin films by pulsed laser deposition at low background pressures,” *European Physical Journal B*, vol. 51, no. 3, pp. 337–340, 2006.
- [7] O. H. Kwon and G. M. Choi, “Electrical conductivity of thick film YSZ,” *Solid State Ionics*, vol. 177, no. 35–36, pp. 3057–3062, 2006.
- [8] G. Hsieh, S. J. Ford, T. O. Mason, and L. R. Pederson, “Experimental limitations in impedance spectroscopy—part I. Simulation of reference electrode artifacts in three-point measurements,” *Solid State Ionics*, vol. 91, no. 3–4, pp. 191–201, 1996.
- [9] M. Sillassen, P. Eklund, N. Pryds, E. Johnson, U. Helmersson, and J. Böttiger, “Low-temperature superionic conductivity in strained yttria-stabilized zirconia,” *Advanced Functional Materials*, vol. 20, no. 13, pp. 2071–2076, 2010.
- [10] I. Kosacki, C. M. Rouleau, P. F. Becher, J. Bentley, and D. H. Lowndes, “Nanoscale effects on the ionic conductivity in highly textured YSZ thin films,” *Solid State Ionics*, vol. 176, no. 13–14, pp. 1319–1326, 2005.
- [11] X. Guo, “Comment on “colossal ionic conductivity at interfaces of epitaxial ZrO_2 : Y_2O_3 / SrTiO_3 heterostructures”,” *Science*, vol. 324, no. 5926, p. 465, 2009.
- [12] A. Cavallaro, M. Burriel, J. Roqueta et al., “Electronic nature of the enhanced conductivity in YSZ-STO multilayers deposited by PLD,” *Solid State Ionics*, vol. 181, no. 13–14, pp. 592–601, 2010.

Research Article

Tungsten Oxide and Polyaniline Composite Fabricated by Surfactant-Templated Electrodeposition and Its Use in Supercapacitors

Benxue Zou,¹ Shengchen Gong,¹ Yan Wang,¹ and Xiaoxia Liu²

¹ Department of Chemical Engineering, Liaodong University, Dandong 118003, China

² Department of Chemistry, Northeastern University, Shenyang, China

Correspondence should be addressed to Benxue Zou; benxue_dd@163.com

Received 20 March 2014; Accepted 11 May 2014; Published 29 May 2014

Academic Editor: Yongfeng Li

Copyright © 2014 Benxue Zou et al. This is an open access article distributed under the Creative Commons Attribution License, which permits unrestricted use, distribution, and reproduction in any medium, provided the original work is properly cited.

Composite nanostructures of tungsten oxide and polyaniline (PANI) were fabricated on carbon electrode by electrocodeposition using sodium dodecylbenzene sulfonate (SDBS) as the template. The morphology of the composite can be controlled by changing SDBS surfactant and aniline monomer concentrations in solution. With increasing concentration of aniline in surfactant solution, the morphological change from nanoparticles to nanofibers was observed. The nanostructured WO₃/PANI composite exhibited enhanced capacitive charge storage with the specific capacitance of 201 F g⁻¹ at 1.28 mA cm⁻² in large potential window of -0.5 ~ 0.65 V versus SCE compared to the bulk composite film. The capacitance retained about 78% when the sweeping potential rate increased from 10 to 150 mV/s.

1. Introduction

Electrochemical capacitors (supercapacitors) have been considered as green energy storage devices which offer a number of desirable features such as fast charging/discharging within seconds and long cycle life. In supercapacitors, energy storage is mainly based on underpotential deposition (namely, double layer capacitors) or some redox process (namely, pseudocapacitors). The limitation of electrochemical capacitors to widespread application is their relative low energy density. Thus the challenge for the electrochemical capacitors is to promote the energy storage capability, meanwhile maintaining its high charging/discharging rate. Nanostructured electrode materials can meet these demands due to their high energy storage capacities and power output densities [1, 2].

Conducting polymers and metal oxides in nanosize scale are expected to display enhanced capacitive performance because of their large surface area, high conductivity, and light weight. The very high surface area and low charge transport resistance of nanomaterials favored faster transport of charges and ions between electrode materials and electrolyte in comparison to the bulk materials. Recently, much work

has focused on the development of nanomaterials for charge storage. Zhou and coworkers demonstrated that the capacitive performances of polyaniline (PANI) were enhanced with increasing its real surface area [3]. The nanofibrous PANI prepared by the pulse galvanostatic method displayed a high specific capacitance. Nanostructured NiO electrodeposited on stainless steel was reported to retain good supercapacitive performance at high scan rate [4].

Since the size and morphologies of nanoscale materials have significant influence on their properties, many efforts have been devoted to fabricate nanostructured materials [5, 6]. As we know, surfactant is widely used as additive to control the structure and morphologies of conducting polymers and inorganic species [7]. The surfactant self-assembled into organized templates in the bulk of solution or at interface offers potential to produce materials that retain its molecular imprint. It was reported that polymers with nanoparticle and nonfibrillar morphologies can be obtained by using anionic surfactant as the template, while those existing as nanofibers or nanorods structures can be afforded by cationic or nonionic surfactant-assisted chemical polymerizations [8]. Conducting polymer with nanosphere structures was

reported to be obtained through an electrochemical synthesis from a surfactant containing solution [9]. Surfactant has also been used in the preparation of inorganic species with high surface area [10, 11]. For instance, Baeck and coworkers described an electrochemical strategy for the formation of thin nanostructured WO_3 films from dilute surfactant solution [12]. Brezesinski utilized supermolecular assemblies of surfactant molecules as the structure-directing template to synthesize a nanocrystal-based porous TiO_2 film [13].

Compared to single component materials, conducting polymer based nanocomposites exhibit superior properties due to the synergistic effects. Recently, Hu and coworkers embedded SnO_2 nanoparticles in the PANI networks by *in situ* polymerization on surfaces of inorganic metal oxide nanoparticles; these nanocomposites showed high rate capability and cyclic stability for supercapacitor [14]. Murugan et al. demonstrated an *in situ* intercalation polymerization of 3,4-ethylenedioxythiophene to prepare a nanocomposite of poly(3,4-ethylenedioxythiophene) (PEDOT) and MoO_3 , in which the PEDOT was intercalated into layers of MoO_3 [15]. Composite films of WO_3 and PANI exhibited electrochromic properties with improved stability through immobilizing the oxide in the polymer matrix [16–18]. Our previous studies showed that the composites of PANI and WO_3 exhibited superior electrochemical sensing and pseudocapacitive properties compared to the respective single component [19, 20]. A model supercapacitor assembled by the obtained WO_3 /PANI composite as the negative electrode material displayed a significantly promoted energy density and improved cyclic stability. In this work, we present a simple and convenient method to fabricate PANI and tungsten oxide nanostructured composites on carbon electrode by electrocodeposition with sodium dodecylbenzene sulfonate (SDBS) surfactant as the template. Morphologies of the composites were investigated by scanning electron microscopy (SEM), while cyclic voltammetry and chronopotentiometry (CP) were carried out to study capacitive properties of the composites.

2. Experimental

2.1. Materials and Instrumentation. Aniline was purified by distillation before use. All other chemicals were of analytical grade and used as received. Electrochemical experiments were conducted with a multichannel potentiostat (VMP3, Bio-Logic-Science Instruments) in a three-electrode electrolytic cell. The reference and counter electrodes were saturated calomel electrode (SCE) and platinum plate (ca. 1 cm^2), respectively. Carbon cloth purchased from SGL (Germany) with geometric area of 0.78 cm^2 was used as the working electrode. All potentials are relative to the SCE.

2.2. Composite Films Preparation. Composite films of WO_3 /PANI were electrochemically deposited on carbon substrates by cyclic voltammetry. A potential range between -0.6 and 0.9 V at 50 mV/s was used. Prior to the deposition of the film, the carbon substrates were cleaned by water and acetone and then cleaned by potential dynamic scanned from -1.0 to 1.0 V for 2 cycles in $1\text{ M H}_2\text{SO}_4$. All the films

were grown by 25 cyclic voltammetric scans and then rinsed with distilled water.

The solution used for composite film deposition contained tungsten acid (0.15 M), H_2O_2 (0.04 M), and H_2SO_4 (0.5 M) with different amount of aniline and sodium dodecylbenzene sulfonate (SDBS). SDBS concentrations of 0, 1.3, 2.6, 5.2, 57.4, and 130 mM were used and the films produced were denoted as $\text{WP}^{\text{S}0}$, $\text{WP}^{\text{S}1.3}$, $\text{WP}^{\text{S}2.6}$, $\text{WP}^{\text{S}5.2}$, $\text{WP}^{\text{S}57.4}$, and $\text{WP}^{\text{S}130}$.

The composite films prepared from solutions containing 57.4 mM SDBS in the presence of 75 and 175 mM aniline were denoted as $\text{WP}^{\text{A}75/\text{S}57.4}$ and $\text{WP}^{\text{A}175/\text{S}57.4}$, while those from solutions containing 130 mM SDBS in the presence of 75 and 125 mM aniline were denoted as $\text{WP}^{\text{A}75/\text{S}130}$ and $\text{WP}^{\text{A}125/\text{S}130}$, respectively.

2.3. Composite Film Characterization. Pseudocapacitive behaviors of the films were studied by cyclic voltammetry and chronopotentiometry (CP) in $1\text{ M H}_2\text{SO}_4$ electrolyte. The morphologies of the samples were investigated by scanning electron microscopy (SEM, LEO SUPRA 35). The FT-IR spectra were recorded using Spectrum One FT-IR spectrometer (Perkin-Elmer, USA) with KBr pellets of powder samples scraped off from C substrate. The UV-vis spectra were recorded on composite films deposited on ITO using Lambda 35 UV/vis spectrophotometer.

3. Results and Discussions

3.1. Influence of SDBS Surfactant Concentration on Morphology of the Composite. Electrocodeposition of WO_3 and PANI was conducted through 25 cyclic voltammetric scans between -0.6 and 0.9 V at 50 mV/s in solutions containing various concentrations of SDBS surfactant. Surface morphologies of the composite films $\text{WP}^{\text{S}0}$, $\text{WP}^{\text{S}1.3}$, $\text{WP}^{\text{S}2.6}$, $\text{WP}^{\text{S}5.2}$, $\text{WP}^{\text{S}57.4}$, and $\text{WP}^{\text{S}130}$, obtained from 0, 1.3, 2.6, 5.2, 57.4, and 130 mM SDBS, were investigated by SEM (Figure 1). As can be seen in Figure 1, the particle size decreases with increasing concentration of SDBS in solution at lower concentration range ($< 5.2\text{ mM}$). The $\text{WP}^{\text{S}2.6}$ and $\text{WP}^{\text{S}5.2}$ composites show the smallest size of nanoparticles having average diameter of $10\sim 50\text{ nm}$. At the higher concentration of SDBS (e.g., 130 mM), particular large spherical particles assembled from 1D oriented nanoribbon-like structure were observed (Figure 1(f)), which indicate that the morphology of the composite is controllable by SDBS surfactant.

As we know, the SDBS surfactant consists of hydrophilic sulfonic acid and long hydrophobic alkyl chain. The spherical micelles are formed at the critical micelle concentration (cmc). The cmc for SDBS is about 1.5 mM in aqueous solution [21]. With the increase of SDBS concentration in solution, the spherical micelles self-assemble into larger spherical, cylindrical aggregates in solution, or flat bilayer micelles on the surface [22]. The aggregated micelles are negatively charged outside, so the anilinium cation can form complex structures by electrostatic interaction. The incorporation of aniline monomer with surfactant causes the aggregated micelle to swell and enlarge [7]. These complexes were assumed to serve

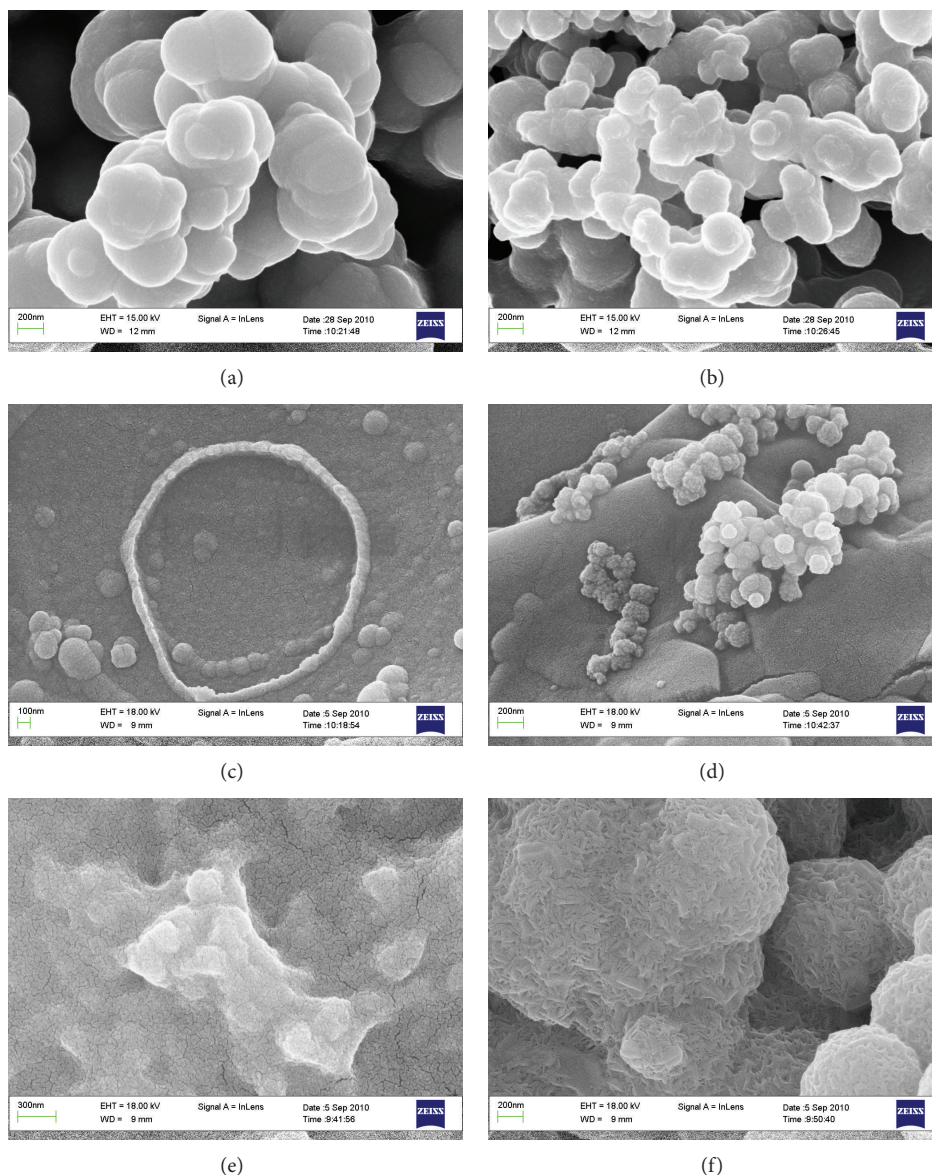


FIGURE 1: SEM images of WO_3/PANI films (a) $\text{WP}^{\text{S}0}$; (b) $\text{WP}^{\text{S}1.3}$; (c) $\text{WP}^{\text{S}2.6}$; (d) $\text{WP}^{\text{S}5.2}$; (e) $\text{WP}^{\text{S}57.4}$; and (f) $\text{WP}^{\text{S}130}$.

as structure template in the electrochemical polymerization process. At the lower SDBS concentrations (about 2~4 cmc), the smaller spherical micelle may facilitate the smaller particle size of the composite formed on the electrode (Figures 1(c) and 1(d)). With the increasing concentration of SDBS (e.g., 130 mM), the micelle becomes larger and more SDBS may aggregate more aniline monomers inside/outside the micelle, which more likely lead to the original 1D direction growth of the polymers as shown in Figure 1(f).

3.2. Influence of Aniline Concentration on Morphology of the Composite. It is interesting to note that aniline concentration also significantly influences morphology of the composite. Figure 2 presents the surface morphologies of $\text{WP}^{\text{A}75/\text{S}57.4}$ and $\text{WP}^{\text{A}175/\text{S}57.4}$ films afforded from 57.4 mM SDBS solutions

with 75 and 175 mM aniline and $\text{WP}^{\text{A}75/\text{S}130}$ and $\text{WP}^{\text{A}125/\text{S}130}$ films afforded from 130 mM SDBS solutions with 75 and 125 mM aniline, respectively. The composite particles tend to be of one-dimensional arrangement when aniline concentration increases in solution. Cationic anilinium is considered to be amphiphilic molecular because of its cationic head group and hydrophobic phenyl ring [23]. As the aniline concentration increases, more aniline monomer will be involved in micelle formation, and the competition between surfactant/monomer supermolecules and aniline monomer itself micelles may take place. Thus the increase of aniline concentration may exert influences on micelle compositions and structures. During the electrodeposition process, the preferentially 1D direction growth of polyaniline and the elongation of the rigid micelle result in the formation of 1D arrangement of the composite.

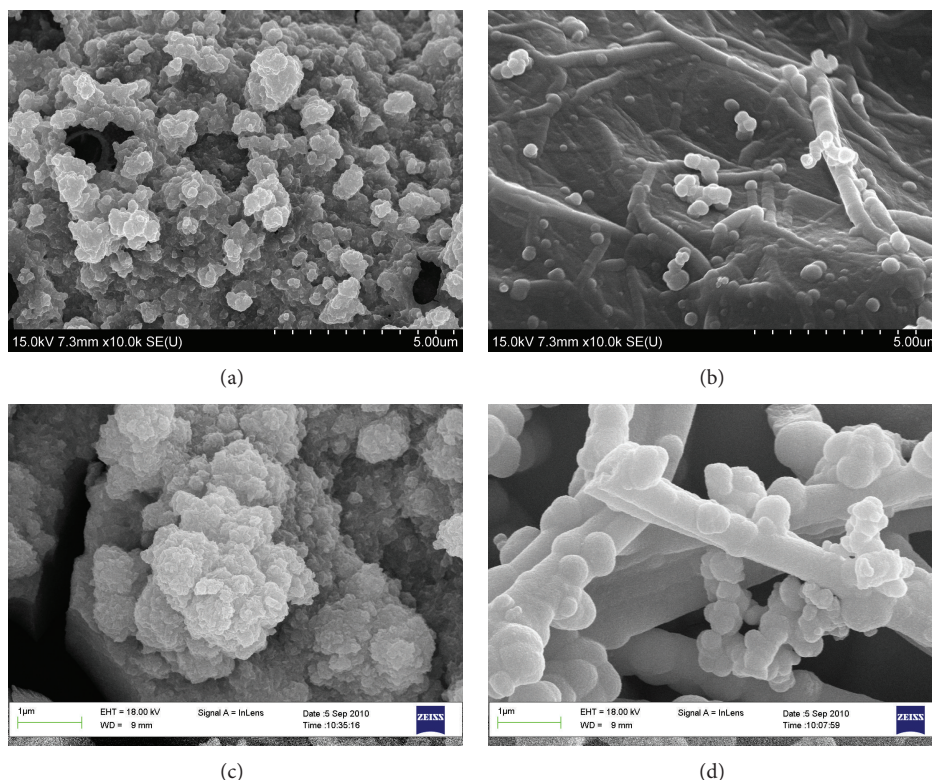


FIGURE 2: SEM images of WO_3/PANI films (a) $\text{WP}^{\text{A75}/\text{S57.4}}$; (b) $\text{WP}^{\text{A175}/\text{S57.4}}$; (c) $\text{WP}^{\text{A75}/\text{S130}}$; and (d) $\text{WP}^{\text{A125}/\text{S130}}$.

Similar trends were observed on similarly prepared PANI. Figure 3 shows the SEM images of PANI films of PANI^{A75} , $\text{PANI}^{\text{A125}}$, and $\text{PANI}^{\text{A175}}$ electrodeposited from solutions containing 75, 125, and 175 mM aniline, respectively. PANI is prone to grow in 1D directions as the concentration of aniline increased in solution. The short PANI nanorods with average diameter of 150~200 nm gradually changed to long interconnected PANI nanofibers with diameter of 80~100 nm.

3.3. Influence of SDBS Concentration on Pseudocapacitive Properties of the Composite. To investigate the pseudocapacitive properties of the composite films, cyclic voltammetric scans were conducted on WP^{S0} , $\text{WP}^{\text{S1.3}}$, $\text{WP}^{\text{S2.6}}$, $\text{WP}^{\text{S5.2}}$, $\text{WP}^{\text{S57.4}}$, and WP^{S130} in 1 M H_2SO_4 (Figure 4(a)). The WO_3 -related (A/A') and PANI-related (B/B' and C/C') redox pairs can be seen in Figure 4(a), similar to our previously reported WO_3/PANI composite [19]. The redox pair B/B' which corresponds to the exchange between fully reduced (leucoemeraldine) and half-oxidized (emeraldine) PANI is a good indicator for the electrochemical activity of PANI. The currents of B/B' are higher for the composites made in the presence of SDBS than that from free of SDBS. When SDBS was added in the solution up to 2.6 mM, the WO_3 -related (A/A') peak currents on the cyclic voltammograms (CVs) of the composites were increased. However, the currents decreased with the further increase of SDBS concentration, indicating the restriction of the tungsten oxide deposition probably

because of the strong electrostatic repulsive force between the negative headgroup of the surfactant micelles and tungstate anions (suggested by the micrograph of Figure 1(f)). The composite $\text{WP}^{\text{S2.6}}$ exhibited higher electroactivities of both WO_3 and PANI in Figure 4(a). This should be related to the nanostructure of the $\text{WP}^{\text{S2.6}}$ film which may provide more opportunity for the reactive centers on the film to contact with electrolyte and so facilitate the charge transfer in the bulk of the film.

The galvanostatic charge-discharge measurements were carried out by CP on these composite films (Figure 4(b)). The WO_3/PANI composite films display pseudocapacitive behaviors in a comparatively larger potential range from -0.5 V to 0.65 V versus SCE due to the combination of electrochemical activities of WO_3 and PANI. The large potential range is favored for the increase of energy density for supercapacitors. The specific capacitances of the composite films increase with the increase of SDBS concentration up to 2.6 mM (inset of Figure 4(b)). The CP results show that $\text{WP}^{\text{S2.6}}$ composite film exhibits the highest specific capacitance of 201 F/g. The inefficient contribution of WO_3 to the total capacitance of the composite can be observed in the negative potential range of the CP curves of $\text{WP}^{\text{S57.4}}$ and WP^{S130} , which is in agreement with cyclic voltammetry results.

3.4. Characterization of the WP Nanocomposite. EDX and FT-IR spectra were recorded to characterize the typical nanocomposite of $\text{WP}^{\text{S2.6}}$. The EDX spectrum displays the

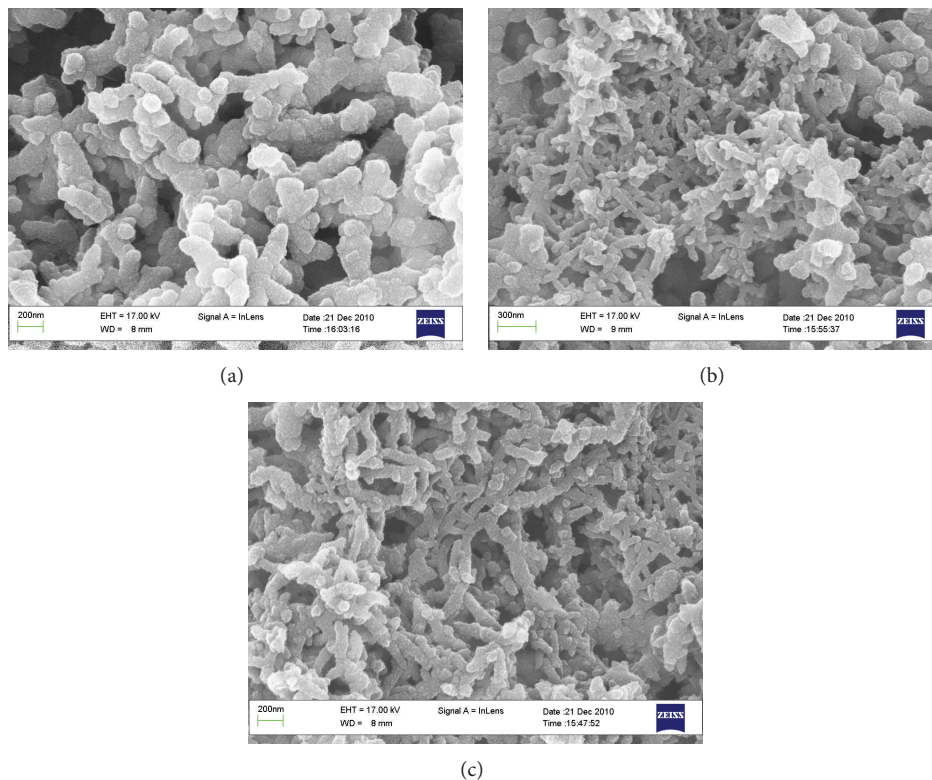


FIGURE 3: SEM images of (a) PANI^{A75}; (b) PANI^{A125}; and (c) PANI^{A175}.

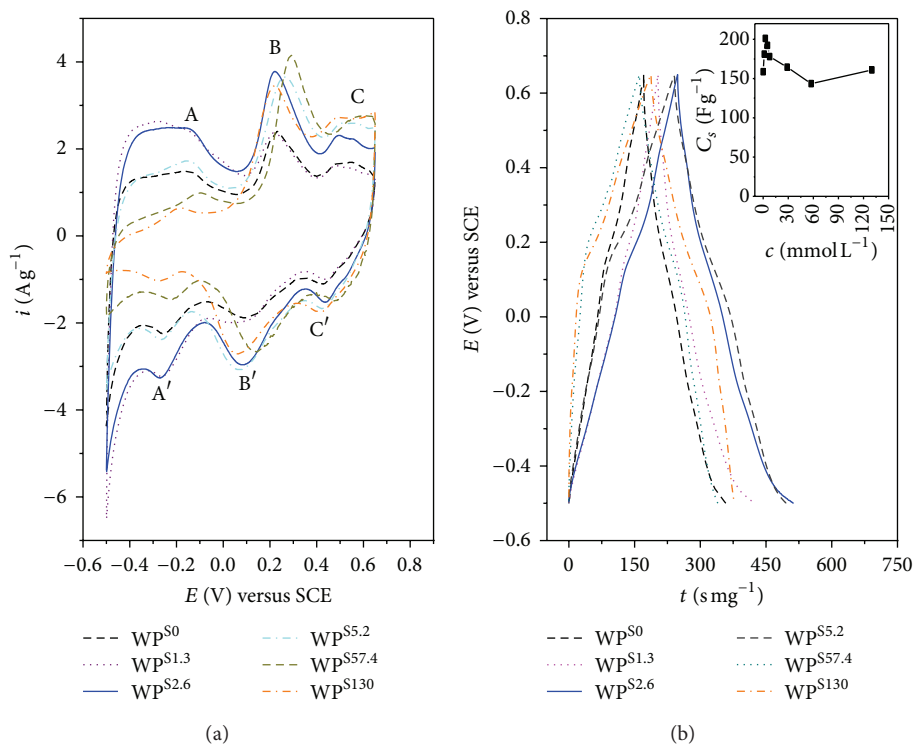


FIGURE 4: (a) CVs of WO₃/PANI films of WP^{S0}, WP^{S1.3}, WP^{S2.6}, WP^{S5.2}, WP^{S57.4}, and WP^{S130} in 1 M H₂SO₄. Scan rate: 10 mV/s. (b) Constant current charge-discharge curves of WO₃/PANI films in 1 M H₂SO₄ at 1.28 mA/cm². Inset shows the specific capacitance of WO₃/PANI electrodes obtained from solutions containing SDBS in various concentrations.

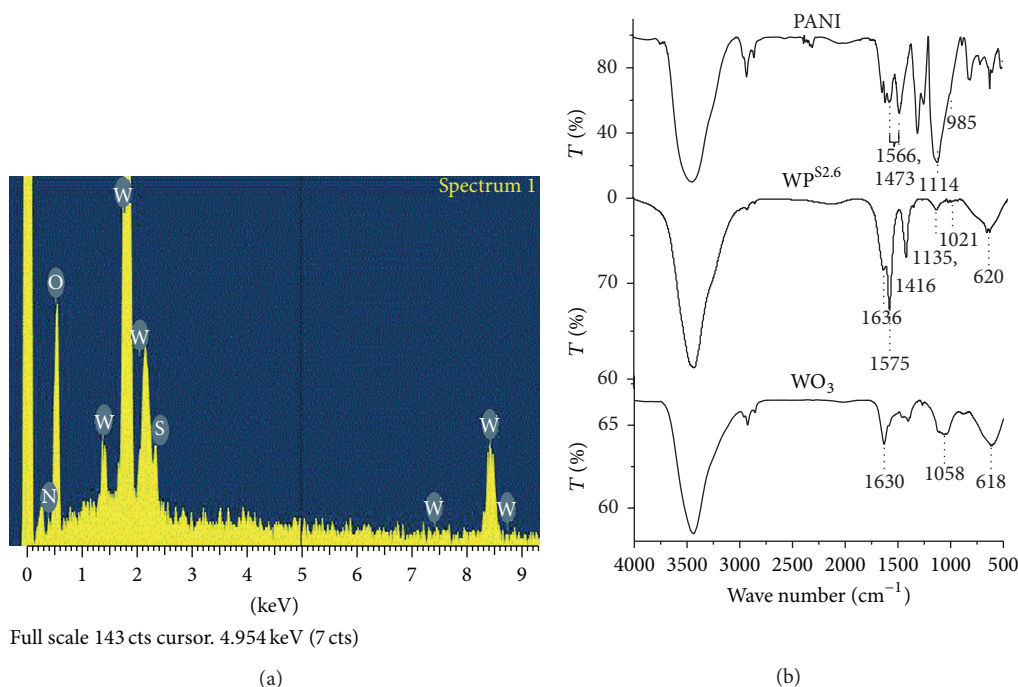


FIGURE 5: (a) EDX spectrum of WP^{S2.6}, (b) FT-IR spectra of PANI, WP^{S2.6}, and WO₃.

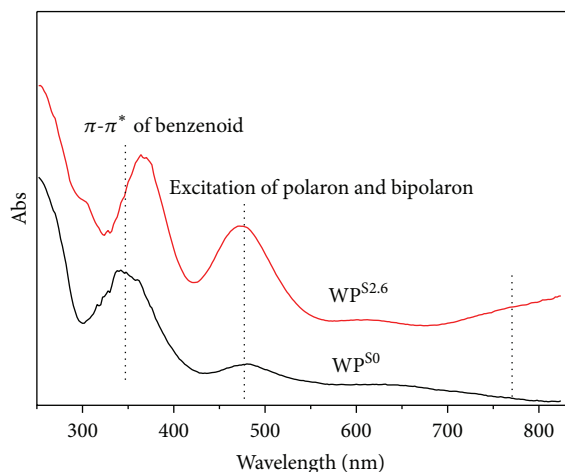
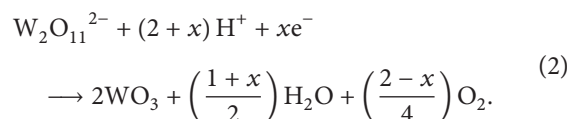
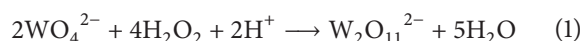


FIGURE 6: UV-vis spectra of the WP^{S2.6} and WP^{S0}.

signals of W from WO₃ and N from PANI in Figure 5(a). From FT-IR spectra in Figure 5(b), WP^{S2.6} exhibits characteristic vibrations of both PANI and WO₃. The peaks at 1575 and 1416 cm⁻¹ are due to the stretching vibration of quinoid (N=Q=N) and benzenoid (N-B-N) rings, respectively [23], which appear at 1566 and 1473 cm⁻¹ in the spectrum of PANI. Bands at 1135 cm⁻¹ in the spectrum of WP^{S2.6} and 1114 cm⁻¹ in that of PANI are attributed to the characteristic band of protonated PANI [24]. As can be observed in Figure 5(b), the intensity of the peak at 1114 cm⁻¹ in the spectrum of PANI is rather higher than that of the WP^{S2.6}. This is mainly attributed to the consumption of H⁺ near or on the electrode surface by

WO₃ deposition process, which results in the decrease of the protonated degree of PANI in the composite. The deposition process of WO₃ can be represented by the following equation [25]:



The absorption peak at 1636 cm⁻¹ for WP^{S2.6}, corresponding to the peak at 1630 cm⁻¹ for WO₃, is attributed to the in-plane bending mode δ(H₂O) of structure water [26]. The O-W-O stretching mode appears as a broad band around 620 cm⁻¹ which is similar to that of WO₃ at 618 cm⁻¹ [27]. The broad peak at 1058 cm⁻¹ in the WO₃ spectrum was overlapped with the characteristic protonated PANI peak at 1135 cm⁻¹ in the spectrum of WP^{S2.6}.

The UV-vis spectra of the WP^{S2.6} (deposited on ITO) were shown in Figure 6, together with the spectra of WP^{S0}. The band at 320–360 nm corresponds to π-π* electron transition of benzenoid segments, which can be assigned to the intermediate state of PANI between leucoemeraldine and emeraldine [8]. The bands at ca. 470 and ca. 800 nm are concerned with the doping level and formation of polarons and bipolarons (quinoid segments), respectively. From Figure 6, the band at 320–360 nm in the spectra of WP^{S2.6} moved to the long wavelength (red shift) in comparison with WP^{S0}, likely because of the increasing delocalized degree of π-π* conjugate system in WP^{S2.6}. Furthermore, the WP^{S2.6} demonstrated the increased intensity of the band at ca. 470 nm and the absorption band

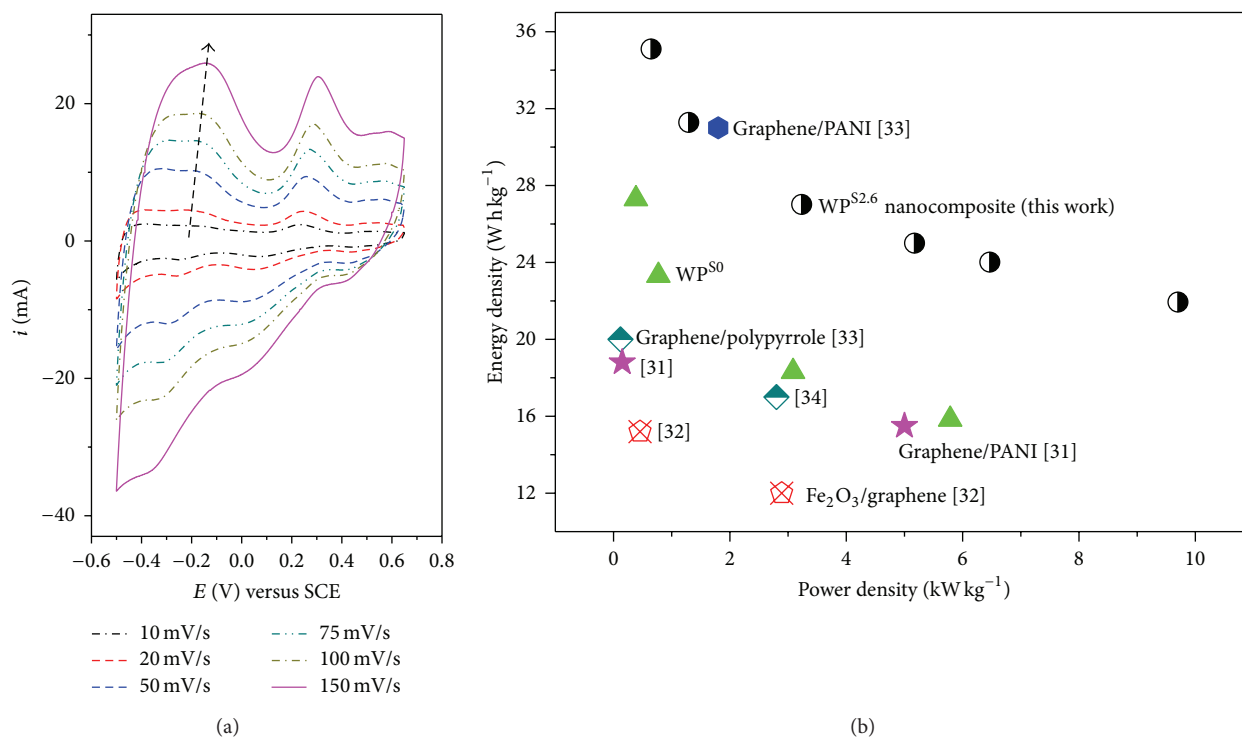


FIGURE 7: (a) CVs of WP^{S2.6} in 1 M H₂SO₄ at different scan rates from 10 to 150 mV/s as indicated by the arrow in the figure. (b) Ragone plots of nano-WP^{S2.6}, bulk WP^{S0} films, and the value of recently reported composite films for comparison.

at around 800 nm with a long tail, which correspond to the polaron bands related transitions, implying the emeraldine salt form of PANI in WP^{S2.6} [5, 28].

3.5. Pseudocapacitive Properties of the WP Nanocomposite.

Figure 7(a) presents the cyclic voltammograms of the WP^{S2.6} composite film at scan rates of 10–150 mV/s with potential range from -0.5 V to 0.65 V. The mirror-like images of CV curves reveal the typical pseudocapacitive behavior with rapid current response on voltage reversal. The CV curves still remain nearly mirror-like image without obvious distortion even at scan rate of 150 mV/s. This excellent rate capability should be mainly attributed to the large accessible surface areas and low charge transport resistance provided by the nanostructures of the composite which facilitate electrolyte ion and charge transport during charge-discharge process. The area capacitance is calculated to be 0.284 F/cm² at the scan rate of 10 mV/s and 0.222 F/cm² at 150 mV/s. The capacitance retained about 78% when the scan rate increased from 10 to 150 mV/s, which is comparable to those of previously reported nano-MnO₂ (retained about 46% from 10 to 150 mV/s) [29], ordered mesoporous WO_{3-x} (about 45% from 10 to 50 mV/s) [30], and polyaniline stabilized WO₃ nanocomposite (about 36% from 5 to 100 mV/s) [18].

Constant current charge-discharge experiments were conducted on WP^{S2.6} and WP^{S0} by chronopotentiometry at various current densities. Ragone plots were obtained based on these experiments (Figure 7(b)). The WP^{S2.6} film has much higher energy density than WP^{S0} film at the

same power density. The energy density of the WP^{S2.6} electrode is found to be 37 Wh kg⁻¹ at the power density of 650 W kg⁻¹ and 25 Wh kg⁻¹ at 5 kW kg⁻¹, which is 46% higher than that of WP^{S0} film at 650 W kg⁻¹ and 56% higher at 5 kW kg⁻¹. Moreover, the nanocomposite WP^{S2.6} film also shows higher energy density and power density than other recently reported values of composite films (Figure 7(b)) [31–34].

4. Conclusions

The electrocodeposition of tungsten oxide and polyaniline composite nanostructures using SDBS surfactant as the template showed that both the SDBS and aniline monomer in the deposition solution could act as the structure direction reagent in the formation of the nanostructured composite film. The morphology of the composite is controllable by SDBS and aniline monomers in solution. The resulting composite film with spherical nanoparticles was formed from 2.6–5.2 mM SDBS (about 2–4 times of cmc). With the concentration of aniline monomer increased in the solution, one-dimensional growth trends were observed for both of PANI and the composites. Nanostructured composite of WP^{S2.6} obtained from the solution containing 2.6 mM SDBS displayed the best capacitive performance and rate capability. The specific capacitance can be retained about 78% with the increasing of sweeping potential rate for cyclic voltammetric scans from 10 to 150 mV/s, which make it useful for negative electrode for supercapacitors.

Conflict of Interests

The authors declare that there is no conflict of interests regarding the publication of this paper.

Acknowledgment

This work was supported by Liaoning Province new Ph.D. startup fund (Project no. 20131039).

References

- [1] S. R. Sivakkumar, W. J. Kim, J.-A. Choi, D. R. MacFarlane, M. Forsyth, and D.-W. Kim, "Electrochemical performance of polyaniline nanofibres and polyaniline/multi-walled carbon nanotube composite as an electrode material for aqueous redox supercapacitors," *Journal of Power Sources*, vol. 171, no. 2, pp. 1062–1068, 2007.
- [2] C. Meng, C. Liu, and S. Fan, "Flexible carbon nanotube/polyaniline paper-like films and their enhanced electrochemical properties," *Electrochemistry Communications*, vol. 11, no. 1, pp. 186–189, 2009.
- [3] H. Zhou, H. Chen, S. Luo, G. Lu, W. Wei, and Y. Kuang, "The effect of the polyaniline morphology on the performance of polyaniline supercapacitors," *Journal of Solid State Electrochemistry*, vol. 9, no. 8, pp. 574–580, 2005.
- [4] K. R. Prasad and N. Miura, "Electrochemically deposited nanowhiskers of nickel oxide as a high-power pseudocapacitive electrode," *Applied Physics Letters*, vol. 85, no. 18, pp. 4199–4201, 2004.
- [5] H. Ding, M. Wan, and Y. Wei, "Controlling the diameter of polyaniline nanofibers by adjusting the oxidant redox potential," *Advanced Materials*, vol. 19, no. 3, pp. 465–469, 2007.
- [6] M. J. Giz, S. L. de Albuquerque Maranhão, and R. M. Torresi, "AFM morphological study of electropolymerised polyaniline films modified by surfactant and large anions," *Electrochemistry Communications*, vol. 2, no. 6, pp. 377–381, 2000.
- [7] A. D. W. Carswell, E. A. O'Rear, and B. P. Grady, "Adsorbed surfactants as templates for the synthesis of morphologically controlled polyaniline and polypyrrole nanostructures on flat surfaces: from spheres to wires to flat films," *Journal of the American Chemical Society*, vol. 125, no. 48, pp. 14793–14800, 2003.
- [8] V. Eskizeybek, F. Sari, H. Gülce, A. Gülce, and A. Avci, "Preparation of the new polyaniline/ZnO nanocomposite and its photocatalytic activity for degradation of methylene blue and malachite green dyes under UV and natural sun lights irradiations," *Applied Catalysis B: Environmental*, vol. 119–120, pp. 197–206, 2012.
- [9] J. A. Raj, J. Mathiyarasu, C. Vedhi, and P. Manisankar, "Electrochemical synthesis of nanosize polyaniline from aqueous surfactant solutions," *Materials Letters*, vol. 64, no. 8, pp. 895–897, 2010.
- [10] M. Deepa, A. K. Srivastava, K. N. Sood, and S. A. Agnihotry, "Nanostructured mesoporous tungsten oxide films with fast kinetics for electrochromic smart windows," *Nanotechnology*, vol. 17, no. 10, pp. 2625–2630, 2006.
- [11] M. Deepa, A. K. Srivastava, and S. A. Agnihotry, "Influence of annealing on electrochromic performance of template assisted, electrochemically grown, nanostructured assembly of tungsten oxide," *Acta Materialia*, vol. 54, no. 17, pp. 4583–4595, 2006.
- [12] S.-H. Baeck, K.-S. Choi, T. F. Jaramillo, G. D. Stucky, and E. W. McFarland, "Enhancement of photocatalytic and electrochromic properties of electrochemically fabricated mesoporous WO₃ thin films," *Advanced Materials*, vol. 15, no. 15, pp. 1269–1273, 2003.
- [13] T. Brezesinski, J. Wang, J. Polleux, B. Dunn, and S. H. Tolbert, "Templated nanocrystal-based porous TiO₂ films for next-generation electrochemical capacitors," *Journal of the American Chemical Society*, vol. 131, no. 5, pp. 1802–1809, 2009.
- [14] Z.-A. Hu, Y.-L. Xie, Y.-X. Wang, L.-P. Mo, Y.-Y. Yang, and Z.-Y. Zhang, "Polyaniline/SnO₂ nanocomposite for supercapacitor applications," *Materials Chemistry and Physics*, vol. 114, no. 2–3, pp. 990–995, 2009.
- [15] A. V. Murugan, A. K. Viswanath, C. S. Gopinath, and K. Vijayamohan, "Highly efficient organic-inorganic poly(3,4-ethylenedioxythiophene)-molybdenum trioxide nanocomposite electrodes for electrochemical supercapacitor," *Journal of Applied Physics*, vol. 100, no. 7, Article ID 074319, 2006.
- [16] P. K. Shen, H. T. Huang, and A. C. C. Tseung, "Study of tungsten trioxide and polyaniline composite films. I. Electrochemical and electrochromic behavior," *Journal of the Electrochemical Society*, vol. 139, no. 7, pp. 1840–1845, 1992.
- [17] N. Parvatikar, S. Jain, S. Khasim, M. Revansiddappa, S. V. Bhoraskar, and M. V. N. A. Prasad, "Electrical and humidity sensing properties of polyaniline/WO₃ composites," *Sensors and Actuators B: Chemical*, vol. 114, no. 2, pp. 599–603, 2006.
- [18] H. Wei, X. Yan, S. Wu, Z. Luo, S. Wei, and Z. Guo, "Electropolymerized polyaniline stabilized tungsten oxide nanocomposite films: electrochromic behavior and electrochemical energy storage," *The Journal of Physical Chemistry C*, vol. 116, no. 47, pp. 25052–25064, 2012.
- [19] B.-X. Zou, Y. Liang, X.-X. Liu, D. Diamond, and K.-T. Lau, "Electrodeposition and pseudocapacitive properties of tungsten oxide/polyaniline composite," *Journal of Power Sources*, vol. 196, no. 10, pp. 4842–4848, 2011.
- [20] B.-X. Zou, X.-X. Liu, D. Diamond, and K.-T. Lau, "Electrochemical synthesis of WO₃/PANI composite for electrocatalytic reduction of iodate," *Electrochimica Acta*, vol. 55, no. 12, pp. 3915–3920, 2010.
- [21] K. Naoi, Y. Oura, M. Maeda, and S. Nakamura, "Electrochemistry of surfactant-doped polypyrrole film(I): formation of columnar structure by electropolymerization," *Journal of the Electrochemical Society*, vol. 142, no. 2, pp. 417–422, 1995.
- [22] C.-H. Yang, Y.-K. Chih, H.-E. Cheng, and C.-H. Chen, "Nanofibers of self-doped polyaniline," *Polymer*, vol. 46, no. 24, pp. 10688–10698, 2005.
- [23] S. Bhadra, S. Chattopadhyay, N. K. Singha, and D. Khastgir, "Improvement of conductivity of electrochemically synthesized polyaniline," *Journal of Applied Polymer Science*, vol. 108, no. 1, pp. 57–64, 2008.
- [24] L. Duić, Z. Mandić, and S. Kovač, "Polymer-dimer distribution in the electrochemical synthesis of polyaniline," *Electrochimica Acta*, vol. 40, no. 11, pp. 1681–1688, 1995.
- [25] E. A. Meulenkamp, "Mechanism of WO₃ electrodeposition from peroxy-tungstate solution," *Journal of the Electrochemical Society*, vol. 144, no. 5, pp. 1664–1671, 1997.
- [26] L. Barrio, J. M. Campos-Martín, and J. L. G. Fierro, "Spectroscopic and DFT study of tungstic acid peroxocomplexes," *Journal of Physical Chemistry A*, vol. 111, no. 11, pp. 2166–2171, 2007.

- [27] M. Deepa, A. K. Srivastava, K. N. Sood, and A. V. Murugan, "Nanostructured tungsten oxide-poly(3,4-ethylenedioxythiophene): poly(styrenesulfonate) hybrid films: synthesis, electrochromic response, and durability characteristics," *Journal of the Electrochemical Society*, vol. 155, no. 11, pp. D703–D710, 2008.
- [28] H.-F. Jiang and X.-X. Liu, "One-dimensional growth and electrochemical properties of polyaniline deposited by a pulse potentiostatic method," *Electrochimica Acta*, vol. 55, no. 24, pp. 7175–7181, 2010.
- [29] K. R. Prasad and N. Miura, "Potentiodynamically deposited nanostructured manganese dioxide as electrode material for electrochemical redox supercapacitors," *Journal of Power Sources*, vol. 135, no. 1-2, pp. 354–360, 2004.
- [30] C. Jo, I. Hwang, J. Lee, C. W. Lee, and S. Yoon, "Investigation of pseudocapacitive charge-storage behavior in highly conductive ordered mesoporous tungsten oxide electrodes," *The Journal of Physical Chemistry C*, vol. 115, no. 23, pp. 11880–11886, 2011.
- [31] Q. Wu, Y. Xu, Z. Yao, A. Liu, and G. Shi, "Supercapacitors based on flexible graphene/polyaniline nanofiber composite films," *ACS Nano*, vol. 4, no. 4, pp. 1963–1970, 2010.
- [32] D. Wang, Y. Li, Q. Wang, and T. Wang, "Nanostructured Fe_2O_3 -graphene composite as a novel electrode material for supercapacitors," *Journal of Solid State Electrochemistry*, vol. 16, no. 6, pp. 2095–2102, 2012.
- [33] H. Wang, Q. Hao, X. Yang, L. Lu, and X. Wang, "A nanostructured graphene/polyaniline hybrid material for supercapacitors," *Nanoscale*, vol. 2, no. 10, pp. 2164–2170, 2010.
- [34] D. Zhang, X. Zhang, Y. Chen, P. Yu, C. Wang, and Y. Ma, "Enhanced capacitance and rate capability of graphene/polypyrrole composite as electrode material for supercapacitors," *Journal of Power Sources*, vol. 196, no. 14, pp. 5990–5996, 2011.